2019

Investigation on liquid-liquid dispersion in stirred tanks through experimental approach and computational fluid dynamic (CFD)

Khajeh Naeeni, Sepehr

http://knowledgecommons.lakeheadu.ca/handle/2453/4379

Investigation on Liquid-Liquid Dispersion in Stirred Tanks through Experimental Approach and Computational Fluid Dynamic (CFD)

By

Sepehr Khajeh Naeeni

B.Sc. Chemical Engineering
Sharif University, Tehran, Iran, 2016

A thesis submitted to the Faculty of Graduate Studies in partial
fulfillment of the requirements for the degree of Master of Applied Science
in

Environmental Engineering

Winter 2019
Lakehead University

Thunder Bay, Ontario, Canada

Abstract

Investigation on Liquid-Liquid Dispersion in Stirred Tanks through Experimental Approach and Computational Fluid Dynamic (CFD)

Sepehr Khajeh Naeeni

MASc, Environmental Engineering, Lakehead University, Thunder Bay, 2019

Stirred tanks have a vital role in chemical engineering industries. Among the various applications of stirred tanks, mixing of two immiscible liquid phases is of interest in chemical processes. Mixing of two immiscible liquids in the stirred tank is an integral part of achieving a stable emulsion, which impacts the product quality. The design of the stirred tanks including but not limited to the geometry and dimensions of the vessel, the location, size, and the type of the impeller, fluid rheology, and the volume fraction of dispersed phase relies on comprehensive knowledge about the liquid-liquid mixing performance. One of the major factors affecting the stability of liquid-liquid dispersion is droplet size distribution (DSD) of dispersed phase. The study of DSD in liquid-liquid dispersions still relies on experimental data.

The main objective of this study is to evaluate the effect of dispersed phase viscosity, volume fraction, and agitation speed on dilute liquid-liquid dispersions. Therefore, the liquid-liquid dispersion in stirred tank has been evaluated through electrical resistance tomography (ERT), focused beam reflectance measurement (FBRM), and computational fluid dynamics (CFD). ERT provides a non-intrusive online measurement to evaluate the mixing hydrodynamic of dispersion in the tank. FBRM technique is an online particle size measurement technique which evaluates the effect of mixing process on particle interactions and droplet size distribution. Using CFD coupled with population balance modeling (PBM) is the last step toward complete analysis of liquid-liquid dispersion process. The CFD model was simulated the multiphase flow based on the Eulerian-Eulerian approach and validated by experimental measurements. The standard k-ε model was employed to predict the turbulent flow and circulation of the liquid phase. The population balance modeling (PBM) was used to track the droplet size and to predict the effect of mixing process on droplet size distribution. An increase in agitation speed was found to decrease the mean and Sauter mean diameter while increasing the homogeneity of the system. The correlations between Sauter mean diameter and hydrodynamic parameters of the system were also investigated. Wider distribution was observed at higher volume fractions without a significant change in droplet size. However, increasing the volume fraction has a damping effect on the homogeneity of the system. Increasing the viscosity of the oil phase resulted in a poor mixing with a gradual shift towards smaller droplets.

The chord length distributions (CLD) obtained by FBRM were used to evaluate the effect of mixing process on droplet's shape deformation in terms of the circularity of drops. A further shape analysis was performed using Python coding. Results show a change in the shape of droplets from sphere to spheroid with an increase in agitation speed. An increase in droplet deformation rate was also observed with an increase in the oil phase viscosity and a decrease in the interfacial tension between two liquids.

Acknowledgement

The research work of this thesis was carried out at Lakehead University, in the program of Environmental Engineering.

I wish to thank my supervisor Dr. Leila Pakzad for her continuous support, leadership, and encouragement in this research. I express my appreciation to Dr. Pedram Fatehi for providing test facilities for this study. I would also like to thank my thesis committee members, Dr. Ehsan Azar from Department of Civil Engineering and Dr. Baoqiang Liao from Department of Chemical Engineering for their time and consideration.

Furthermore, I wish to thank my colleague at Lakehead University, Minoo Ataie, for her kindness and valuable knowledge on FBRM instrument. I acknowledge the assistance of student colleagues (Siamak Aghazamin, Kayte Sutherland, and Fahimeh Mirshekari) in the multi-phase research group for their cherished friendship and pleasant working atmosphere throughout the past two years.

I acknowledge Natural Sciences and Engineering Research Council of Canada (NSERC) for the financial support during this work. I also acknowledge the HPCVL for providing the high-performance computing facilities.

To my Parents, **Nadia** and **Saeed**,

I thank the stars every night that I am lucky enough to live in a world where someone like you exist and give love. Without all your support, I would not be where I am today.

Dedicated to the memory of my grandfather Seyed Reza Saadati.

Table of Contents

List of Tables

Chapter 2: Literature Review

Chapter 3: Experimental Design and Procedure

Chapter 4: CFD Model Development

Chapter 5: First Study

Chapter 6: Second Study

List of Figures

Chapter 2: Literature review

Chapter 3: Experimental Design and Procedure

Chapter 4: CFD Model Development

Chapter 5: First Study

Chapter 6: Second Study

Introduction

Stirred vessel are broadly adopted in various industrial plants to carry out multiphase mixing such as gas-liquid, gas-liquid-solid, solid-liquid, and liquid-liquid (Paul et al., 2004). Elaborately, mixing is a process of distributing elements homogenously throughout the media (Tatterson, 1991). Mixing process has an extensive application in various contexts of chemicals, pharmaceuticals, petrochemicals, biotechnology, polymer industry, paints, cosmetics, waste water treatment, and mineral processing (Paul et al., 2004). Liquid-liquid mixing process in stirred tanks is a challenging procedure due to inherent complex rheology of dispersion, which leads to inhomogeneous flows (Patel et al., 2015).

An immiscible liquid-liquid dispersion type can be oil-in-water (O/W) in which oil droplets are dispersed in an aqueous phase, for instance, mayonnaise, and milk. In the other type, water droplets are dispersed in an oil phase which is called water-in-oil (W/O) such as margarine, and butter. The formation of droplets and their significant participation in making a homogenous and stable dispersion is of great interest. The droplet size distribution in dispersion is also a key element in design and scale-up. It widely has been accepted that stability of a mixture of two immiscible liquids and the relative interactions strongly depends on both hydrodynamics and droplet size distribution of the fluid in the geometry.

In most cases the flow around the rotating impeller blades lead to high levels of turbulence and high shear rates. The flow is anisotropic and inhomogeneous over the entire volume. A better understanding of the mixing process is needed in order to design stirred tanks that can meet the required operation conditions. The general understanding of mixing process in stirred tank was achieved over the years through experimental investigations for various tank geometries and materials. Experimental studies are usually costly and time consuming. An alternative approach to overcome this drawback is using advanced computational fluid dynamic (CFD). CFD is a useful approach to simulate a process with various parameters contributing in the process, in shorter time. Proper validation of the simulation results relies upon experimental studies such as tomographic techniques, and particle size measurement instruments such as focused beam reflectance measurement (FBRM). Even though significant advances have been achieved in liquid-liquid mixing in past years, estimation of the droplet size distribution (DSD) for dilute liquid-liquid dispersion agitated in stirred tank has not been investigated in both experimental and modeling aspects.

This thesis describes the hydrodynamic characteristics and chord length distribution of diluted liquid-liquid dispersions. This purpose was achieved by:

- Evaluation of mixing performance in terms of flow pattern and mixing index using electrical resistance tomography (ERT).
- Chord length distribution of dispersion using focused beam reflectance measurement (FBRM) as well as an investigation on the shape of drops.
- Comprehensive analysis of the dispersion using CFD model development.
- A novel particle shape analysis by using Python coding language.

Chapter two provides a literature review on liquid-liquid dispersion and its application in industry. The studies related to the application of ERT, FBRM, and CFD in liquid-liquid dispersion are presented in this chapter. At the end, the fundamentals in particle shape analysis using FBRM instrument are described.

Chapter three is concerned with the design, specification, and operation of ERT and FBRM instruments. The experimental procedure and conditions are also provided in this chapter.

Chapter four is about the CFD model development. This chapter reviews the general information about CFD such as governing equations, numerical methods, and methods of discretizing the equations as well as population balance modeling.

Chapter five presents the first part of my study (known as "**First Study**" henceforth) on mixing of water-in-oil dispersion. CFD results were validated by available experimental data (Boxall et al., 2010). The objective of this research is to study the effect of impeller speed, viscosity of the primary phase, volume fraction of the dispersed phase on DSD of water-in-oil emulsion.

Chapter six provides the results for the second part of my study (known as "**Second Study**" henceforth) on oil-in-water dispersion by means of experimental study as well as CFD simulations. A discussion on shape factor and correlations between Sauter mean diameter and hydrodynamic of the system through the experimental results obtained by ERT and FBRM following by CFD results are presented in this chapter.

Chapter seven is devoted to the overall conclusions and recommendations for future works.

Finally, Python codes for modeling the droplet shape is presented in the **Appendix A**.

Literature Review

2.1 Introduction

Liquid-liquid mixing is a key stage for various applications in chemical, pharmaceutical, petroleum, and food manufacturing processes. Examples of industrial processes involving liquid-liquid mixing include polymerization, emulsification, and solvent extraction. In all these processes, drop size distribution is among the most important parameters for evaluating dispersion stability and efficiency of operation. It plays an important role in affecting the mass transfer rate between the phases in liquid-liquid systems (Boxall et al., 2010). Smaller drop sizes are more advantageous in mass transfer processes as they produce larger interfacial and mass transfer areas around the impeller zone compared to drops with larger size (El-Hamouz et al., 2009). Due to the significant application of liquid-liquid dispersions in various industries, understanding the fundamentals of mixing which is crucial to industries scale-up demands more investigation. The efficiency of mixing performance leads to the better product quality.

The size of droplets in dispersion is an important factor, as it has an effect on the stability and rheology of emulsions. Typically, the complete homogeneity in the mixing of two immiscible liquids is desired. An important parameter for the evaluation of mixing effectiveness is mixing index (Harrison et al., 2012). Mixing index is defined as the average standard deviation of dispersed phase volume fraction in each volume element of dispersion. This parameter is related to impeller type, agitation speed, volume fraction and fluid rheology (Harrison et al., 2012). Although mixing of single phase flow is well understood within past decades, understanding the mixing of two immiscible liquid-liquid dispersion still demands more investigation.

The goal of this chapter is to provide a brief review of literature on the important parameters related to the liquid-liquid dispersion systems such as droplet size distribution and mixing index. Finally, the research objectives are presented.

2.2 Droplet Size Distribution

Droplet size distribution (DSD) has a significant effect on the mass and heat transfer rates through interfacial areas (Sjoblom, 2001). Besides, it plays a crucial role in design and scale-up of mixers and chemical reactors. However, sustaining stable dispersion with the desired DSD in large-scale industrial tanks is a demanding task with high economic risk involved.

Several studies have been conducted on DSD in emulsions experimentally (Ohtake et al., 1987 and 1988; Lovick et al., 2005; Singh et al., 2009; Boxall et al., 2010; Khalil et al., 2010). One of the most common and simple techniques for the droplet size measurement is the sample withdrawal technique. The size of withdrawn droplets was then measured by a microscope (Godfrey and Grilc, 1977; Kumar et al., 1991) or a photometer (Verhoff et al., 1977). The drawbacks of this technique include biased sampling of certain droplet sizes and its' limitation to the dilute dispersion system, (Godfery and Grilc, 1977).

Solsvik and Jakobsen (2015) used a high-speed imaging technique to assess the breakage mechanism in a liquid-liquid dispersion system. The disadvantage of this technique is that the sample image may not be a good representative for all available droplet sizes in the dispersion system. The recent development of lasers, i.e. laser diffraction or laser backscattering method, introduce new particle size measurement which overcome the above-mentioned limitations (Lovick et al., 2005). Lovick et al. (2005) used an optical reflectance measurement (ORM) particle size analyser and an endoscope to obtain on-line droplet size distributions (DSD) for a kerosene in water dispersion system with volume fraction range of 10-60%. They concluded that the effect of dispersed phase volume fraction on droplet size is insignificant in highly concentrated dispersions. Liu et al. (2017) investigated the effect of a non-ionic surfactant (i.e. Tween 80) concentration on DSD of oil in water dispersion in a stirred tank, experimentally and numerically. They concluded that with an increase in surfactant concentration, the mean droplet size was decreased, and the stability of emulsion enhanced. Zhou and Kresta (1998) used phase Doppler particle analyser (PDPA) by which the size, velocity, and concentration of droplets can be measured. Zhou and Kresta (1998) presented a review of available measurements and correlations for droplet size in liquid-liquid dispersion.

Boxall et al. (2010) determined a correlation between the measurement of the droplet size using two particle size measurements, particle video microscope (PVM) and a focused beam reflectance measurement (FBRM). In the study by Sprow (1967) on emulsification process of iso-octane and salt water, a correlation between mean and maximum size of the droplet size distribution was suggested. Similar observation was also reported by Brown and Pitt (1972), Calabrese et al. (1986), Lemenand et al. (2003) for emulsions with primary aqueous phase. In a study conducted by Wang et al. (2013), FBRM technique was used for evolution of droplet size for the mixing of oil-in-water dispersion to investigate the phase inversion for volume fractions of 10% - 60%.

2.3 Electrical Resistance Tomography (ERT) Applications

Tomography is an imaging technique that provide valuable results about hydrodynamic characteristics without physically interrupting the process (Williams and Beck, 1996). A tomographic technique is real-time measurements such as electromagnetic, electrical and acoustic. Selection of these tools relies on the purpose of measurement information and the objective of the experiment.

Electrical resistance tomography (ERT) has been widely used in past decades for both validating CFD and the analysis of mixing hydrodynamic (Bolton, 2004; Pakzad, 2007; Sharifi, 2013). ERT sends electrical signals across the tank and visualize the flow inside the tank by reconstruction of electrical conductivity signals. A set of electrodes with equal space between are positioned around the tank in horizontal planes (more information about ERT instrument can be found in **Chapter 3: Experimental Design and Procedures**.

ERT has a wide range of application in industry such as fluidized beds, stirred tanks (Williams and Beck, 1996), bubble columns (Wang et al., 2000), polymerization reactor (Kaminoyama et al., 2005), solid-liquid tanks (Hosseini et al., 2010, Tahvildarian et al., 2011), aerated reactors (Gumery et al., 2011; Hamood-ur-Rehman et al., 2012; Hamood-ur-Rehman et al., 2013; Babaie et al.,2015; Hashemi et al., 2016), and mixing of non-Newtonian fluids (Pakzad et al., 2008[a, b]; Patel et al., 2014[a, b]).

Kaminoyama et al. (2005) used this method to monitor the stability of reaction in the polymerization reactor. Holden et al. (1998) applied ERT for unsteady dynamic macromixing of miscible liquids with two types of impellers in a plant-scale reactor. Kim et al. (2006) used ERT to measure mixing time and dispersion velocity of dispersed phase in the mixing of two immiscible liquids. Solid-liquid filtration processes were investigated by ERT in study by Vlaev et al. (2000). This technique can provide, for instance, a mixing of non-Newtonian fluid inside the tank (Pakzad et al., 2013). A brief literature review of the most recent application of ERT is mentioned in **Table 2.1**.

Table 2.1.ERT applications in mixing process in stirred tanks.

Reference	Media	Objective	Achievements
Pakzad et al. (2008)	Non-Newtonian Liquid	Cavern size in non-Newtonian fluid with yield stress	The size of cavern was visualized.
Zhao et al. (2008)	Newtonian Liquid	The effect of UV lamps in photo-reactors on Hydrodynamics	The position of UV lamps was optimized.
Stanley (2006)	Solid-liquid	To evaluate the state of precipitation by measuring the solid concentration	Kinetic of precipitation was studied, solid concentration was achieved.
Richard et al. (2005)	Liquid Solid-liquid	Mixing process in pharmaceutical production reactor.	Geometry optimization
White and Doblin (2003)	Gas-liquid	Gas dispersion	Performance of A310 impeller, gas flow rate, and impeller speed were evaluated.
Wang et al. (2000)	Gas-liquid	Measuring gas holdup	Higher viscous fluid holds less gas

Among all available literature on the application of ERT in chemical processes, a gap in the application of ERT in mixing of two immiscible liquids can be found. In present study, ERT was used to imaging the flow process inside the tank by using conductivity tomograms. ERT was also used to define the homogeneity of the system by calculating the mixing index of dispersion. As mentioned earlier, mixing index is the average standard deviation between the volume fraction of dispersed phase at different positions in the tank. Since in a homogenous liquid-liquid dispersion, the volume fraction of the secondary phase in each volume element would be the same, therefore; the lower the mixing index, the more homogenous dispersion. Detailed information on calculation of mixing index using ERT conductivity data will presented in this chapter.

2.4 Degree of Homogeneity

2.4.1 Concentration Profile

Concentration profile is a method to study system homogeneity. Different methods for evaluating the concentration profile are available such as conductivity probe (Myers et al., 1994), electrical resistance tomography (Vlaev et al., 2000), and sampling (Wang et al., 2005). Tomography method was used in this study due to its efficiency and non-intrusive measurement.

2.4.2 Mixing Index

Typically, the effect of mixing on dispersion is studied by considering the variation in average volume fraction. Therefore, conductivities data from ERT measurements were related to volume fraction by using Maxwell equation (Maxwell, 1873) as follows:

$$\frac{\sigma_m - \sigma}{2\sigma_m + \sigma} = f\frac{\sigma_m - \sigma_p}{2\sigma_m + \sigma_p} \tag{2.1}$$

where σ is the conductivity, f is the volume fraction and subscripts m and p relate to continuous and dispersed phase, respectively. For calculation of mixing index, each ERT plane was divided into six concentric rings as shown in **Figure 2.1**. In each plane, the average volume fraction in each of the six rings is calculated from measured values of all elements on that ring. The standard deviation of each ring is then calculated for both planes. The volume fraction of dispersed oil therefore can be calculated for each plane in the radial direction across the six rings (radial mixing index MI_R) and/or in the axial direction (axial mixing index MI_z) for each annulus between two planes. An overall mixing index, MI_O, can be calculated as the standard deviation of all data in radial and axial profile (6 rings × 2 planes = 12 data points in this case). Overall mixing index can be calculated by Eq. (2.2) (Harrison et al., 2012):

$$MI_o = \frac{1}{\overline{X_{r,p}}}\sqrt{\frac{\sum_1^r \sum_1^p \left(X_{r,p} - \overline{X_{r,p}}\right)^2}{rp - 1}} \tag{2.2}$$

where MI_O is the overall mixing index for total mixing area, $\overline{X_{r,p}}$ is the average volume fraction of the 12 rings, $X_{r,p}$ is the individual ring volume fraction, and rp is the total number of rings for all planes.

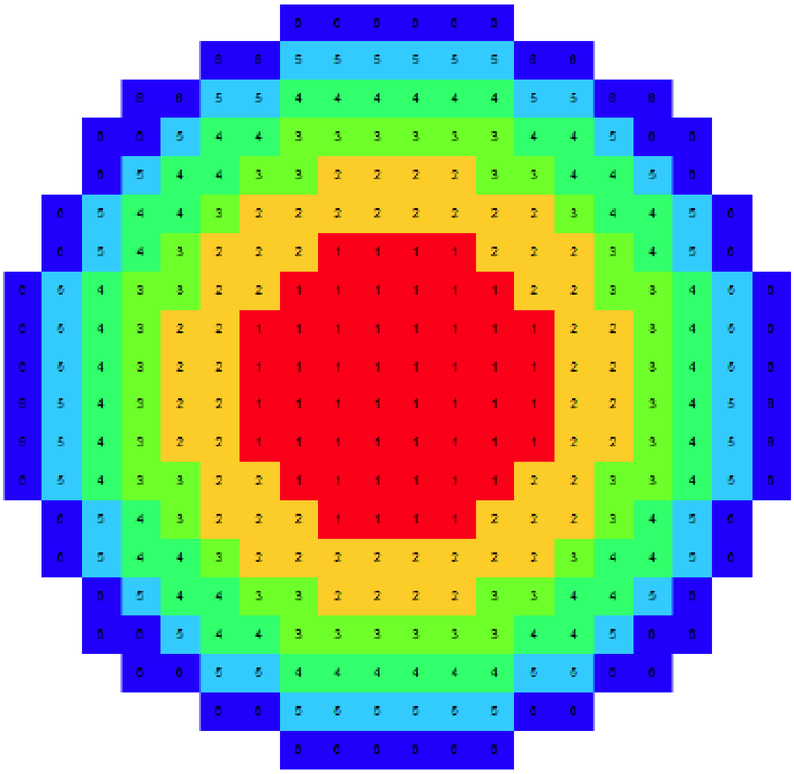

Figure 2.1. Schematic of the six rings on each plane used for mixing index calculation.

2.5 FBRM Applications in Stirred Tanks

Among various techniques for determining particle size, few can be used in-line or over a wide range of volume fractions (Allen, 1990). Ultrasonic technique has been used for particle size measurements, but the drawback of this method is the lengthy time measurement which makes it unsuitable for dynamic systems. Lab-scale laser diffraction instrument is another method that has been used in various studies (Bale and Morris, 1987; Hobbel et al., 1991). The problem with this instrument is that it cannot be used in plant-scale industry and the measurement can be taken for dilute systems. A typical way for transient drop size measurement is analyzing by withdrawing samples over time (Desnoyer et al., 2003). The drawback of this technique is that the drop size is not stabilized. 3D optical reflectance measurement (ORM) technique was used by Cull et al. (2002) and Lovick et al. (2005) in a liquid-liquid bio-catalytic reactor.

An alternative measurement technique is FBRM which is in-situ particle measurement instrument. FBRM has been used in many studies for crystallization (Poilov et al., 1997) or kinetics of flocculation (Sharma et al., 1994). FBRM measures the particle chord length distribution which is the straight line between two edges of droplet. A primary chord length distribution is constructed from the chord length measurements of many particles. The size range is divided into Cartesian or logarithmic intervals termed bins and the number count for each bin is reported. The number count is the number of particles intersected by the laser in its circular path over 10 seconds time interval. FBRM tracks the rate and degree of the change in chord length during measurement time.

2.6 Methods for Determining Particle Shape

As mentioned earlier, the interfacial area of droplets has a significant effect on heat/mass transfer ratio between phases. The surface of droplets may subject to different forces as they are exposed to the turbulent eddies. The deformation of droplet shapes has a fundamental impact on the estimation of the interfacial area of droplets (Fragkopoulos et al., 2017). The droplet shape has been neglected in almost previous studies for the simplification of models. However, the shape of the droplets could potentially be a critical factor for accurately predicting the flow characteristics in CFD simulations and defining more accurate breakage kernels. Most of the studies on particle shape are limited to solid particles and flocculation systems (Li et al., 2005; Petrak et al., 2015; Chen et al., 2017).

Due to the inherent irregularity of floc structures in both two and three dimensions, techniques for measuring the size and shape parameters are difficult (Jarvis et al., 2005). Some of the methods used for obtaining particle size are: microscopy, photography and image analysis, light scattering, and transmitted light. Physical sizing techniques such as sieving are inappropriate due to their delicate nature which cannot be a good representative of the system (Jarvis et al., 2005). Among available methods, on-line techniques such as light scattering method allows quick measurements to made and their non-intrusive nature as well as ability to monitor a wide range of particle size distributions (Jarvis et al., 2005). In this study, light scattering method by means of FBRM instrument was used to evaluate the size and shape of drops.

2.6.1 Calculation of Shape Factor using Chord Length Distribution (CLD)

In liquid-liquid dispersion, droplets are generally assumed spherical in shape due to the isotropic response of the sphere with lowest relative variance. However, in reality droplets' shape can depart from the ideal spherical shape. Droplets can be deformed and elongated because of the flow shear stress (Lovick et al., 2005). Small eddies of continuous phase which not have enough energy for breakage, can only deform the droplet's shape (Paul et al., 2004). In all instruments for particle size measurement, particle shape influences the physical phenomena utilized for size measurement (Li et al., 2005). Therefore, the small change in droplet's shape can have an effect on CLD (Sidiropoulos, 2014). In this regard, the circularity of the projected shape of droplets was calculated using FBRM chord length results.

In general, such geometries as sphere and spheroid can be observed in a liquid-liquid dispersion system (Nachtigall et al., 2016; Fragkopoulos et al., 2017). A spheroid is formed by rotating an ellipse about one of its main axes. A spheroid is an ellipsoid with two equal length axes when it is rotated about one of its axes. If the equatorial radius is greater than the polar radius, it is called oblate ellipsoid. The analysis of non-spherical particles has been limited to 2D shape analysis (Langston and Jones, 2001; Heath et al., 2005). In 2D shape analysis, a projected shape of a droplet can generally be described by an ellipse as follows:

$$(\frac{x}{a})^2 + (\frac{y}{b})^2 = 1 \tag{2.3}$$

where *x* and *y* are co-ordinates, and *a* and *b* are the semi-axis lengths with $a>b$. The droplet has spherical geometry if it has two equal semi-axis length ($a = b$). In fact, the ratio of $^a/_b$ shows how close the droplet projected shape is to a complete circular. To measure the proximity of a 2D projected shape to the outline of a circle, a circularity factor ($\psi_{p,pe}$) can be defined as (Petrak et al., 2015):

$$\psi_{p,pe} = \frac{2.\sqrt{\pi A_p}}{U_p} \leq 1 \tag{2.4}$$

where A_p and U_p are the droplet projection area and the perimeter of the droplet projected area, respectively. The circularity factor of droplet is ranging from 0 to 1. The value of 0 shows a straight line and the value of 1 shows a complete circular shape. The chord length distributions based on two particle shapes, sphere and spheroid, can be found in Petrak et al. (2015).

According to their study, the correlation between the aspect ratio $\left(\frac{a}{b}\right)$ with a non-dimensional shape parameter (*P*), for a range of 1≤ $^{a}/_{b} \leq 10$ can be defined as follows:

$$\frac{a}{b} = -55.35P^5 + 431P^4 - 1313.5p^3 + 1962.3p^2 - 1433.7P + 410.34 \tag{2.5}$$

where P is an area-weighted median of CLD /number-weighted median of CLD. In fact, the ratio of $^{a}/_{b}$ shows how close the droplet projected shape falls to a complete circular. The circularity of the droplets can be then calculated for values of $\left(\frac{a}{b}\right)$ using Eq. (2.6) as follows (Petrak et al., 2015):

$$\psi_{p,pe} = 1.125 - 0.119\left(\frac{a}{b}\right) + 0.0055(\frac{a}{b})^2 \tag{2.6}$$

where $\psi_{p,pe}$ is the circularity factor of a droplet. More mathematical details on using CLD for measuring shape factor can be found in a research by Petrak et al. (2015). As discussed earlier, the geometry of particles has an effect on measured chord lengths.

The measured CLDs can be further used to extend the droplet shape analysis by investigation on the probability or likelihood of having each shape (sphere or spheroid) in dispersion. In other words, we intend to set up the actual droplet size distributions of different geometries, i.e. sphere and spheroid, on the basis of CLDs data. There have been several studies conducted in order to derive analytical expressions for CLDs of the sphere and spheroid (Kendall and Moran, 1965; Kingman, 1965; Kellerer, 1971).

The CLDs can be obtained separately for each droplet shape. The chord length for sphere (Kingman, 1965) and spheroid (Kellerer, 1971) shape is calculated using Eq. (2.7) and (2.8), respectively:

for Sphere:

$$\frac{2s}{{d_1}^2} \quad 0 < s < d, d = diameter \tag{2.7}$$

for Spheroid:

$$\frac{2s}{c_1 {d_2}^2}\left[c_2 + \frac{\sqrt{1-e^2}}{4(e^{-2}-1)}\left\{\sqrt{\left|\frac{{d_2}^2}{s^2}-1\right|\left(\frac{{d_2}^3}{s^3}+\frac{3d_2}{2s}\right)+\frac{3}{2}ci\left(\frac{d_2}{s}\right)}\right\}\right]$$

$$ci(x) = \begin{cases} cos^{-1}(x) & for\ 0 \leq x \leq 1 \\ cosh^{-1}(x) & for\ x > 1 \end{cases} \tag{2.8}$$

$$c_1 = \frac{1}{2} + \frac{e^2}{2\sqrt{1-e^2}} ci\left(\frac{1}{e}\right), \quad c_2 = \frac{1}{4e^2} + \frac{3}{4} c_1$$

where *s* is the chord length, d_1 is the diameter of sphere, d_2 is the diameter of spheroid, and *e* is the elongation of the spheroid shape.

The CLD data measured by FBRM needs to be interpreted in some way to obtain information regarding drop size and shape. We aim to determine the expected diameter and the probability of having each shape. Li et al. (2005) presented a model to determine the CLD for a spherical particle. The model needs to be extended to allow for various particle shapes. For this purpose, the probability of having each shape can be assessed through mixture distribution. Using mixture distribution can be helpful to realize how different shapes (i.e. sphere or ellipsoid) contribute in making the data set of chord lengths, and what is their relative probability. In this regard, the mixture distribution of the aforementioned expressions (i.e. Equations (2.7) and (2.8)) should be optimized. The mixture distribution for both chord lengths of sphere and spheroid was coded using Python (Ver. 3.7.0). A mixture distribution is a mixture of multiple probability distributions. Mixture distribution is a useful way to show how the variables can be distributed for each distribution. More formally, a distribution *f(x)* is a mixture of *k* component distributions $f_1, f_2, \ldots, f_k$ if:

$$f(x) = \sum_{k=1}^{k} \lambda_k f_k(x) = \tag{2.9}$$

$$f(x; p, \mu_1, \mu_2, {\sigma_1}^2, {\sigma_2}^2) = \frac{p}{\sqrt{2\pi{\sigma_1}^2}} exp\left[-\frac{(x-\mu_1)^2}{2{\sigma_1}^2}\right] + \frac{1-p}{\sqrt{2\pi{\sigma_2}^2}} exp\left[-\frac{(x-\mu_2)^2}{2{\sigma_2}^2}\right]$$

where λ_k is the mixing weights, $\lambda_k > 0, \sum \lambda_k = 1$, *x* is chord length, *p* is the probability, μ is the mean, and σ^2 is the variance of normal distributions. The probability density function of mixture distribution can be obtained in the same way as mentioned in Eq. (2.9). A random variable *x* drawn from *k* different normal distributions with probability λ_k by specifying the component's probability density function as:

$$pdf(x_j) = \sum_{k=1}^{k} \lambda_k N(\mu_k, {\sigma_k}^2) \tag{2.10}$$

where *pdf(x)* is the probability density function, $\mu_k, {\sigma_k}^2$ are the mean and variance of distribution. For simplicity, we restrict our attention to present study where the mixture has two components. In other words, the random variable X (here X is chord length) is assumed to be generated from a mixture of two normal distributions if:

$$\begin{gathered} x\sim N(\mu_1, {\sigma_1}^2) \text{ with probability p;} \\ x\sim N(\mu_2, {\sigma_2}^2) \text{ with probability 1-p;} \end{gathered} \tag{2.11}$$

where $N(\mu\,, \sigma^2)$ is the normal distribution function, μ is the mean, and σ^2 is the variance of normal distribution.

Having said all above discussion on normal distributions and mixture distributions; we intend to use information theory to analyze the behavior of proposed CLD data sets. If we want to compute the probability that a certain CLD data set (our experimental droplet size that we measured by using FBRM) will be given from the actual droplet diameter of two shape geometries (i.e. sphere and spheroid); information theory can be used to optimize the mixture distribution in Eq. (2.9) with its constraints. Among different methods for optimization of mixture distribution such as expectation maximization (Dempster et al., 1977), and maximum likelihood estimation (Wu, 1983); maximum entropy method (Shannon, 1951) was used in this study. In this method, it is known that a gaussian random variable has the largest differential entropy of any random variable for a specified mean and variance (Politis, 1994). This method is prominent for modelling of time series observations and image processing (Politis, 1994). Based on the maximum entropy principles, the most appropriate distribution to model a given set of data is the one with highest entropy to satisfy all the constrains (Shannon, 1951) as follows:

$$p\mu_1 + (1-p)\mu_2 \geq \mu \tag{2.12}$$

$$p\mu_1 + (1-p)\mu_2 \leq \mu$$

As it is discussed earlier, the chord length distribution depends on the shape of the droplets. It is interesting to evaluate the mutual information of two gaussian distributions since it is a measure of their dependence on random variable (chord length). Maximizing the entropy of distribution shows how the chord length changes respect to the probability distribution parameters (Arellano-valle et al., 2013). The entropy of gaussian distribution is calculated as follows:

$$h(x) = -\int_{\mathbb{R}} f\ lnf = \frac{1}{2} log 2\pi e \sigma^2 \tag{2.13}$$

where *h(x)* is the entropy, *f* is the normal distribution function and σ is the variance of distribution. Therefore, the entropy of a normal distribution is related to the variance. Entropy gives a measure of uncertainty in distributions. Basically, using Entropy helps to understand how much mutual information and uncertainty each of these distribution shows in mixture distribution. More information on differential entropy and information theory can be found elsewhere (Ebrahimi et al., 2010).

Solving the mixture distribution by maximizing the entropy of distribution (refer to Eq. (2.13)) results in having **a)** the equivalent diameter and probability of having a shape of sphere; **b)** the equivalent diameter, elongation and probability of having spheroid shape in dispersion. Typically, when referring to a non-sphere drop size, choosing chord length for comparison between different particle shapes is not useful. The reason is that, unless the particle being measured is a sphere, the chord length can take a different value for the same particle. The distance between two random edges of a non-spherical particle can be different. The use of equivalent diameter allows the droplet to be assumed as a circle or sphere which makes a comparison easier between irregular drop forms. Therefore, rather than using chord length, an equivalent diameter should be used for comparative purposes.

2.7 Computational Fluid Dynamics (CFD)

Due to the limitation of experimental studies in terms of time and cost, using computational fluid dynamic (CFD) for modeling the flow behavior gained much interest over the years (Blazek, 2015). CFD is a helpful method to simulate the hydrodynamics, heat transfer, mass transfer, and related phenomena by using numerical methods. The fundamental steps of CFD modeling can be explained as:

1- Create the geometry and meshing,
2- Specify the fluid properties,
3- Specify the boundary conditions,
4- Set up the solver and solution methods, and
5- Compute and monitor the solutions.

An important part of running an accurate simulation are building the geometry and then, construction of the mesh with finite number of cells. After meshing the geometry; materials and their relative physical properties should be defined. Setting boundary conditions is an important task in order to get accurate result. In liquid-liquid dispersion, the droplet diameter was assumed to change since the droplets undergo breakage and coalescence phenomena due to the turbulence condition of the system (Coulaloglou and Tavlarides, 1977; Singh et al., 2009). One of the advantages of using CFD is measuring the particle size distribution (PSD) in dispersions. Population balance modeling (PBM) is one of the available models in CFD which can be applied to track the phenomena that occurs among the particles, such as nucleation, growth, aggregation, and breakage (Roudsari et al., 2012). One of the most challenging parts involved in population balance modeling is the deviation of measured droplet size from experimental results which stems from inherent dependency of available models on the particular empirical correlations and measurements.

Several methods have been investigated to track particle interactions and particle size distributions such as the standard method of moment (SMM) (Randolph and Larson, 1988), the Monte-Carlo method (Ramkrishna, 2000), the direct quadrature method of moments (DQMOM) (Marchisio et al., 2003), and the discrete method (Hounslow et al., 1988; Ramkrishna, 2000). The DQMOM method is very efficient for single component systems. The drawback of using this method is that only one property of particle can be determined which can be mass, moisture, volume, etc. (Roudsari et al., 2012). The DQMOM was applied by Buffo et al. (2012) for the simulation of gas-liquid dispersion in a tank equipped with a Rushton impeller. They achieved promising results for the mass transfer coefficient which agreed with the experimental data performed by Lakkonen et al. (2006). Moilanen et al. (2008) used inhomogeneous multiple size group (MUSIG) model and bubble number density (BND) method for the population balance modeling in an aerated bioreactor tank with three impellers. The MUSIG method coupled with the BND method provide bubble size distribution based on the dividing of the dispersed gaseous phase into *N* inhomogeneous velocity groups, and each of these groups is subdivided into *M* bubble size classes (Zwart and Frank, 2005). The BND approach was proposed for the first time by Wu et al. (1998) based on the prediction of variation of local bubble size.

Among all available models in PBM, discrete method was used in this study. In this method, the particle size distribution is presented in terms of a set of discrete size classes (Hounslow et al., 1988). The advantage of this method are its robust numeric and that it gives the PSD directly. Population balance equations are generally coupled with the fluid dynamics equations. In order to use the discrete method, the range of particle sizes should be defined a priori (Hounslow et al., 1988). The past decade has witnessed a huge growth of the discrete method for the population balance modeling of gas-liquid and liquid-liquid dispersions. To illustrate, Azargoshasb et al. (2016) used CFD-PBM with the discrete method to simulate gas-liquid dispersion in a bioreactor with eleven bin classes of arbitrary size to investigate the effect of hydrodynamic parameters on mass transfer, reaction behavior, and the Sauter mean diameter of biomass production.

The discrete method has been employed by Kerdouss et al. (2006) by introducing ten bubble bins for simulation of the bubble size distribution. Rathore et al. (2012) modeled an aerated bioreactor equipped with an e-blade impeller. They employed the discrete method with thirteen bins for population balance to evaluate the effect of impeller speed, gas flow rate, and liquid height on the mass transfer coefficient. In another study, Gelves et al. (2014), proposed the use of the discrete method to investigate the effect of turbulence, rotating flow, and breakage-coalescence in a stirred tank. The population balance was also applied to model the aggregation in a slurry system, as performed by Heath and Koh (2003). The Eulerian multiphase model coupled with the *k*-epsilon turbulence model was applied in their work to investigate the variation of the mean particle size over time. Agterof et al. (2003) presented the evolution of the mean droplet size over time in an oil/water emulsion with the help of moments of droplet size method in population balance. Roudsari et al. (2012) used the Luo's model coupled with the Eulerian approach and *k*-epsilon turbulence model for the mixing of water in an oil emulsion. Schütz et al. (2009) employed the mixture model and Lehr's approach for the modeling of the breakage in water-diesel separation found in hydro-cyclones. Their model successfully described the droplet coalescence and droplet breakage in liquid-liquid dispersion. Further research in this area by Srilatha et al. (2010) includes the droplet size distribution in a mixing tank for two different emulsion systems (water-in-tri butyl phosphate and water-in-xylene). However, they assumed that aggregation and breakage occurred only among the droplets with equal diameter. Similarly, Vladisavljevic et al. (2011) measured the droplet size distribution as a function of oil viscosity in an oil-in-water micro-channel. Boxall et al. (2010) focused on the effect of the continuous phase viscosity on the DSD of high volume fraction emulsions while a comprehensive study for dilute liquid-liquid dispersions has not yet been established. De Hert and Rodgers (2017) observed a transition from monomodal to bimodal distribution in droplet size as the viscosity of the dispersed phase increased.

2.7.1 Sequential or Simultaneous Solution Method

An important factor in simulation procedure is the solution method for coupling transport equations, turbulence, and population balance equations. In sequential approach, population balance equations are solved in the last step of calculations after solving the transport equations. On the other hand, in simultaneous approach all equations are solved at the same time during calculations (Roudsari et al., 2012). Since solving the population balance equations depends on hydrodynamic parameters such as turbulent kinetic energy, turbulent dissipation rate, and volume fraction; using sequential approach can results in inaccurate results because in this approach, the steady state values of aforementioned parameters are used in population balance equations. Therefore; using simultaneous approach, albeit more time consuming, can predict more accurate results (Roudsari et al., 2012).

2.7.2 Parallelization

In order to reduce extensive computational cost and time for calculating droplet size distribution rather than obtaining mean droplet size, parallelization in computation is recommended in literature (Schütz et al., 2009; Roudsari et al., 2012).

2.8 Design Consideration

The efficiency of the mixing process is highly dependent upon the design parameters. An important task to design an agitator is characterization of parameters of mixing process. Stirred tank geometry is an important parameter affecting the mixing process in term of droplet size distribution, homogeneity, mixing time, power consumption, and so on. Important variables in designing tank geometry are vessel, shaft, impeller, and baffles.

1. Vessel: the geometry of the tank such as rectangular, spherical, and cylindrical can affect the hydrodynamics of mixing process and mixture quality (Paul et al., 2004). An ideal ratio of liquid height to tank diameter for using one impeller is equal to one. For ratios more than one, number of impellers must be greater than one (Siddiqui, 1993).
2. Shaft: the position of the shaft entry can be on the top, side, or bottom of the tank. Using a shaft on the side enhance the mixing performance for solids with low settling velocities (Tatterson, 1991).
3. Impeller type: Choosing an appropriate impeller is important to achieve homogenous flow with less power consumption and in a short time. The efficiency of mixing depends on flow pattern induced by impeller which can be axial flow or radial flow (Chhabra and Richardson, 1999). In the first paper, we used Rushton turbine which is a radial flow. Radial flow impellers discharge the flow radially to the tank wall. They can provide high shear and turbulence with lower pumping which makes them an ideal agitator for liquid-liquid mixing (Paul et al., 2004). The pitch-blade impeller (PBT), an axial flow impeller, was used for mixing oil in water emulsion in the second paper. The axial flow impellers discharge the fluid in a vertical direction, i.e. upwards or downwards. The schematic figures of the stirred tank and impeller geometries will be shown in **Chapter 3**.

2.9 Research Objectives

According to the literature review presented in this study, little effort has been devoted to investigate the effect of different mixing parameters (such as impeller speed, viscosity of the fluid, and volume fraction) on droplet size distribution and mixing of dilute liquid-liquid dispersions. The application of ERT in the mixing of two immiscible liquids is not also fully evaluated yet. It was also found that the effect of operation conditions on droplet shape was not investigated and available literatures on particle shape analysis are limited to solid particles and bubble columns.

To achieve this objective, the first part of this study shows the development of the CFD model in conjunction with population balance modeling for mixing of water in oil emulsion. The CFD results were validated by experimental data of Boxall et al. (2010). With the help of CFD software package (FLUENT version 17.2), extensive calculations were performed to study the liquid-liquid dispersion in a stirred tank equipped with Rushton impeller.

The second part of this study is devoted to experimental study of dilute emulsions using both electrical resistance tomography (ERT) and focused beam reflectance measurement (FBRM).

CFD was used in this study to achieve correlations between the droplet size and hydrodynamic of the system. CFD results were validated by experimental data. Additionally; the analysis of drop shape was performed. The aim of this study was to investigate the effect of PBT impeller, impeller speed, volume fraction, and viscosity of dispersed phase on mixing characteristics and droplet size distribution of dilute liquid-liquid dispersion in stirred tank.

Experimental Design and Procedure

3.1 Experimental Setup for Second Study (presented in Chapter 5)

The experimental setup for the second part of this study was conducted in a transparent flat-bottomed cylindrical tank of 200 mm height and 200 mm inner diameter as shown in **Figure 3.1.** The tank is equipped with Pitched blade impeller (PBT) with a 95 mm off-bottom clearance. The impeller with 0.95 m diameter was driven using a 0.2 hp direct driven motor.

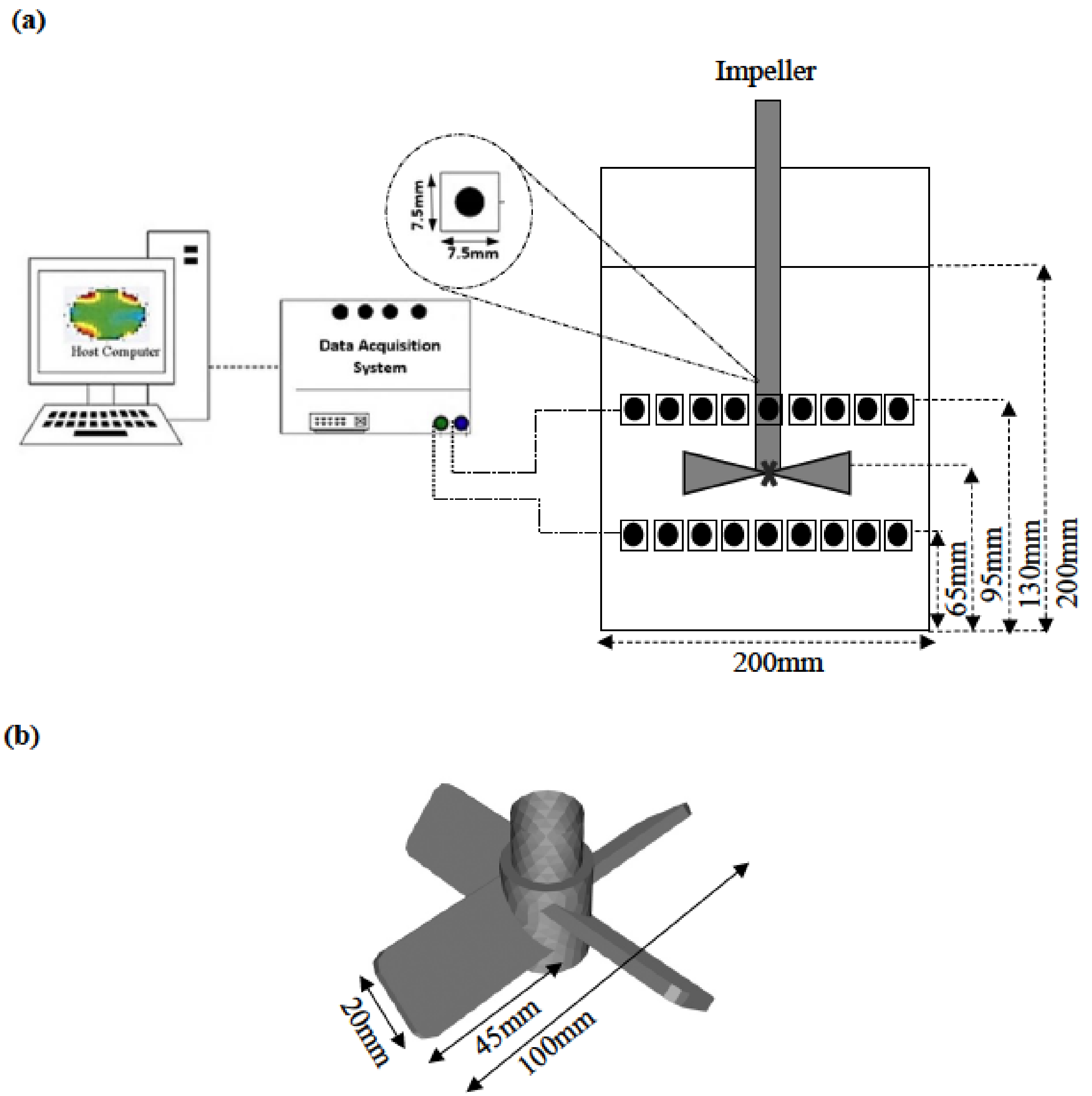

Figure 3.1. **(a)** The Schematic of the ERT system, **(b)** The Schematic of pitch-blade impeller (PBT) and its dimensions.

3.2 Material Properties

Two different oils, canola and linseed oils, were used as dispersed phase and water as a continuous phase. The physical properties of the oils are presented in **Table 3.1**. The conductivity of the tap water (with salt added) was measured as 822 μS/cm with conductivity meter (Thermo scientific, Orion star A212). A tensiometer equipped with a Du Nouy ring (sigma 701, Biolin Scientific) and OneAttension software was used to determine the surface and interfacial tension based on force measurements. A concentric cylinder rheometer (TA instrument) with a cup radius: 15mm, rotor radius: 14 mm, and height: 42 mm was used to perform the rheological studies.

Table 3.1. Physical properties of fluids at 20ºC and 1atm.

Fluid	Density (kg/m^3)	Viscosity (mPa.s)	Interfacial Tension (mN/m)
water	1000	1.0	-
canola oil	908	58.6	31.30
linseed oil	929	45.35	62.766

3.3 Experimental Condition

The effect of impeller speed, volume fraction of dispersed phase, and viscosity of dispersed phase were evaluated in this study. The experimental conditions are summarized in **Table 3.2**.

Table 3.2. Experimental conditions in second study.

Experimental Variable	Range
Impeller speed	175,200,225, and 250rpm
Volume fraction of dispersed phase	2.5%, 5.0%, 7.5%, and 10.0%
Viscosity of dispersed phase	45.35 mPa.s and 58.6 mPa.s

As can be seen in **Figure 3.1**, the mixing tank is equipped with an electrical resistance tomography (ERT) system. In the following section, a brief review on ERT is presented.

3.4 Electrical Resistance Tomography (ERT)

Tomographic technology is the process of collecting measurement signals from sensors located around a cross-sectional plane of an object. A host computer is used to collect the output signals and to reconstruct a conductivity tomogram of the cross-section observed by the sensors (Pakzad, 2007). The electrical tomography systems are the best choice for industrial processes due to their simplicity, rugged construction and high-speed response (Williams and Beck, 1996). This section is devoted to the design, structure, and operation of the ERT instrument.

In ERT instrument, multiple electrodes are located around the periphery of the process vessel with a direct contact to the fluid (Pakzad, 2007). A typical ERT contains three main parts named as: sensors, data acquisition system (DAS), and image reconstruction system.

3.4.1 Sensors

The tomographic picture of a cross-section strongly depends on the accuracy of the collected data by sensors acting as the most important part of the ERT systems. The sensitivity of the electrodes to small changes in the conductivity of the domain is important (Williams and Beck, 1996). Electrodes are fabricated from gold, platinum, stainless steel, and silver due to their good conductivity and resistance to corrosion in the process (Williams and Beck, 1996). Various factors can affect the data accuracy and image reconstruction of ERT such as: size of the electrodes, the position of the electrodes, and number of the electrodes per cross-section plane (Williams and Beck, 1996).

3.4.2 Data Acquisition System (DAS)

The data acquisition system collects the raw conductivity distribution data and send it to the host computer by performing the following functions: signal measurement, de-modulation, filtering and control; waveform generation and synchronization, voltage measurement stages between electrodes, and power supply (Mann et al., 1997).

3.4.3 Data Collection Strategy

Data collection strategy is an important part of the ERT measurement for building reconstructed images based on the full set of measurements (Pakzad, 2007). Four different strategies are available for data collection as follows:

1-The adjacent strategy,

2- The opposite strategy,

3- The diagonal strategy, and

4- The conducting boundary strategy.

-The Adjacent Strategy

In this method, the current is sent through two neighbouring electrodes and the voltages are measured for all successive pairs of neighboring electrodes and then repeated again. The total number of voltage measurements M is given by:

$$M = \frac{n(n-3)}{2} \tag{3.1}$$

where n is the number of electrodes. The advantage of using this method is the minimum hardware requirement and fast image reconstruction (Mann et al., 1997). This method was used as a data collection strategy in our experiment.

-The Opposite Strategy

This method is based on sending the current to two diametrically opposed electrodes and collecting the voltage reference from the electrode adjacent to the current-injecting electrode. The procedure is then repeated in clockwise direction for all pairs of electrodes. The drawback of this strategy is that it is less sensitive to the changes in conductivity close to the tank wall (Pakzad, 2007).

-The Diagonal Strategy

This method is based on sending current between two electrodes separated by large dimensions. For instance, the current is sent to electrode 1 as a current reference, and electrode 3, 5, ..., 15. Electrode 2 is acting as voltage reference, thus, the voltage is measured from electrodes left with respect to electrode number 2. According to this strategy, 104 independent measurements are taken for a full set of measurement. This strategy has a good sensitivity over the entire mixing tank (Pakzad, 2007).

-The Conducting Boundary Strategy

In this strategy, both current and voltage are sent between two electrodes with the aim of reducing the electromagnetic interference by earth-conducting boundary. More information about this strategy can be found elsewhere (Pakzad, 2007).

3.4.4 Image Reconstruction

Processing the conductivity data measured from vessel boundaries needs a suitable image reconstruction algorithm to process the raw data. Image reconstruction algorithm can be non-iterative or iterative depending on the desired accuracy of the image and required time for reconstruction. More information on image reconstruction methods can be found in Williams and Beck (1996).

- Non-iterative Image Reconstruction

In this process, the electrical conductivity of each pixel is determined within the image from the set of electrical measurements. This method is known as inverse problem. The conductivity distribution is determined from a finite number of boundary voltage measurements using linear back projection algorithm (LBP) (Pakzad, 2007).

3.5 ERT System

An ERT system (P2+ version8, Industrial Tomography System-ITS, Manchester, UK) was employed in this study. An ERT system comprises of electrodes, data acquisition system (DAS), and a computer. The mixing tank was equipped with two ERT sensor planes, one above (plane 1) and one beneath the impeller (plane 2) with 65 mm distance between. Each plane consisted of 16 equally spaced stainless-steel electrodes. The height, width, and thickness of the electrodes were 8 mm, 7 mm, and 1 mm, respectively. All electrodes were in direct contact with the fluid inside tank and were connected to the ERT system through coaxial cables. The conductivity distribution was measured through adjacent strategy (Pakzad et al., 2008b). The total number of independent measurements in the system, 104 individual measurements, can be obtained through: $M=n(n-3)/2$ where n is the number of electrodes and M is the total number of measurements. A conductivity tomogram is basically constructed using 316 pixels. Therefore, the total number of 632 (316 ×2 planes) non-invasive conductivity measurements per each sample measurement were presented for the conductivity distribution (Malik and Pakzad, 2018).

The P2+ ERT system employed in this study has the following specification: the frequency was 75 Hz-153.6 kHz (in 12 steps); the input-current injection ranges were 0 to 75 mA; the frame speed was 20 ms/frame; the output voltage ranged from -10 to +10 V; and the spatial resolutions of images were 3-5% of the vessel diameter. In this study, the current source was defined as 15 mA and the temporal resolution was about 1.2 s/frame. More details can be found in Malik and Pakzad (2018).

Figure 3.2 presents the mean conductivity measured by two ERT planes as a function of time. Reference measurement was taken prior to start mixing in order to eliminate the effects of the impeller and shaft. The first 50 seconds of measurements were measured and averaged as a reference frame. It can be seen in this figure, since both planes were placed in water phase (refer to **Figure 3.1**), both measuring planes displayed same conductivity (section I). As the impeller started its rotation and oil dispersed into the water, the conductivity of both measuring planes have been reduced (section II). Followed by adequate time given to the process in order to reach a steady state, the impeller was stopped rotating and two phases started to separate and therefore conductivity of both planes increased gradually (section III). During agitation process, a difference between the conductivities measured by the ERT planes can be noticed. Plane 2 with the lower conductivity shows that more oil droplets were presented in that area in compared to Plane 1.

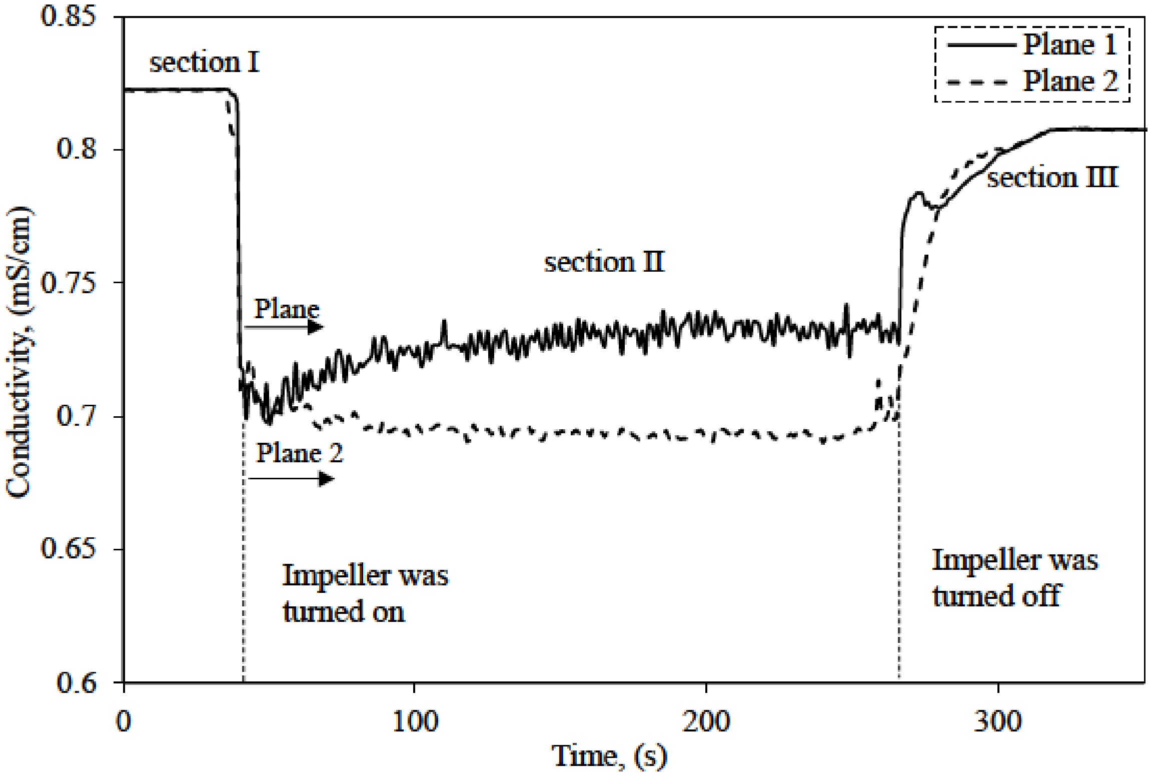

Figure 3.2.ERT conductivity data for two planes for canola oil (volume fraction of 2.5%) at 175 rpm.

3.6 Focused Beam Reflectance Measurement (FBRM) Probe

The FBRM probe used in this study is E25 particle size analyzer (Mettler-Toledo Lasentec) with probe size of 25 mm, scan diameter of 5 mm, and the scan interval of 10 s. The FBRM instrument contains three major parts: a measurement probe, an electronic measurement unit, and a computer for data acquisition and analysis. The focal point of the FBRM probe was set to default value of -20 µm. Heath et al. (2002) discovered the impact of the focal point position on the FBRM measurements, perceiving that changing the focal point more into the fluid increased the number of measured longer chords due to larger particles being less able to approach the measurement window.

The probe has a capability of detecting minimum particle size of approximately half the wavelength of the laser employed is employed which is 400 nm. When the measurements are about to be taken, the probe is inserted into the dispersion. Electronic unit generates the laser beam and it is projected through the sapphire window of the FBRM probe and focused just outside the window surface. This focused beam is then moved so it follows a circular path around the circumference of the probe window. A laser is then deflected by a rotating optical lens at a constant velocity of 2-6 m/s depending on the application so that particle motion has minor effect on measurement. As particles pass by the window surface, the focused beam will intersect the edge of a particle. The particle will then begin to backscatter laser light. The particle will continue to backscatter light until the focused beam has reached the particle's opposite edge. Backscattered light is collected by the FBRM optics and converted into an electronic signal.

A FBRM probe uses a discrimination circuit to identify the time period of backscatter from one edge of an individual particle to its opposite edge. Corresponding chord length is the product of the measured reflectance time and the laser scan speed. The counts of particles with different chord lengths make the chord length distribution (CLD). The chord length was obtained directly by using 90-log channels over the range of 1-1000 µm using IC-FBRM software. **Figure 3.3** depicts the schematic figure of FBRM setup used for particle size analysis.

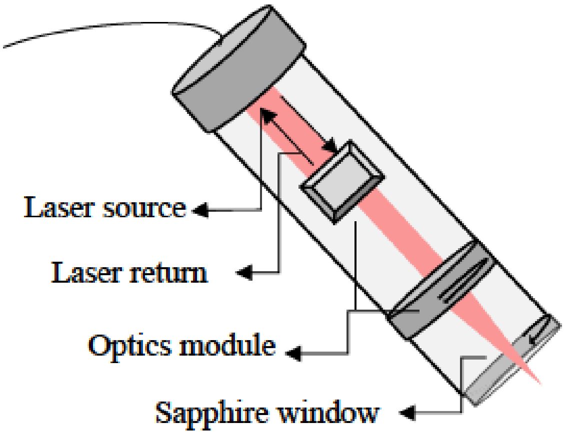

Figure 3.3. The schematic diagram of the FBRM laser probe.

3.7 Experimental Procedure

The volume fraction of dispersion for experiments varies between 2.5% - 10.0%. Each batch was prepared by dissolving 3.6 gr table salt in tap water as a continuous phase. Desired volume of oil was added and the fluid within the tank was allowed to sit for few hours to reach the room temperature. Before starting the measurements, the instrument current source (15 mA) and gain map were calibrated. A conductivity meter (Thermo scientific, Orion star A212) was used to measure the conductivity before each experiment run. Taking measurements continued until the conductivity of both sensor planes showed the same conductivity value which means that the flow was homogenous within the mixing tank.

For FBRM experiments, the tank was filled with water and specific volume fraction of the dispersed phase. It was found that adding salt to the water doesn't have significant effect on chord length measurements. Therefore, no salt was added for FBRM measurements. Prior to start droplet size measurement, the laser probe was calibrated by using distilled water. After calibration, the laser probe starts measuring the chord lengths and reporting the data after each 10s interval time.

CFD Model Development

4.1 Introduction

As mentioned earlier, the computational fluid dynamics (CFD) has been widely used recently to visualize mechanically stirred tanks. The main advantage of using CFD is the reduction in number of experiments that need to be done to get the same result. The commercial CFD package, FLUENT 17.2 (FLUENT Inc., USA), was used to discretize the governing equations numerically. FLUENT design modeller and meshing package was used to generate model and mesh of the mixing tank.

4.2 CFD Modeling of the Stirred Tanks

In order to model the Flow in stirred tanks, one can employ four general approaches available in CFD as: black box, sliding mesh, multiple reference frames, and snapshot approach. The multiple reference frame (MRF) and sliding mesh are more common models that have been used in FLUENT software (Pakzad, 2007).

4.2.1 The Black Box Approach

Due to dependency of this method on required boundary conditions on the impeller swept surface; this approach is limited by the availability of experimental data (Ranade, 2001). Using this approach for multiphase flows and to industrial scale reactors is not feasible, because having boundary conditions for such systems is not an easy task. Additionally; the drawback of this approach is that, this approach cannot evaluate the flow between the impeller blades (Pakzad, 2007).

4.2.2 The Sliding Mesh Approach

The most advantage of using sliding mesh approach (Luo, 1994; Murthy, 1993) is that dynamic simulations are carried out using two grid zones; one is attached to the tank and wall while the other is attached to the rotating impeller. The grid moves in this model as the impeller rotates in time relative to the wall, while the baffle region does not move (Pakzad, 2007). This model can provide useful information about the system in time-dependent solution method. Computational requirements for this method are greater compare to steady state methods (Roudsari et al., 2012).

4.2.3 The Multi Reference Frame (MRF) Approach

The MRF model creates two regions within the mixing vessel; one region around the impeller with distance above and below it. This impeller grid region is stationary, but the conservation equations are solved in a rotating frame. The rotation angular velocity of this region is the same as that of the impeller and shaft. Thus, the velocity of these elements is zero relative to the rotating frame. The second region is associated with the walls, tanks surface, and baffles. The conservation equations in this grid region are solved in the stationary frame. The values of conserved quantities are matched at the interface between these two grid regions (Luo, 1994).

4.2.4 The Snapshot Approach

This approach is based on taking snapshot of flow in a stirred tank while the position of the impeller is fixed (Ranade, 2001). In this method, the impeller blades are modeled as solid walls (Ranade and Dommeti, 1996). The flow is simulated using stationary frame in a fixed blade position. Simulations are performed at different blade positions and then the averaged results are obtained. The entire domain is divided into two regions. In the impeller region, time-dependent terms are approximated in terms of spatial derivatives. In the other region, time derivative terms in governing equations can be neglected due to their small values compared with other terms (Pakzad, 2007)

4.3 Multiphase Modeling

Two methods have been provided for the numerical calculation of multiphase flows in Fluent: the Euler-Lagrange approach and the Euler-Euler approach which will be discussed below.

4.3.1 Euler-Lagrange Approach

In this approach, the fluid phase is treated as a continuous phase by solving the Navier-Stokes equations and the dispersed phase is solved by tracking a large number of particles, bubbles, or droplets through the calculated flow field. This approach is useful in modeling of spray dryers, coal and fuel combustion, and some particle-laden flows (Fluent, 2006). This model is not appropriate for liquid-liquid mixing, fluidized beds or any application with considerable volume fraction of secondary phase (Fluent, 2006).

4.3.2 Euler-Euler Approach

In this approach, all different phases are treated mathematically as interpenetrating continua. The volume fraction of each phase is assumed to be a function of space and time and the sum of all volume fractions is equal to one (Fluent, 2006). Conservation equations for all phases are derived and have relation by providing constitutive relations obtained from empirical information. In ANSYS Fluent, three different Euler-Euler multiphase models are available: the volume of fluid (VOF) model, the mixture model, and the Eulerian model (Fluent, 2006).

4.3.2.1 The VOF Model

The VOF model is designed for two or more immiscible fluids where the position of the interface between the fluids is of interest. In the VOF model, a single set of momentum equations is shared by the fluids, and the volume fraction of each of the fluids in each computational cell is tracked throughout the domain. Applications of the VOF model include stratified flows, free-surface flows, filling, sloshing, the motion of large bubbles in a liquid, the motion of liquid after a dam break, the prediction of jet breakup (surface tension), and the steady or transient tracking of any liquid-gas interface.

4.3.2.2 The Mixture Model

The mixture model is applicable for two or more phases (fluid or particulate). The mixture model solves for the mixture momentum equation and prescribes relative velocities to describe the dispersed phases (Fluent, 2006). Applications of the mixture model include bubbly flows, sedimentation, and cyclone separators. The mixture model can also be used without relative velocities for the dispersed phases to model homogeneous multiphase flow (Fluent, 2006). For bubbly, droplet and particle-laden flows in which the volume fraction exceeds 10%, using either mixture model or Eulerian model provides more accurate results. As discussed earlier, the VOF model is useful when the simulation of stratified or- free-surface flows is of interest (Fluent, 2006). The decision between Mixture and Eulerian model has to be made based on the following guidelines:

1-If there is a wide distribution of the dispersed phases (that is, if the particles vary in size and the largest particles do not separate from the primary flow field), the mixture model may be preferable. If the dispersed phases are concentrated just in portions of the domain, the Eulerian model should be used (Fluent, 2006).

2- If the drag force between the phases applicable to the system is available, the Eulerian model can provide more accurate results. Otherwise; if the phase interaction is questionable, the mixture model may be a better choice (Fluent, 2006). For most cases with spherical particles such as our case, the Schiller-Naumann law is more than adequate.

3- Since the mixture model solves a smaller number of equations than the Eulerian model, it is better option for simple problems while the Eulerian model is more accurate (Fluent, 2006).

4.3.2.3 The Eulerian Model

The Eulerian model is the most complex of the multiphase models in ANSYS Fluent. It solves a set of momentum and continuity equations for each phase. Eulerian multiphase model has many applications including bubble columns, risers, particle suspension, and fluidized beds.

- Governing Equations in Eulerian Model

The continuity equation in Eulerian model is defined as:

$$\frac{1}{\rho_q}\left(\frac{\partial(\alpha_q\rho_q)}{\partial t}\right) + \nabla.(\alpha_q\rho_q\vec{v}_q) = 0 \tag{4.1}$$

And the momentum equation is defined as:

$$\frac{\partial}{\partial t}(\alpha_q\rho_q\vec{v}_q) + \nabla.(\alpha_q\rho_q\vec{v}_q\vec{v}_q) = -\alpha_q\nabla p + \nabla.\overline{\overline{\tau_q}} + \alpha_q\rho_q\vec{g} \quad + \vec{R}_{pq} + \vec{F}_q \tag{4.2}$$

where ρ_q is the density of the phase q, α_q is the volume fraction of phase q, $\vec{v}_q$ is the velocity vector of the same phase, $\vec{g}$ is the gravity acceleration, $\overline{\overline{\tau_q}}$ is the stress tensor, $\vec{F}_q$is the external force, $\vec{R}_{pq}$ is the interaction force between phases, and p is the pressure. Stress tensor and interaction forces in momentum equation can be calculated as follows:

$$\overline{\overline{\tau_q}} = \alpha_q\mu_q(\nabla.\vec{v}_q + \nabla.\overrightarrow{\nabla v}^T{}_q) + \alpha_q\left(\lambda_q - \frac{2}{3}\mu_q\right)\nabla.\vec{v}_q\bar{I} \tag{4.3}$$

$$\vec{R}_{pq} = \sum_{p=1}^{n} K_{pq}(\vec{v}_p - \vec{v}_q) \tag{4.4}$$

In the above equation; μ_q and λ_q are shear and bulk viscosity of phase q. $\bar{I}$ is the unit tensor and K_{pq} is the interphase momentum exchange coefficient. The exchange coefficient is defined as:

$$K_{pq} = \frac{\rho_p f}{6\,\tau_p} d_p A_i \tag{4.5}$$

where A_i is the interfacial area concentration. f is drag force and τ_p is the particle relaxation time which is defined as:

$$\tau_p = \frac{\rho_p d_p^2}{18\mu_q} \tag{4.6}$$

The importance of exchange coefficient is because of dependency of the rate of momentum exchange between two fluids.

Since the density ratio between two phases are close to one and the size of the droplets are small, the effect of the virtual mass force and the lift force in compared to the drag force are negligible in this study (Drew and Lahey, 1993). The drag coefficient proposed by Schiller and Naumann (Schiller, 1933) was used. The drag force correlation is as follows:

$$f = \frac{C_D Re}{24} \tag{4.7}$$

$$C_D = \frac{24(1+0.15Re^{0.687})}{Re} \qquad \text{for } Re \leq 1000$$

$$C_D = 0.44 \qquad \text{for } Re \geq 1000$$

where Reynolds number can be calculated based on the primary and secondary phase velocities:

$$Re = \frac{\rho_q |\vec{v}_p - \vec{v}_q| d_p}{\mu_q} \tag{4.8}$$

4.4 Turbulence Model in Stirred Tank

Using an accurate turbulence model coupled with population balance equations is an important factor results in accurate droplet size distribution. Among all various turbulence model in FLUENT package, we employed *k*-epsilon model. This model is applicable for a wide range of turbulent flows due to providing robustness and reasonable accuracy. The assumption in this model is that the flow is fully turbulent, and same as our case the effect of molecular viscosity is negligible.

The k-epsilon model was used in various CFD modeling projects to simulate multiphase mixing (Ranade, 2001). Among different available turbulence models, many researchers have used standard *k*-epsilon model due to its robustness and accuracy in predicting the turbulent parameters especially where the shear stresses are of interest (Marchisio et al., 2003, Kerdouss et al., 2006, Schütz et al., 2009). This model was derived for fully turbulent flow where the effects of molecular viscosity are negligible (Launder and Spalding, 1983). The disadvantage of using this model is that it doesn't give accurate results for unconfined flows such as aerodynamics applications.

In this study the standard *k*-epsilon model was used to simulate the turbulent flow within the emulsion cell. Many researchers such as Raikar et al. (2009) and Wang et al. (2005) have used this model and achieved satisfactory results. Two important parameters, i.e. k, the turbulence kinetic energy, and ε, the rate of energy dissipation is calculated using Eq. (4.9) and Eq. (4.10), respectively:

$$\frac{\partial}{\partial t}(\rho k) + \frac{\partial}{\partial x_i}(\rho k u_i) = \frac{\partial}{\partial x_j}\left[\left(\mu + \frac{\mu_t}{\sigma_k}\right)\frac{\partial k}{\partial x_j}\right] + G_k + G_b - \rho\varepsilon - Y_M + S_K \tag{4.9}$$

$$\frac{\partial}{\partial t}(\rho\varepsilon) + \frac{\partial}{\partial x_i}(\rho\varepsilon u_i) = \frac{\partial}{\partial x_j}\left[\left(\mu + \frac{\mu_t}{\sigma_\varepsilon}\right)\frac{\partial \varepsilon}{\partial x_j}\right] + C_{1\varepsilon}\frac{\varepsilon}{k}(G_k + C_{3\varepsilon}G_b) - C_{2\varepsilon}\rho\frac{\varepsilon^2}{k} + S_\varepsilon \tag{4.10}$$

where G_k and G_b are the source of turbulent kinetic energy due to the mean velocity gradients and due to buoyancy, respectively. The model constants were retained their default values as $C_{1\varepsilon} = 1.44$, $C_{2\varepsilon} = 1.92$, $\sigma_k = 1.0$, and $\sigma_\varepsilon = 1.3$. **Table 4.1** shows a brief review of available turbulent models with their related advantages and disadvantages.

4.5 Population Balance Modeling (PBM)

Various industrial fluid flow applications involve a secondary phase with a relative particle size distribution. The size distribution of particles, including solid particles, bubbles, or droplets, can evolve in conjunction with transport and chemical reaction in a multiphase system. The interactions between particles can be a combination of different phenomena like nucleation, growth, dispersion, dissolution, aggregation, and breakage. Thus, in multiphase flows involving a size distribution, a balance equation is required to describe the changes in the particle population, in addition to momentum, mass, and energy balances. This balance is generally referred to as the population balance (Fluent, 2006). The population balance model is a balance equation of species of different sizes and it is similar to the mass, energy and momentum balances (Randolph and Larson, 1988).

Population Balance Modelling (PBM) can track droplet coalescence and breakage of the dispersed phase and consider the particulate behaviour in the stirred tanks. Valentas and Amundson (1966) were the first who studied PBM for liquid-liquid dispersions to describe the drop size distribution for a continuous stirred tank. Hounslow et al. (1988) proposed a solution for the population balance equation in a well-mixed batch system. They used the moment transform to convert the population balance equations into ordinary differential equations. They employed population balance model to develop a numerical technique to model the growth and aggregation of particles in a suspension (Calcium oxalate monohydrate crystals) and simulated the formation of kidney stones. Their approach incorporated the calculation of the rate of change of total particle number and volume.

FLUENT provides different methods to in population balance modeling such as discrete method, inhomogeneous discrete method, standard moment, quadrature moment, and direct quadrature method of moment (DQMOM) method. Of a particular interest is the discrete method, in which the population balance is fully discretized into size intervals and the size distribution that is coupled with fluid dynamics is computed. This approach is also particularly useful when the range of particle sizes is known. Although, the discrete method is computationally expensive if the required number of intervals is large.

Droplet breakage and coalescence in an emulsion under turbulent flow regime in an agitated tank was investigated by (Coulaloglou and Tavlarides, 1977). They reported that the droplets coalescence rate was proportional to the droplets collision rate and the coalescence efficiency of the deformable drops. The breakage rate expression includes the breakage frequency, which represents the fraction of droplets splitting per unit time and the probability density function (PDF), which describes the distribution of the daughter droplets from the mother particle.

Hill and Ng (1995) developed a systematic method based on geometric ratios to use discretized population balance equations in the simulation of breakage processes in a batch system. Luo and Svendsen (1996) developed a theoretical model in order to predict breakup rates in turbulent liquid-liquid and gas–liquid dispersions. Each particle was assumed to break up into only two smaller particles (binary breakage) and the frequency of breakage was considered to be proportional to the energy level of the arriving eddies towards the particles. A few theoretical breakage mechanisms were proposed by Kostoglou et al. (1997) for dispersion systems using different geometrical ratios for particles; however, considerable simplification was made to eliminate the breakage frequency.

Table 4.1. Turbulence models and their description.

Turbulence Model	Description, Advantages, and Disadvantages
Standard k–ε	The most common used model, it is robust and quite cheap. Has been useful in engineering community for many years. It gives stable calculation and are very suitable especially for high Reynolds number. Not useful for swirling flows.
RNG k–ε	One developed model of the k–ε, this model improved results for swirling flows and flow separation. However, the disadvantage is that the model is less stable than standard k–ε model.
Realizable k–ε	Another adjusted version of the k–ε model, the realizable k–ε model correctly predicts the flow in round jets and is also well suited for swirling flows and flows involving separation.
RSM	Good estimates for all types of flows, including swirl, separation, and round and planar jets. Because equations for the Reynolds stresses are solved directly, it is more expensive than k–ε models. The reason is longer calculation time.
LES	Large eddy simulation is a transient formulation and offer good results for all flow systems. The model is based on Navier–Stokes equations and calculate large-scale turbulent fluctuations and models only the small-scale fluctuations. Because it is a transient formulation, the required more time for calculation than the RSM and k–ε s. In addition, a finer grid is looked-for to achieve the maximum benefit from the model and to accurately capture the turbulence in the smallest, sub grid scale eddies. Analysis of LES data require a bit higher advance planning and work.
k-ω	This is another two-equation model. In this model is an inverse time scale that is associated with the turbulence. Its numerical behavior is similar to that of the k- ε models.
DNS	DNS is conceptually the simplest approach to the problem of turbulence. An initial velocity field is assumed and iterated and the velocity field is evolved over time. DNS requires considerable resources. The scale for the resolution of small eddies is at least 1000 times smaller than those used in LES. DNS is the leading edge of turbulence research. So far only basic problems are being addressed. Applications of DNS can be used to study fundamental properties of turbulence, provide data to compare simplified turbulence models, and simulate other effects such as non-Newtonian phenomena.

4.5.1 Governing Equations in PBM

The Emulsification process is fundamentally coupled with droplet coalescence and breakage phenomena resulting in droplet size distribution. To have a stable Emulsion and improve the efficiency of the process, droplet coalescence should be avoided while droplet breakage should be increased (Liao and Lucas, 2009. In fact, the choice of model for particle interactions is of interest for decades. Alopaeus et al. (1999), Alopaeus et al. (2002), Nambier et al. (1992) have investigated the accuracy of different kernels on droplet size distribution in stirred tank for turbulent dispersions. A conjunction of Euler-Euler multiphase model and discrete method in population balance leads to the set of droplet size intervals which are assumed as an independent Eulerian phase (Schütz et al. 2009). The general population balance equation for secondary phase can be written as (Hagesaether et al., 2002):

$$\frac{\partial}{\partial t}(\rho n_{di}) + \left(\rho u_q n_{di}\right) = \rho[B_B - D_B + B_C - D_C]_i \tag{4.11}$$

where B_B and D_B on the right side of Eq. (4.11) denote birth and death due to breakage while B_C and D_C are representative of birth and death due to coalescence, respectively. The birth rate and death rate as results of breakage were defined by Eq. (4.12) and Eq. (4-13), respectively (Hagesaether et al., 2002):

$$\begin{aligned} B_B(i) = &\sum_{K=i+1, i\neq N}^{N} \Omega_B(\upsilon_K, \upsilon_i) + \sum_{k=1, i\neq N}^{i} x_{i+1,k}\Omega_B(\upsilon_{i+1}, \upsilon_K) \\ &+ \sum_{K=1, i\neq 1}^{i-1} \left(1 - x_{i,k}\right)\Omega_B(\upsilon_i, \upsilon_K), \qquad i = 1, \ldots, N \end{aligned} \tag{4.12}$$

$$\mathrm{D_B(i)} = \sum_{\mathrm{k=1}}^{\mathrm{i-1}} \Omega_{\mathrm{B}}(\upsilon_{\mathrm{i}}, \upsilon_{\mathrm{K}}), \qquad \mathrm{i = 2, \ldots, N} \tag{4.13}$$

The term $\Omega_B(\upsilon_i, \upsilon_K)$ is the rate of breakage for a droplet with size υ_i into droplet with the size of υ_K. The size of the daughter droplet will be calculated by Eq. (4.14):

$$\upsilon_j = x_{i,k}\upsilon_{i-1} + \left(1 - x_{i,k}\right)\upsilon_i \tag{4.14}$$

$$x_{i,k} = 2^{1+k-i}$$

The number density function has been used in this study which is equal to:

$$f(m, t, \vec{x}) = \frac{dN}{dxdydzdm} \tag{4.15}$$

The number density function is defined as finite number of particles, here as droplet, per size of the interval and per volume.

The accuracy of different kernels on droplet size distribution in stirred tanks for turbulent dispersions have been investigated in several studies (Nambier et al., 1992, Alopaeus et al., 1999 and 2002). Many researchers have proposed various empirical, or semi-empirical models to get valid results for particle size distribution by population balance simulation (Luo and Svendsen, 1996; Lehr, 2001; Ghadiri and Zhang, 2002). Breakage in droplets was modeled using Lehr's breakage model (Lehr. 2001). Lehr (2001) defined a breakage model for liquid-gas dispersion based on the interaction of inert forces. Schütz et al. (2009) used the Lehr breakup model for liquid-liquid separation in hydrocyclone, and they achieved satisfactory droplet size distribution. The equation for breakage rate according to Lehr's model is expressed as:

$$\Omega_B\left(\acute{d}\right) = 0.5.\,(\acute{d})^{5/3}(\frac{\rho_c}{\sigma})^{7/5}\,\varepsilon^{19/5} exp\left(-\frac{\sqrt{2}}{(\acute{d})^3}(\frac{\sigma}{\rho_c})^{9/5}\frac{1}{\varepsilon^{6/5}}\right) \tag{4.16}$$

In above equation, the droplet breakage in liquid-liquid system is caused by turbulent eddies smaller than $\acute{d}$, the diameter of mother droplet. The breakage mechanism profoundly depends on the condition surrounding the droplet. External stresses from eddies of continuum destroy the fluid particle; whereas, the surface stress of the particle as well as viscous stress of the fluid inside the droplet resist distortion (Revankar, 2001). The daughter particle size distribution of Lehr (2001) based on lognormal distribution was used as follows:

$$\beta\left(d,\acute{d}\right) = 180\,\left(\frac{d^2}{\acute{d}^3}\right)\left(\frac{d^3}{\acute{d}^3}\right)^2\left(1-\frac{d^3}{\acute{d}^3}\right)^2 \tag{4.17}$$

where d, $\acute{d}$, ρ_c, σ, and ε are the mother droplet size, daughter droplet size, density of continuous phase, and turbulent dissipation rate, respectively. Eq. (4.17) describes the impact of the turbulent energy dissipation rate on the generation of daughter droplet diameter of $\acute{d}$ from mother droplet size of d. In order to get accurate droplet size distribution, the normalized function of daughter droplet size distribution must be equal to one as shown in Eq. (4.18):

$$\int_{m_{min}}^{\acute{m}} \beta(m,\acute{m})dm = 1 \tag{4.18}$$

More details about Lehr's breakage mechanism can be found in Lehr (2001). The coalescence would seem to be defined by the priori assumption of having a sufficient rate of collisions between droplets with diameter of d and d'. Coalescence between droplets depends on two major factors; collision rate and coalescence efficiency (the ratio of successful collisions to all possible collisions). Another key parameter in droplet coalescence is the liquid film thickness between two interacting droplets (Coulaloglou and Tavlarides, 1977). At the critical film thickness, the film breaks, droplets join together, and coalescence happens. In other words, the contact time between two droplets must be higher than the drainage time (Liu & Li, 1999). In the inertial subrange where inertial stresses control droplets' interactions, turbulent eddies make droplets into contact (Rueger and Calabrese, 2013).

The birth rate and death rate for droplets due to coalescence are defined as follows:

$$B_C(i) = \sum_{j=1, i\neq N}^{i-1} x_{i,j}\Omega_{ag}(v_i, v_j) + \sum_{j=1}^{i-1}(1 - x_{i-1,j})\Omega_{ag}(v_{i-1}, v_j), \;\; i = 2, \dots, N \tag{4.19}$$

$$D_C(i) = \sum_{j=1}^{N-1} \Omega_{ag}(v_i, v_j) + \Omega_{ag}(v_i, v_j), \quad i = 2, \dots, N \tag{4.20}$$

The Luo (1993) model was applied for the coalescence rate. This model is the function of collision frequency and collision probability as follows:

$$\Omega_{ag}(V_i, V_j) = \omega_{ag}(V_i, V_j) P_{ag}(V_i, V_j) \tag{4.21}$$

where $\omega_{ag}(V_i, V_j)$, the collision frequency, is defined by Eq. (4.23) and $P_{ag}(V_i, V_j)$ is the probability of the collision resulting in coalescence.

$$\omega_{ag}(V_i, V_j) = \frac{\pi}{4}(d_i + d_j)^2 n_i n_j \bar{u}_{ij} \tag{4.22}$$

where $\bar{u}_{ij}$ is the characteristic velocity of collision between two droplets, and $n_i \; and \; n_j$ are number densities.

$$\bar{u}_{ij} = (\bar{u}_i^2 + \bar{u}_j^2)^{1/2} \tag{4.23}$$

where

$$\bar{u}_i = 1.43(\varepsilon d_i)^{1/3} \tag{4.24}$$

The aggregation probability equation is defined by Eq. (4.25) as follows:

$$P_{ag} = exp\left\{-c_1 \frac{\left[0.75(1 + x_{ij}^2)(1 + x_{ij}^3)\right]^{1/2}}{\left({}^{\rho 2}/_{\rho 1} + 0.5\right)^{1/2}(1 + x_{ij})^3} We_{ij}^{1/2}\right\} \tag{4.25}$$

where $x_{ij} = {}^{di}/_{dj}$. By considering the above condition, the dynamic pressure difference around the droplet against its surface stress can determine whether or not the droplet will resist to break in the system. The ratio of dynamic pressure to particle surface stress is called Weber number $We = {}^{\tau_i}/_{\tau_s}$ (Liao and Lucas, 2009). This number indicates whether the kinetic energy or surface tension of the droplet is dominant. The Weber number (*We*) presented in Eq. (4.26) is defined by the following equation:

$$We_{ij} = \frac{\rho_l d_i (\bar{u}_{ij})^2}{\sigma} \tag{4.26}$$

Since the design of the tank involves moving parts around the impeller, many authors have used either a multiple reference frame (MRF) (Roudsari et al., 2012; Rathore et al., 2012; Pakzad et al., 2008; Luo et al., 1994; Fan et al., 2010) or the sliding mesh method (Wutz et al., 2016, Kazemzadeh et al., 2016). Since the sliding mesh approach, albeit more accurate, is time consuming, we employed the MRF approach to capture the motion in the vicinity of the impeller. The standard wall function was considered as a boundary condition for the shaft and impeller (Launder and Spalding, 1983). The symmetry boundary condition was used on the liquid level. Coalescence between two bin sizes with number density n_i and n_j can be happened due to buoyancy, laminar shear, and turbulence. The dominant source of aggregation in this case is turbulence (Schütz et al., 2009). Schütz et al. (2009) used Lehr breakup model for liquid-liquid separation in hydro cyclone and they achieved satisfactory droplet distribution.

4.5.2 Solution Methods for Population Balance Modeling

- The Discrete Method

In this method, the size distribution is divided into a finite number of size intervals. This method computes the particle size distribution directly. This method is useful when the range of particle size, minimum and maximum, is known a priori. The population can be discretized with a relatively small number of size intervals and the size distribution is coupled with fluid dynamics. The disadvantage of this approach is that it is time consuming if a large number of intervals is needed (Fluent, 2006). This approach has been used in our simulation. More information on population balance modeling can be found on FLUENT population balance modeling guide (Fluent, 2006).

4.6 Boundary Conditions

In order to solve the conservative equations mentioned above, the boundary conditions and initial values of parameters should be specified. Commonly used boundary conditions are discussed below:

1. Inlet; at inlet boundaries, information about the velocity or pressure, mass flows, physical properties and so on depending on the geometry and the specific condition of the study case would be used.

2. Outlet; at outlet boundaries, the gradients in the direction normal to the outlet surface are zero for all variables except pressure (Ranade, 2001). If the gradients at the outlet boundary are not zero; use of this boundary condition would not be suitable.

3. Walls; a 'no slip' boundary condition can be used at wall boundaries of the domain (Patankar et al. 1980). This means that the velocity of fluid velocity is equal to that of the surface of the wall and the normal velocity is zero.

4. Symmetry; the normal velocity is set to zero at the symmetry surface and the normal gradients of all variables except normal velocity are set to zero. It means that the convective or diffusive flux across the boundary is zero (Versteeg and Malalasekera, 2007).

Wall boundary condition and symmetry boundary condition were used in our study.

4.7 CFD Model Development

In this section, the geometry, meshing, and the general applicable modeling features that applied in both studies are presented.

Since the design of the tank involves moving parts around the impeller, many authors have used either a multiple reference frame (MRF) (Roudsari et al., 2012; Rathore et al., 2012; Pakzad et al., 2008; Luo et al., 1994; Fan et al., 2010) or the sliding mesh method (Wutz et al., 2016; Kazemzadeh et al., 2016). To evaluate the motion in the tank, a simulation should be time dependent. As mentioned earlier, in order to track the dynamic parameters in the tank, either the MRF approach or sliding mesh approach can be used. Since the sliding mesh approach, albeit more accurate, is time consuming, we employed the MRF approach to capture the motion in the vicinity of the impeller. The past years have witnessed a huge growth in the use of the MRF method for the similar mixing geometry (Kerdouss et al., 2006; Pakzad et al., 2008; Patel et al., 2010) and they got accurate results. The standard wall function was considered as a boundary condition for the shaft and impeller which rotate with same velocity (Launder and Spalding, 1983). The symmetry boundary condition was used on the liquid level.

The SIMPLE algorithm was used for pressure-velocity coupling. The second-order discretization scheme was used for all equations except volume fraction. For volume fraction discretization, the QUICK scheme was used which is more accurate for the swirling/rotating fluid (Rathore et al., 2012). The convergence was checked for all 30 equations (one continuity equation, three momentum equations, four volume fraction equations, two turbulence equations, and twenty equations for water bin fractions). FLUENT software (version 17.2) was employed to solve both hydrodynamic and population balance equations. The time step of 0.01s has been chosen to solve all equations for 35s. To use the simultaneous solution method, supercomputing facilities of HPCVL was used. Each simulation was partitioned into 24 parts and each CPU was then used for each part.

4.7.1 Geometry

ANSYS design modeller (version 17.2) was used for defining the mixing tank configuration of both studies. The geometries of the mixing tanks in both studies are shown in **Figure 4.1**.

4.7.2 Grid Generation

ANSYS meshing (version 17.2) was used to discretize the domain. In first study, the reactor was discretized with unstructured tetrahedral mesh consisting of 300,000 cells. Geometry was meshed with both advanced size functions and inflation layers to capture curvature and boundary layer gradients around the impeller in rotating frame.

In second study, the sweep method was applied to mesh the mixing tank. In this method, the PBT impeller and MRF volume were discretized with tetrahedral cells however the rest volume was meshed with hexahedral cells. We used biased-edge sizing to mesh around the impeller and have smooth increase in the size of hexahedral cells from MRF interface to the outer body of the tank. Geometry was meshed up to 700,000 cells with both advanced size functions and inflation layers to capture curvature and boundary layer gradients around the impeller in rotating frame.

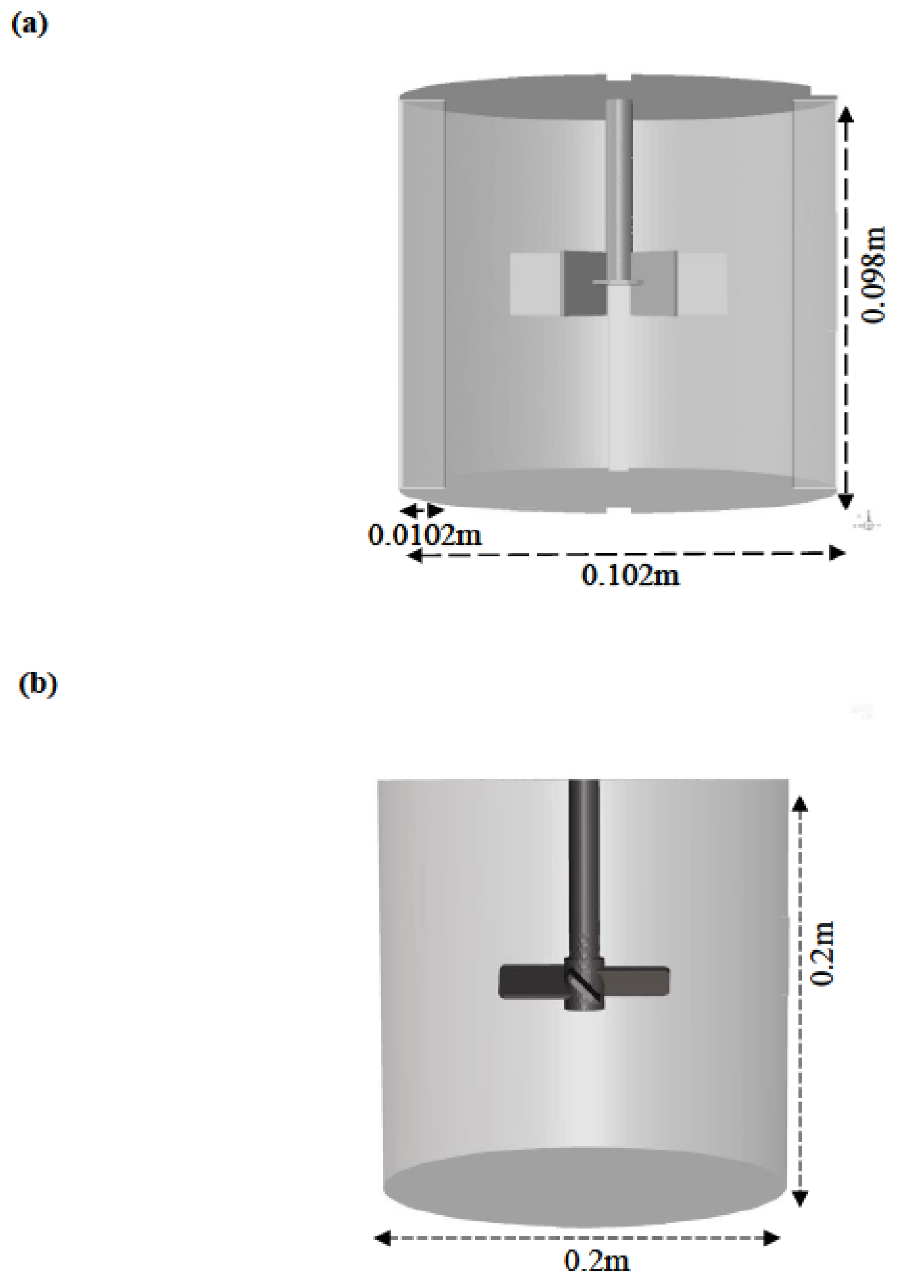

Figure 4.1. Geometries of the mixing tanks for: **(a)** First study (**Chapter 5**); **(b)** Second study (**Chapter 6**).

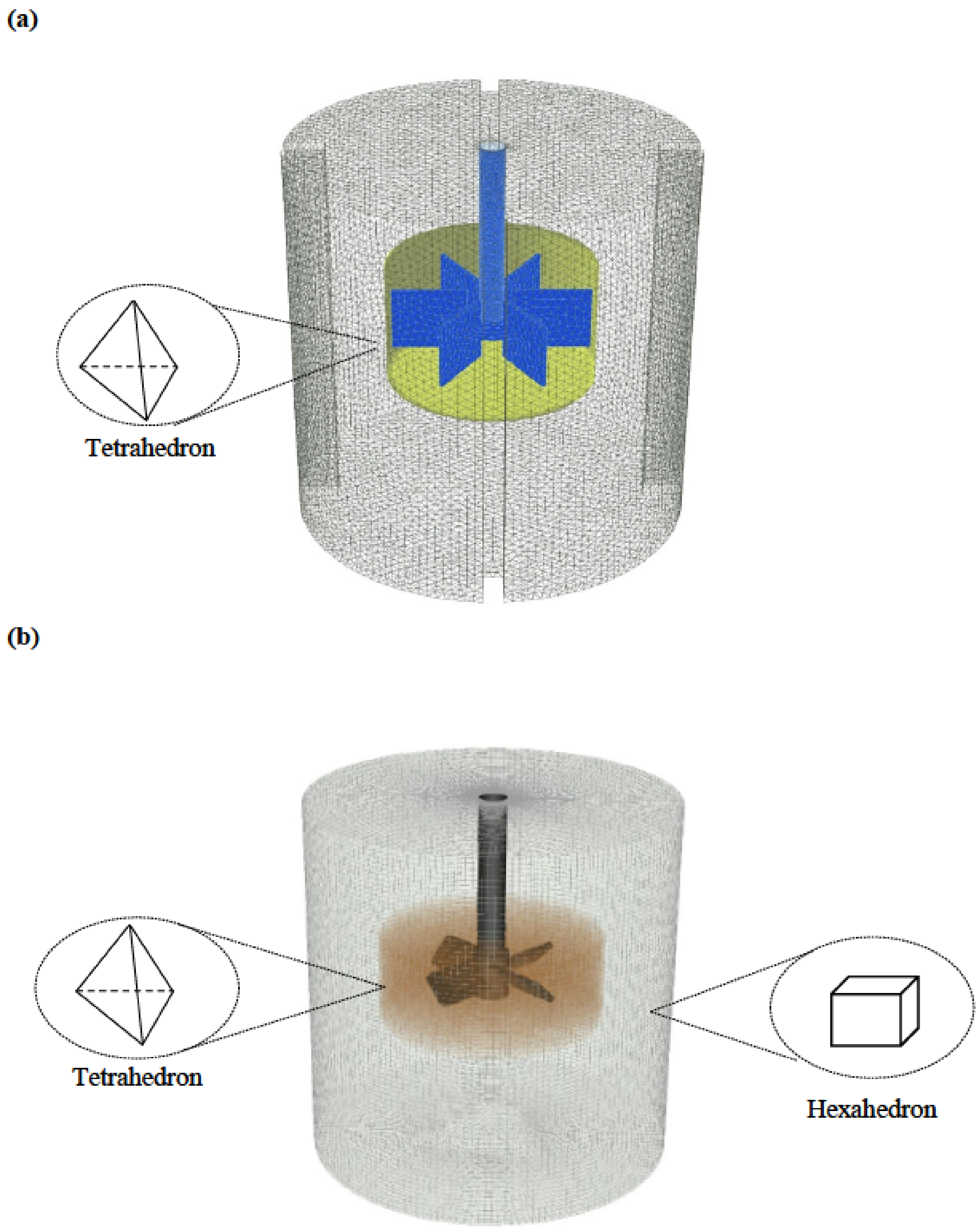

Figure 4.2. Mesh grid for: **(a)** First study **(Chapter 5)** using tetrahedral cells, **(b)** Second study **(Chapter 6)** using sweep method consisting of tetrahedral and hexahedral cells.

4.7.3 Grid Independence Check

The mesh independency check was performed for both studies to ensure the full development of the flow and accuracy of simulation results. The result of mesh independency check is shown in **Figure 4.3**. In first study, the variation in the average of the velocity magnitude of primary phase on an arbitrary line, 10 mm below the impeller was calculated for different grid size at volume fraction of 10.0% and impeller speed of 300 rpm (refer to **Figure 4.3(a)**). In this regard, four different mesh sizes were generated as 60,000, 150,000, 300,000, and 600,000. The discrepancy between them was calculated in terms of the root-mean-square (RMS) deviation (Arratia et al. 2006; Pakzad et al. 2008) as shown in Eq. (4.28). The difference between velocity magnitude for 300,000 and 600,000 mesh was 3.84%.

In second study, the average of turbulent kinetic energy on a line,10mm below the impeller was calculated for three different grid sizes: 300,000cells as a coarse grid, 700,00 cells, and 1,350,000cells as fine grid at 10.0% volume fraction and impeller speed of 200 rpm (refer to **Figure 4.3(b)**). The average turbulent kinetic energy for a coarse grid is clearly different from the other mesh cases. The RMS deviation for the value of turbulent kinetic energy for 700,000 cells and 1,350,000 cells was 2.44%. Therefore, the grid with 700,000 cells was considered for all simulations.

$$RMS = \frac{\left[\frac{1}{n}\sum_{1}^{n}(x_1 - x_2)^2\right]^{1/2}}{\left[\frac{1}{n}\sum_{1}^{n}(x_2)^2\right]^{1/2}} \tag{4.27}$$

where *n* is the number of nodes and *x* is the variable of interest.

(a)

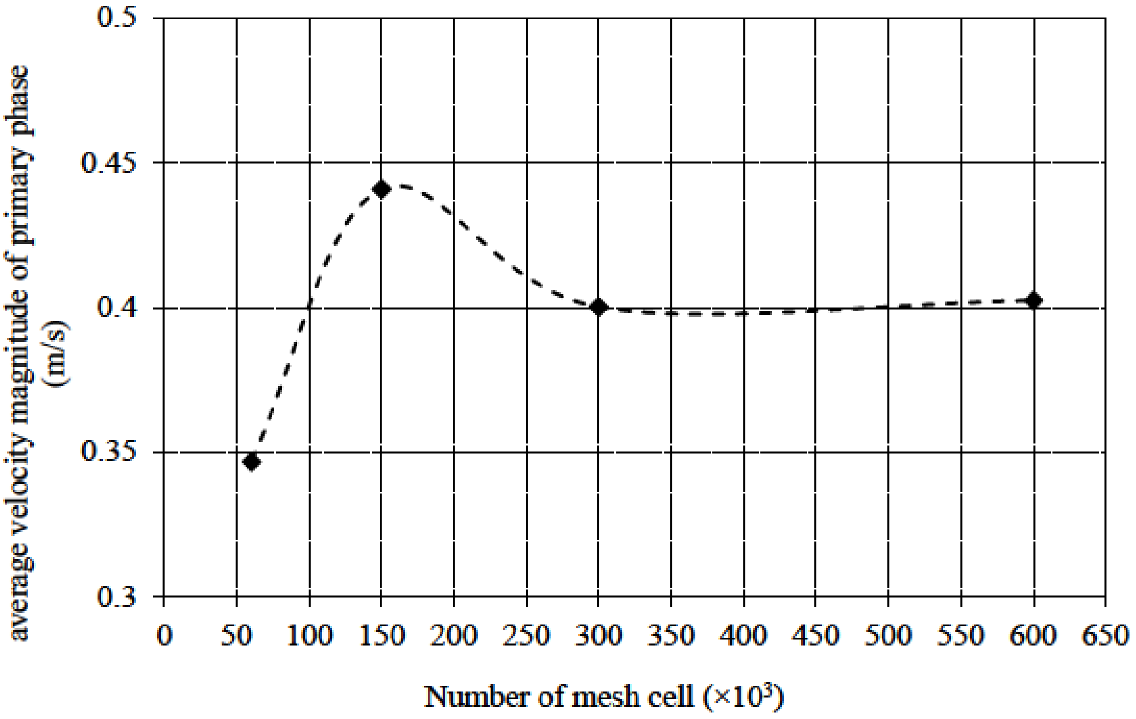

(b)

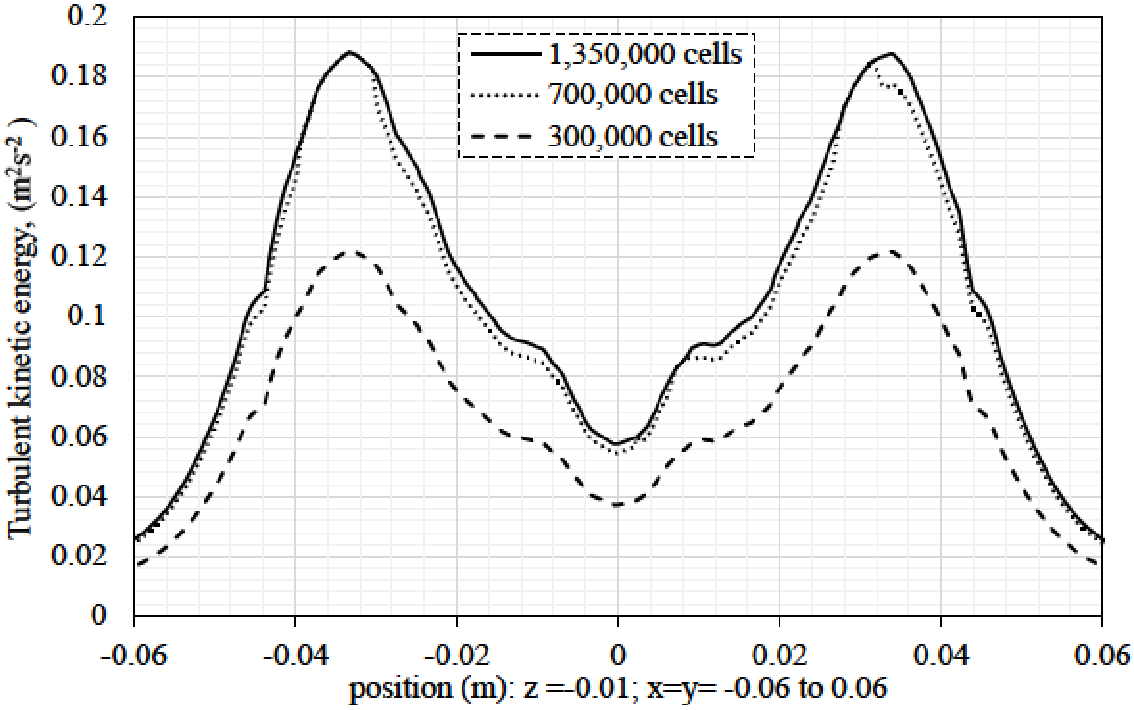

Figure 4.3. Effect of grid numbers on: **(a)** Average velocity magnitude (first study), **(b)** Average turbulent kinetic energy in horizontal position (second study).

4.8 Solution Procedure

Fluent (version 17.2) was employed to solve all transport and population balance equations for unsteady-state condition. All transport equations were integrated using control volume method. Standard wall function was considered as wall treatment (Launder and Spalding, 1983). The symmetry boundary condition was used on the liquid level. The SIMPLE algorithm was used for pressure-velocity coupling. The second-order discretization scheme was used to calculate the face fluxes in the momentums and for all equations except volume fraction. For volume fraction discretization, the QUICK scheme was used which is more accurate for the swirling/rotating fluid (Rathore et al., 2012). Governing transport equations were integrated over small control volumes which results in an algebraic linear system.

The Gauss–Seidel iterative method and the Algebraic Multi-Grid method (AMG) were then used to solve the algebraic linear equations. The simulation started by setting all velocity components equal to zero. Population balance equations along with transport equations were solved simultaneously with the time step of 0.01s, number of time steps 122,500, and maximum iteration per time step of 35. The initial condition for the turbulent energy dissipation was equal to 1 m^2/s^3 and for turbulent kinetic energy was equal to 1 m^2/s^2. The convergence was checked by monitoring the residual of all equations, and the average volume fraction of dispersed phase. To use the simultaneous solution method, supercomputing facilities of HPCVL was used. Each simulation was partitioned into 24 parts and each CPU was then used for each part.

Droplet Size Distribution and Mixing Hydrodynamics of Dilute Emulsions by Coupled Computational Fluid Dynamics (CFD) and Population Balance Modeling (PBM)

5.1 Abstract

In this chapter, computational fluid dynamic (CFD) coupled with the population balance modeling (PBM) have been employed to model and simulate mixing of water in crude oil emulsion in a stirred tank. An Eulerian multiphase model and standard *k*-epsilon turbulence model incorporating with population balance discrete method were employed to simulate the flow field and droplet size distribution in a stirred tank. The effect of impeller speed, volume fraction of dispersed phase, oil viscosity, and number of bin fractions on droplet size distribution have been investigated in this work. The experimental droplet size distribution reported by (Boxall et al., 2010) was employed to validate the CFD simulation at different impeller speed for water as a secondary phase and crude oils as a primary phase. This chapter is organized as follows:

5.2. Introduction
5.3. Results and Discussion; and
5.4. Concluding Remarks.

5.2 Introduction

The mixing tank modeled in this study is a flat-bottom cylindrical tank with the internal diameter of 0.102 m. The liquid height in the tank is 0.098 m providing approximately 0.81 L volume of the fluid. A Rushton impeller with a diameter of 0.0508 m was attached to a central shaft with an off-bottom clearance of 0.0515 m and four equal-spaced baffles were mounted to the wall (refer to **Figure 4.1**). The tank was filled with the crude oil as the primary phase and tap water as the secondary phase. Four different crude oils have been tried in this study. The physical properties of the fluids are presented in **Table 5.1**. The volume fraction of the secondary phase (i.e. water) was varied from 2.5% to 15.0% (i.e. 2.5, 5.0, 7.5, 10.0, and 15.0%). Three levels for impeller speed as 300 rpm, 400 rpm, and 600 rpm were considered.

Table 5. 1. Physical properties of the fluids at standard condition (Boxall et al., 2010).

Fluid	Density (kg/m^3)	Viscosity (cP)	Interfacial Tension (mN/m)
Water	1000	1.0	-
Pure Conroe oil	842	3.1	20
Troika oil	869	20.0	11
20% Conroe oil- 80% brightstock	886	262.0	20
Petronius	883	100.0	13

5.3 Results and Discussion

The sufficient number of bin fractions in discrete method is a prominent key for population balance modeling (PBM). Small number of bin classes leads to inaccurate DSD while using large numbers of bin classes is computationally expensive. Among various distribution equations such as single probability density function (Zhuo and Kresta, 1998), linear normal distribution (Calabrese et al., 1986), and logarithmic normal distribution (Boxall et al., 2010), the logarithmic normal distribution (as presented by Eq. (5.1)) was applied in this study to present DSDs.

$$f_d(X) = \frac{1}{\sqrt{2\pi}\sigma X} exp\,(-\frac{(lnX - \mu)^2}{2\sigma^2}) \tag{5.1}$$

where X is the bin fraction size, σ is the standard deviation, and μ is the median of the distribution defined as follows:

$$\sigma = \sqrt{ln\,(1 + \frac{\nu}{d_m^2})} \quad and \quad \mu = ln\frac{d_m}{\sqrt{1 + \frac{\nu}{d_m^2}}} \tag{5.2}$$

where ν is the variance of DSDs and d_m is the mean of all bin sizes.

Figure 5.1 shows a droplet size distribution for four different number of bin fractions as 7, 15, 20, and 35 bin fractions for 5.0vol% of Conroe oil agitated at 400 rpm. A nearly identical distribution for 20 and 35 bin fractions can be observed. The similarity in the profiles of droplet size distribution for 20 and 35 bin fractions resulted in choosing 20 bin fractions for further simulation.

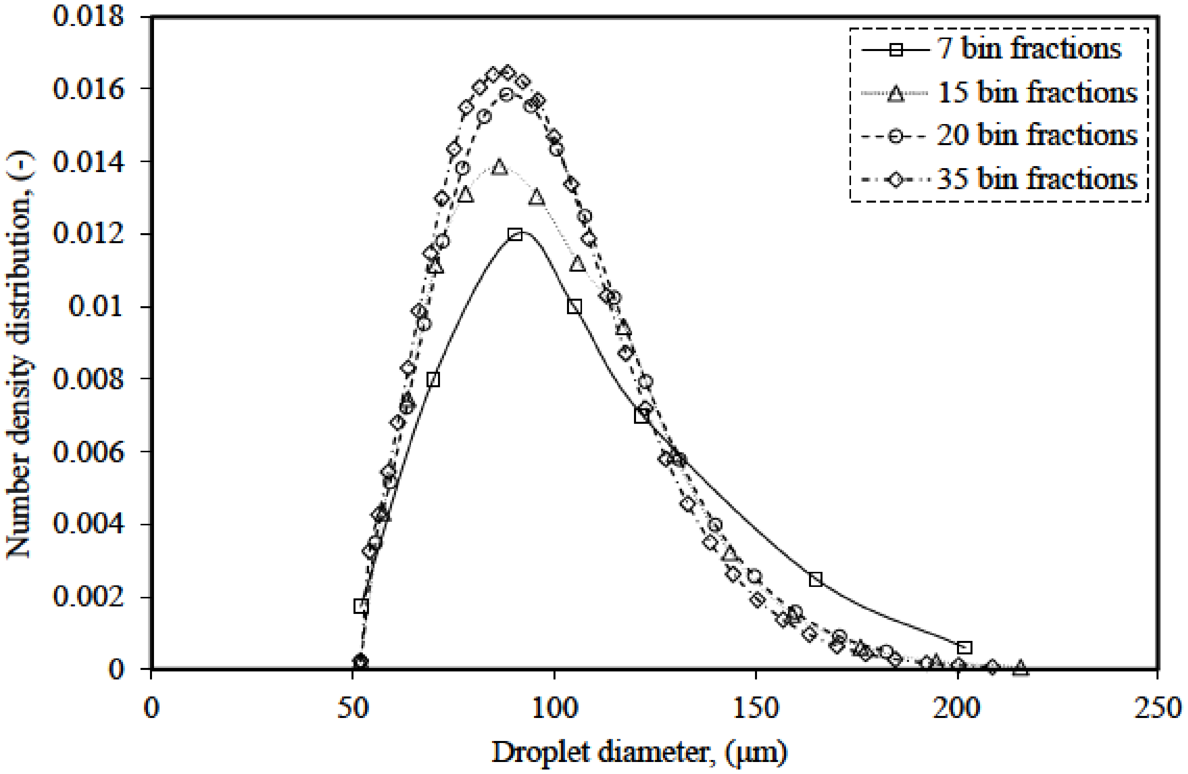

Figure 5.1. Droplet size distribution of 5% water in Conroe oil at 400 rpm for different number of classes.

Figure 5.2 shows the cumulative probability droplet size distribution of 15.0 vol% water in Conroe oil as a function of impeller speed. As the impeller speed increased, the size of the water droplets gradually shifted to the smaller droplets. As a result, the maximum droplet size of approximately 290 µm for 300 rpm were substituted by 210 and 135 µm at 400 and 600 rpm, respectively. This shows that the breakage phenomenon was more dominant at higher impeller speeds as expected. In fact, an increase in impeller speed results in higher turbulent pressure fluctuation. The turbulent kinetic energy provided by eddies with diameter of $\lambda \leq d$ break the mother droplet to the smaller droplets (Simon et al., 2003). An increased flow velocity gradient also increases the oscillations and the breakage probability of oil droplets (Stamatoudis and Tavalarides, 2007). Consequently, the fraction of oil droplets with small diameter is increased and the distributions are shifted to smaller sizes. The shift in droplet size distributions toward smaller size with higher agitation intensity was also noticed in other studies (Gerstlauer, 1999; Ramkrishna, 2000; Alopaeus et al., 2002).

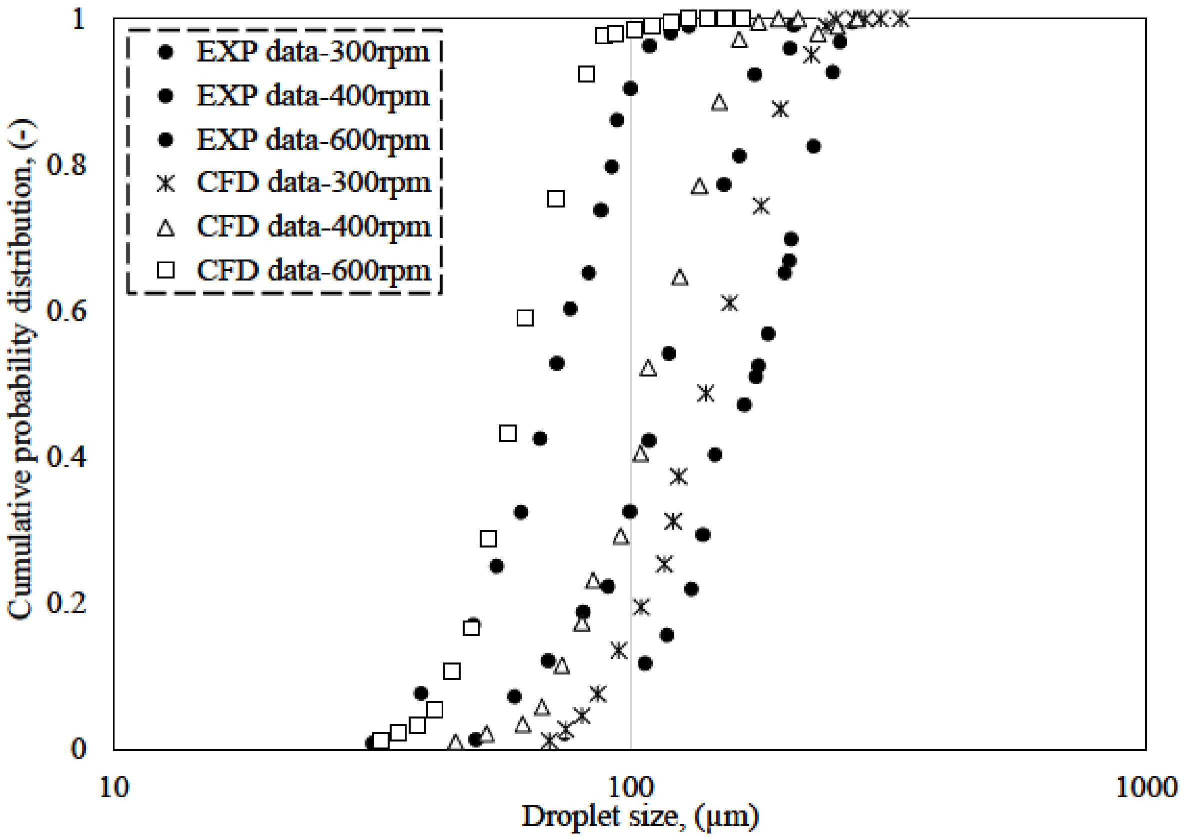

Figure 5.2. Cumulative probability size distribution for different impeller speeds for continuous phase of Conroe oil at 15% volume fraction.

Figure 5.3 presents the logarithm number density of seven bin fractions at different impeller speeds for 15.0% water volume fraction. Seven arbitrary bin fractions were chosen in a way to have two small size droplet classes, three medium size droplet classes, and two large size droplet classes. The comparison between the bin classes at 300 rpm and 400 rpm shows an increase in number densities for most of the bins due to turbulent intensity induced by higher impeller rotation (Ruiz et al., 2002; Ok et al., 2003; Schütz et al., 2009). Further analysis of logarithmic number densities for the middle-sized droplets (i.e. classes 3, 4, and 5) especially at 400 rpm and 600 rpm shows higher numbers in these classes which justify higher coalescence rate among small droplets. The higher coalescence rate was occurred due to increased characteristic velocity of collision between droplets as shown in Eq. (4.22). As the impeller speed increased to 600 rpm, a higher coalescence rate was induced by a higher adhesion energy and a higher collision rate among the middle size classes. A decrease in the size of droplets leads to an increase in cohesive stress and a decrease in disruptive stress, until droplet reaches a certain size, at which point the rate of breakage and coalescence will be the same (Rueger and Calabrese, 2013).

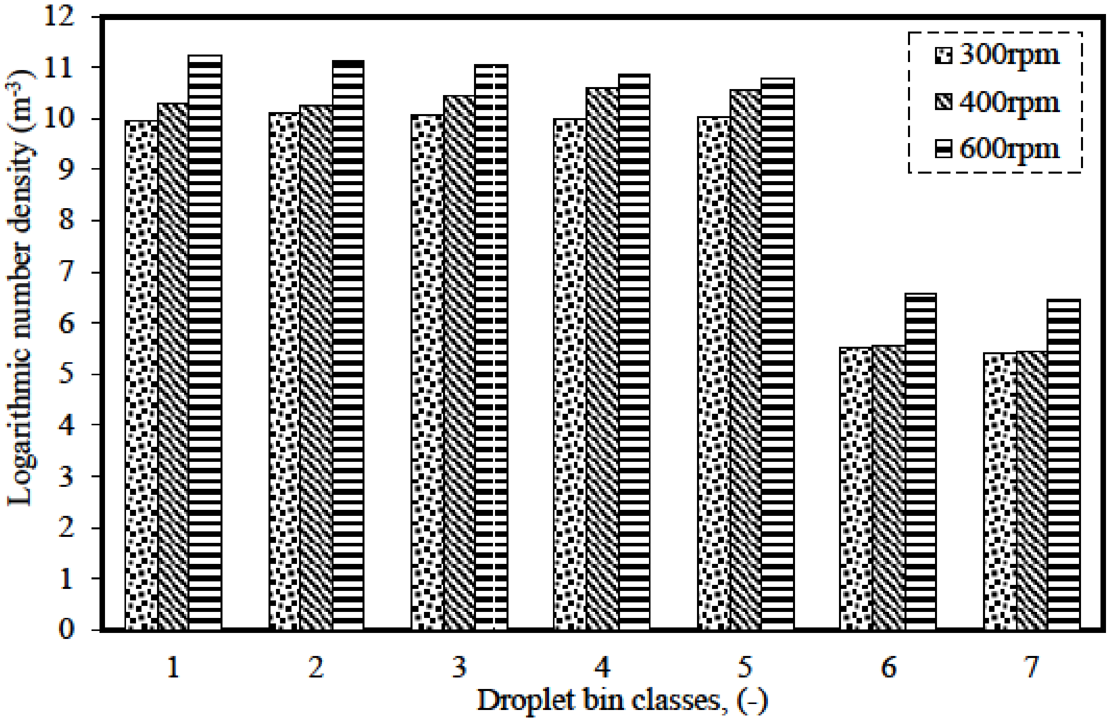

Figure 5.3. Logarithmic number density of droplets for 7 bin classes (small, medium, and large size droplets) in Conroe oil- water with volume fraction of 5.0%.

Figure 5.4 shows the vertical cross section contour plots for the 15.0% volume fraction of dispersed phase at different impeller speeds. This figure depicts a relative non-homogeneity in the vessel at the impeller speed of 300 rpm compared to 400 and 600 rpm. As can be seen in this figure, the water volume fraction is higher in the region beneath the impeller at 300 rpm. The higher density of water, and insufficient pumping power generated by the Rushton impeller at 300 rpm are the two factors leading to the higher volume fraction of water at the bottom of the tank. The insufficient flow motion was recovered by increasing the impeller speed to 400 rpm, therefore, the green region at the tank surface becomes smaller. As can be seen, still some degree of inhomogeneity can be observed at the bottom of the tank. With an increase in impeller speed to 600 rpm, a full homogenous flow was obtained due to higher turbulent kinetic energy and improved recirculation rate induced by impeller (Maggioris et al., 1998). Since the dispersed phase is located at the bottom of the tank before mixing, and the pumping rate of impeller is insufficient at 300 and 400 rpm; a lower impeller off-bottom clearance could also help in higher circulation rate and more homogenous flow within the tank at lower impeller speeds.

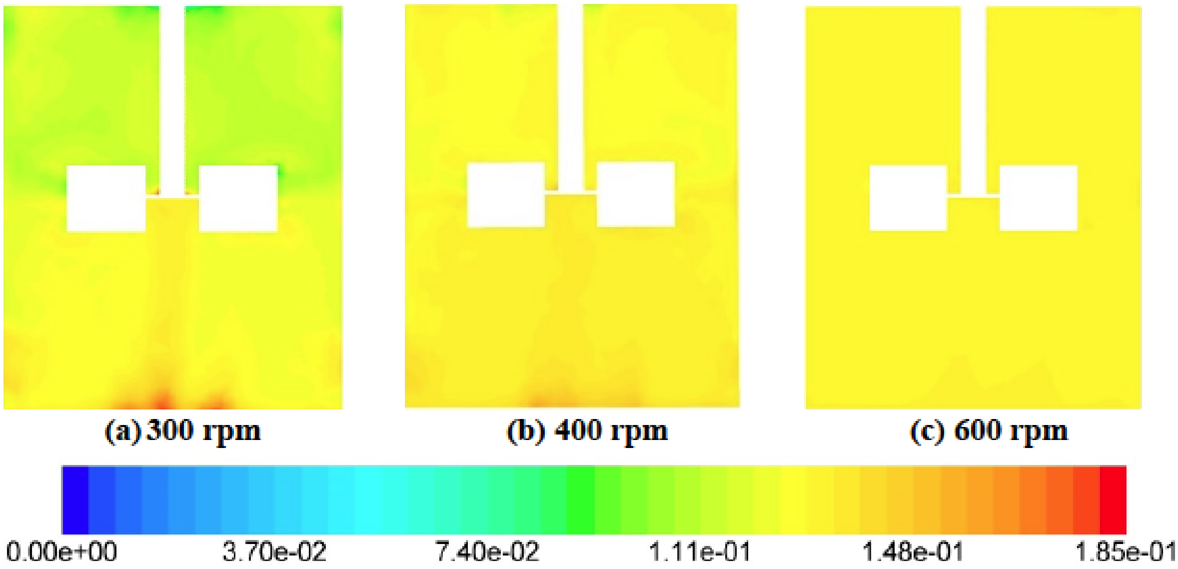

(a) 300 rpm **(b) 400 rpm** **(c) 600 rpm**

Figure 5.4. Contour of volume fractions for 15% volume fraction water in pure Conroe oil at impeller speed of **(a)** 300 rpm, **(b)** 400 rpm, and **(c)** 600 rpm.

Figure 5.5 shows the effect of dispersed phase volume fraction on DSD at 400 rpm impeller speed. Similar bell-shaped curves are observed at different volume fractions, however, dispersions with higher volume fraction show larger number densities which was expected. A slightly narrower size distribution profile can be observed as volume fraction decreased which agrees with a study by Liu et al. (2013). According to Liu et al. (2013), an increase in volume fraction of the dispersed phase (i.e. ranging from 1.0% to 5.0%) results in a wider droplet size distribution. Wang et al. (2013) obtained the same result for evolution of chord length distribution (CLD) at different oil volume fractions (10.0-60.0%) in a mixing tank. However, Qi et al. (2015) reported no pronounced effect of volume fraction on DSD for high concentrated emulsions. Boxall et al. (2010) also mentioned no pronounced difference in DSD of water-crude oil dispersion for volume fractions of 10.0%-35.0%.

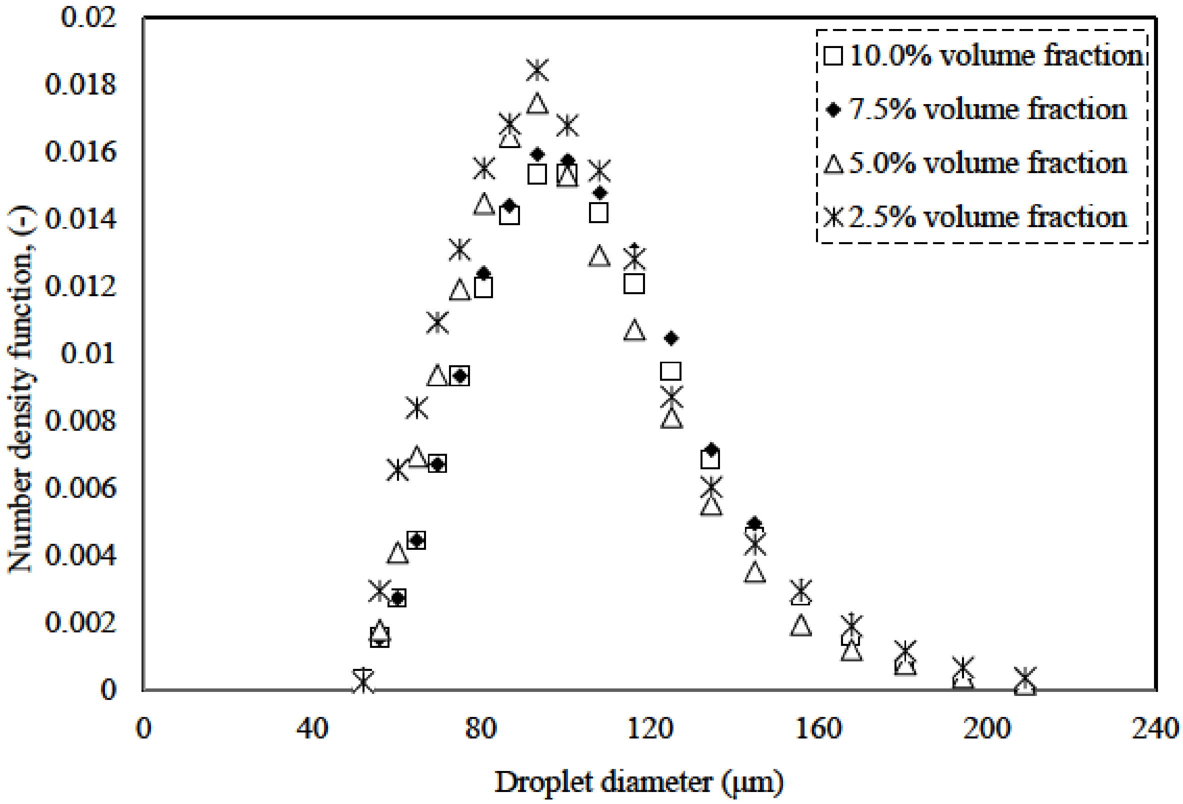

Figure 5.5. Droplet size distribution for different water volume fraction at 400 rpm with Conroe oil.

Figure 5.6 shows the contour of turbulent kinetic energy on five horizontal planes for Conroe oil at 15.0% volume fraction and impeller speed of 300 rpm. This figure shows that the turbulent kinetic energy was more intense at the center of plane 3 in compared with other horizontal planes, whereby less turbulent kinetic energy was induced by flow circulation at the center of other planes. The distribution of turbulent kinetic energy on plane 1 and plane 2 shows lower values of turbulent kinetic energy at the center while more energy is distributed near the walls. The average turbulent kinetic energy on planes are as follows: Plane 1: 0.0108 m^2s^{-2}, Plane 2: 0.0153 m^2s^{-2}, Plane 3: 0.0457 m^2s^{-2}, Plane 4: 0.0176 m^2s^{-2}, and Plane 5: 0.0125 m^2s^{-2}. The average turbulent kinetic energy shows higher values for the planes above the impeller. This result can be the evidence for lower droplet breakage below the impeller (Maggioris et al., 2000) which can be enhanced by decreasing the impeller off-bottom clearance.

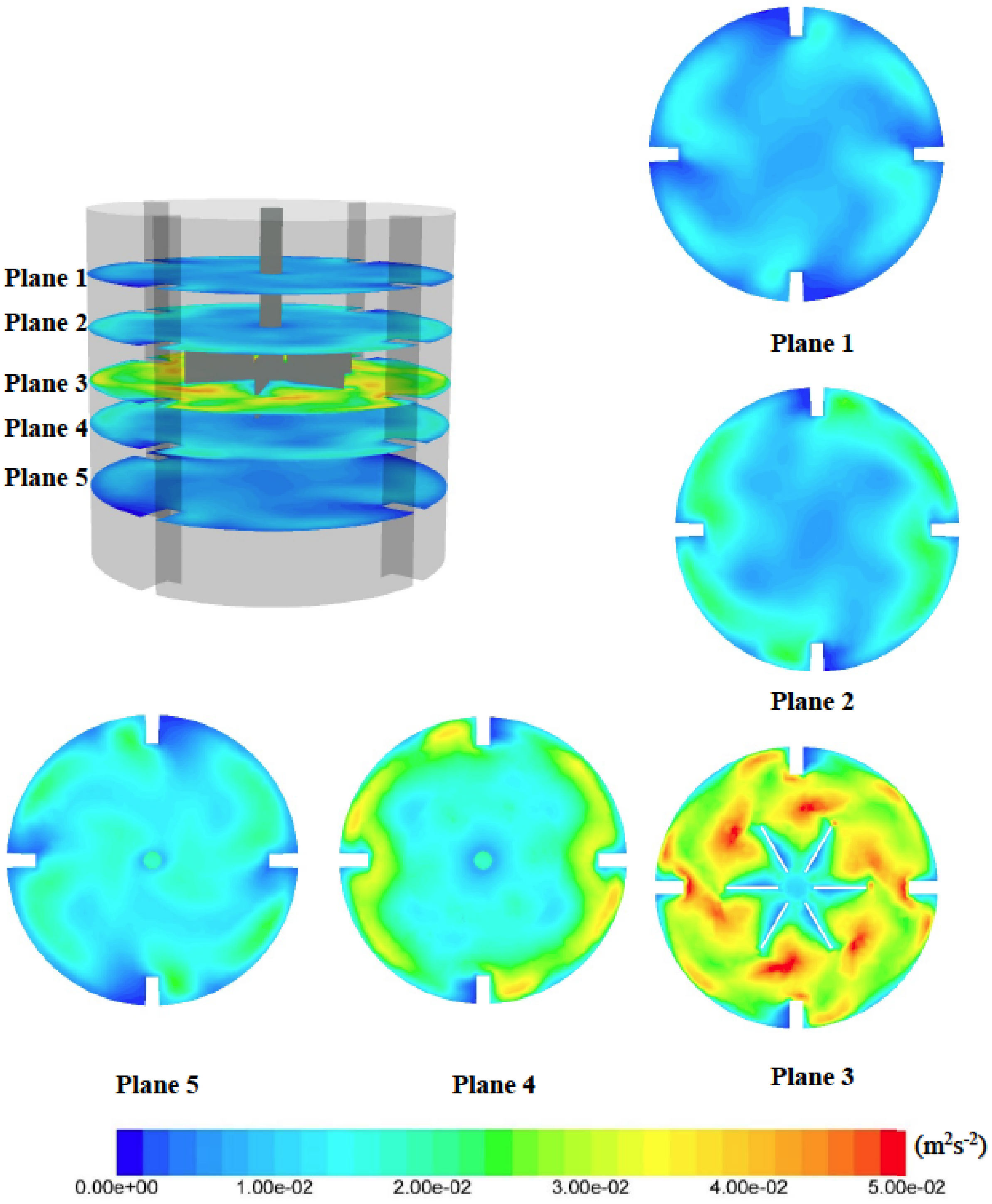

Figure 5.6. Contour of turbulent kinetic energy (m^2s^{-2}) at 300 rpm with 15% volume fraction.

The viscosity of continuous phase is another important factor as it affects the stability of the dispersion system and also droplets size (Boxall et al., 2010). **Figure 5.7** shows droplet size distribution for different crude oils at the impeller speed of 400 rpm and 5.0% water volume fraction. As mentioned in Table. 1, four different crude oils with viscosities ranging from 3.1

mPa.s to 262 mPa.s were considered as the continuous phase. Increased viscosity resulted in lower film drainage rate and lower coalescence rate between liquid droplets in high-viscous fluids (Roudsari et al., 2012), thus, the distributions were shifted toward smaller sizes, and narrower size distributions were achieved. As can be seen, the smaller and narrower size distribution was obtained for Petronius oil with lower viscosity compared to the Conroe-Brightstock oil. This is due to the lower interfacial tension between water and Petronius oil. Lower interfacial tension resulted in a reduction in the retaining force of a droplet, a higher breakage rate, and a smaller droplet size in Petronius oil.

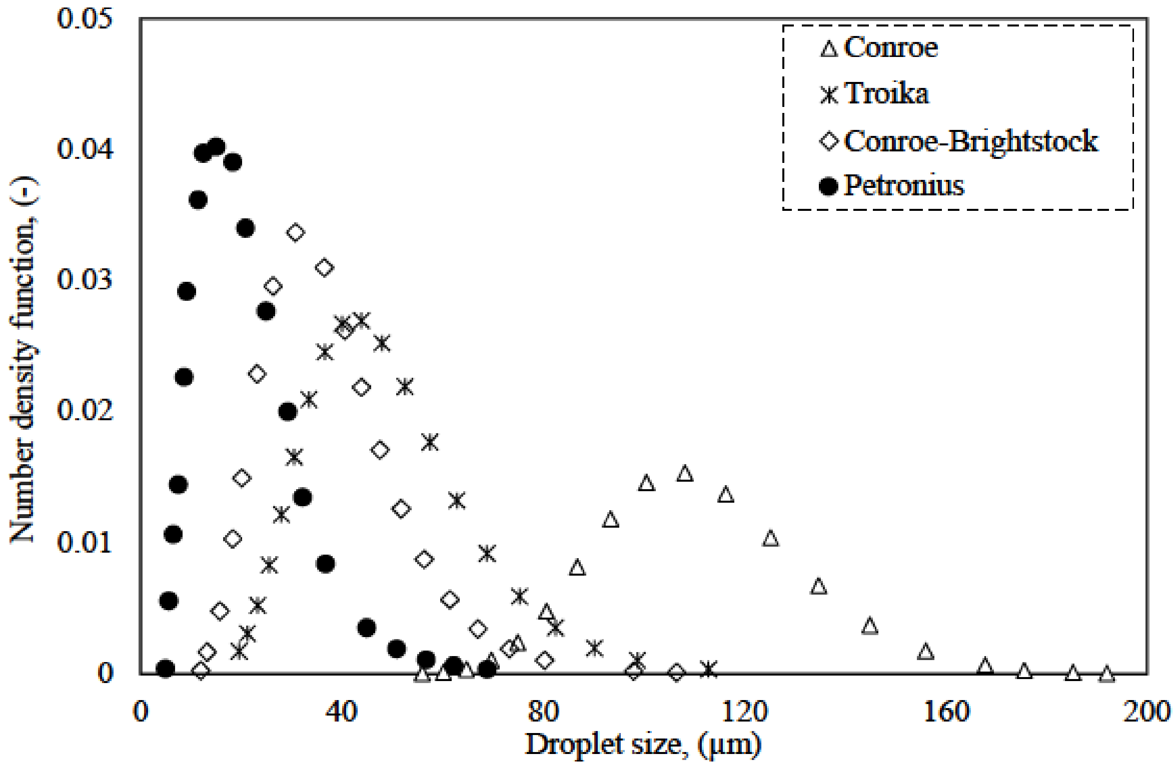

Figure 5.7. Droplet size distribution for different crude oils at impeller speed of 400 rpm and 5% volume fraction.

The evolution of droplet size distribution is influenced by the dynamic breakage and coalescence happening in the process until the steady state condition is reached. **Figure 5.8(a)** shows the contour of breakage source term for 10.0% water volume fraction dispersed in Conroe oil at 300 rpm impeller speed. The birth/death source term due to breakage and coalescence are presented in Eq. (4.12)- (4.13) and Eq. (4.19)- (4.20), respectively. As can be seen, the breakage source term within the tank is negligible compared to the region around the impeller edges with high turbulent dissipation rate, and on the adjacent wall. Although the size of this region is small, high velocity magnitude of the flow induced by impeller in this region

(**Figure 5.8(d)**) results in a high pumping rate through the tank which has considerable impact on droplet size. A successful coalescence between droplets depends on collision efficiency and collision frequency. The contour of coalescence source term at the same operational condition is presented in **Figure 5.8(b)**. As shown in this figure, the coalescence happens everywhere in the vessel. According to the study by Vonka and Soos (2015), higher turbulence in impeller region leads to lower coalescence rate for droplets since there is not enough time for droplets to coalesce. The coalescence source term is nonzero within the tank, although its value is smaller than the value of breakage source term. By comparing the rate of breakage and coalescence source terms, we can conclude that the droplet size distribution is mainly controlled by the breakage. **Figure 5.8(c)** shows the contour of Sauter mean diameter at 10.0% water volume fraction agitated at 300 rpm in Conroe oil which was obtained by using Eq. (5.3) through discrete method in PBM as follows (Khakpay and Abolghasemi, 2010):

$$d_{32} = \frac{\sum_{i=1}^{n} n_i d_i^3}{\sum_{i=1}^{n} n_i d_i^2} \tag{5.3}$$

where n_i and d_i are the number and diameter of droplet in DSD, respectively. A relatively homogenous profile of Sauter mean diameter can be observed due to good mixing in the tank and strong velocity profile as shown in **Figure 5.8(d)**. **Figure 5.8(d)** shows the velocity vector of the primary phase. It can be noticed that two symmetrical liquid vortices were formed in the upper and lower region of the impeller as expected for the radial-flow Rushton impeller. A strong radial flow generated around the impeller results in strong flow circulation rate in breakage region.

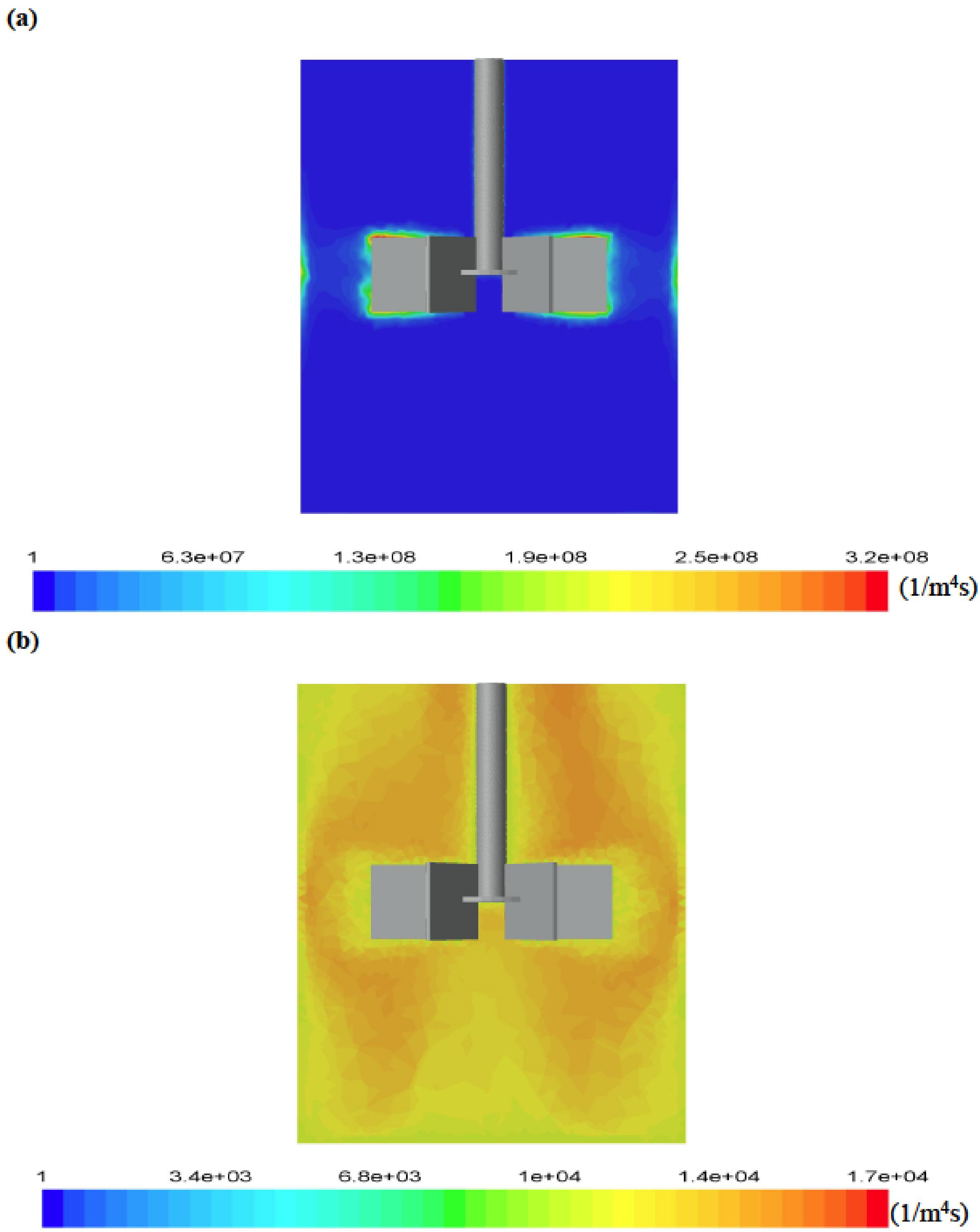
(a)
1
6.3e+07
1.3e+08
1.9e+08
2.5e+08
3.2e+08
(1/m⁴s)
(b)
1
3.4e+03
6.8e+03
1e+04
1.4e+04
1.7e+04
(1/m⁴s)

Figure 5.8 (continued).

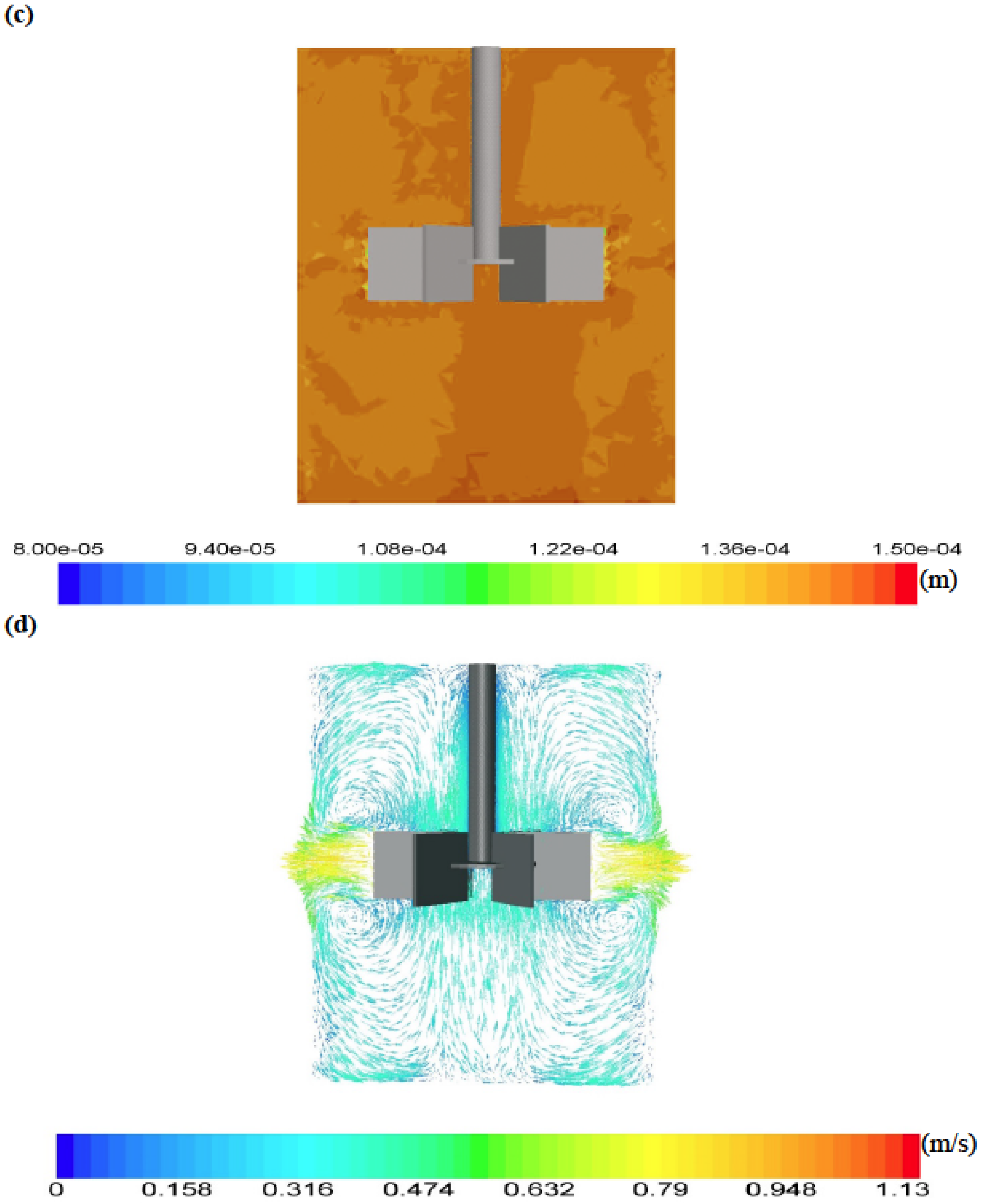

Figure 5.8. Contour plots of: **(a)** breakage source term, **(b)** coalescence source term, **(c)** Sauter mean diameter, and **(d)** velocity vector of continuous phase for Conroe oil at 10.0% volume fraction and impeller speed of 400 rpm.

According to Kolmogorov's theory (1949), two different turbulent regimes were defined; "turbulent inertial" and "turbulent viscous" regimes. To determine the mechanism of energy dissipation contributing to droplet break-up, Kolmogorov (1949) defined an eddy length scale (λ). Based on Eq. (5.4), droplets with the diameter larger than the eddy length scale fall into turbulent inertial regime where the interfacial stresses are balanced by inertial stresses and viscous forces can be neglected. In the turbulent inertial regime, the maximum droplet size (d_{max}) is determined by the balance between turbulent fluctuations against the droplet capillary pressure. However, in the turbulent viscous regime the droplet diameter is smaller than the eddy length scale and d_{max} is determined by the balance between the viscous forces against the droplet capillary pressure (Vankova et al., 2007). Shinnar (1961) concluded that turbulent inertial regime is the dominant mechanism for droplet breakup in turbulent dispersions in stirred tank.

$$\lambda = (\frac{\nu^3}{\varepsilon})^{1/4} \tag{5.4}$$

where λ is the Kolmogorov eddy length scale, ν is the kinematic viscosity, and ε is the local energy dissipation rate. To distinguish the regime proposed by Kolmogorov (Kolmogorov, 1949), the size of smallest eddies should be determined. The change in the regime depends not only on the size of the smallest eddies, but also on the viscosity of continuous phase and the maximum stable droplet size (d_{max}) in dispersion (Vankova et al., 2007). Among various correlations for d_{max}, an equation by Davies (1985) can describe the maximum stable drop size, in turbulent inertial regime, for the viscosity range of 3 and 100 mPa.s which is applicable to our study:

$$d_{max,D} = 0.86\left(1 + 0.37\frac{\mu_D \varepsilon^{1/3} d_{max,D}^{1/3}}{\sigma}\right)^{3/5} \sigma^{3/5} \rho_C^{-3/5} \varepsilon^{-2/5} \tag{5.5}$$

where $d_{max,D}$ is the maximum stable droplet size in inertial regime according to the study by Davies (1985) and μ_D is the viscosity of dispersed phase. **Figure 5.9** presents the comparison between experimental data (Boxall et al., 2010) and calculated values (from Eq. (5.5)) for the maximum stable droplet size for different viscosities and different impeller speeds at volume fraction of 15.0%. The rate of energy dissipation rate for calculation of maximum droplet size was obtained by CFD model after the steady state condition was reached. As can be seen in this figure, although the calculated data for Conroe oil and Troika oil are well correlated by

Davies equation; a significant discrepancy between the experimental data and the theoretical data for viscous oils, Conroe-Brightstock and Petronius, was observed. The maximum droplet size decreased significantly as the viscosity of continuous phase changed from 20 mPa.s to 100 mPa.s. Therefore, Eq. (5.5) cannot predict the maximum stable droplet size at higher viscosity of the continuous phase ($\eta_c > 20$ mPa. s). This is a good indication of a change in turbulent liquid-liquid dispersion regime.

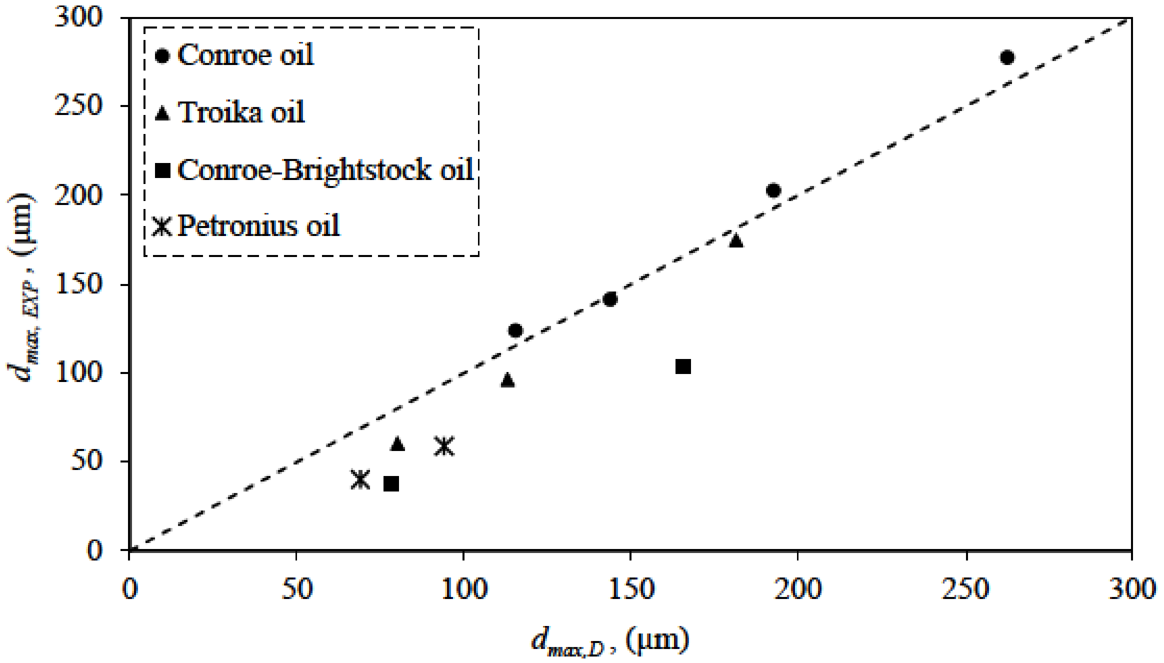

Figure 5.9. Comparison of experimental data (Boxall et al., 2010) and calculated values (using Eq. (5.5) and CFD inputs) for maximum stable droplet size ($d_{max,\ D}$) for various continuous phase viscosities and impeller speeds at 15.0% volume fraction.

According to Kolmogorov theory (Kolmogorov, 1949), as the viscosity of continuous phase increased, the size of the smallest turbulent eddies decreased. Consequently, droplets could become smaller than λ and the regime would change to viscous turbulent regime. The maximum stable droplet size in viscous regime can be obtained by following equation (Kolmogorov, 1949):

$$d_{max,viscous} = 4\varepsilon^{-1/2}\mu_c^{-1/2}\rho_c^{-1/2}\sigma \tag{5.6}$$

where $d_{max,Viscous}$ is the maximum stable droplet size in turbulent viscous regime, μ_c is the viscosity of continuous phase, and ρ_c is the density of continuous phase. **Table 5.2** shows a comparison between the calculated values by Eq. (5.6) and experimental data obtained by

Boxall et al. (2010). As can be noticed in this table, the maximum droplet sizes are less than eddy length scales (calculated using Eq. (5.4)) indicating the viscous regime in dispersions based on Kolmogorov's theory. As can be seen in the table, the calculated values of maximum drop size using the values of ε by CFD model agree well with corresponding experimental data with the error less than 20.0%. The discrepancy in values of theoretical and experimental maximum drop size is related to imprecision to calculate the rate of ε, insufficient time to reach the steady state condition in experiments, and the theoretical constant in Eq. (5.6).

Table 5.2. Comparison of experimental data (Boxall et al., 2010) and calculated values (using Eq. (5.6) and CFD inputs) for maximum stable droplet size ($d_{max,\ viscous}$) for various continuous phase viscosities and impeller speeds at 15.0% volume fraction in turbulent viscous regime.

η_c (mPa.s)	Impeller Speed (rpm)	d_{max}, Experimental *(Boxall et at. 2010)* (µm)	$d_{max,\ viscous}$, calculated using Eq. (5.6) (µm)	λ (µm)
100	300	58.8	64.1	78.7
100	400	39.8	44.6	76.2
262	300	103.9	92.5	118.6
262	600	38	33.4	62.3

The results of **Figure 5.9** and **Table 5.2** show that the maximum droplet size is under control by different parameters depending on the type of turbulent regime. The identification of regimes is of interest for the researchers since much smaller droplets can be obtained in the viscous regime in compared to the inertial regime at the equivalent condition. One can identify the regime by investigation the effect of continuous phase viscosity on maximum droplet size. If the variations in droplet size are not significant (e.g. up to 2-3 times), then the turbulent regime falls in turbulent inertial (Davies, 1985). However, the change in the viscosity of continuous phase results in considerable decrease of droplet size with d_{max}, this is a good indication of turbulent viscous regime. A closer look at Eq. (5.6) reveals that viscosity of continuous phase is the most efficient factor in changing the regime due to its significant effect on eddy length size and maximum stable droplet size in viscous regime. However, viscosity of continuous phase has no effect on the maximum stable droplet size in inertial regime (Davies, 1985) as presented in Eq. (5.5).

The first studies on liquid-liquid dispersion were limited to stirred tanks with low viscosity continuous phase or dilute emulsions (Rueger and Calabrese, 2013); however, industrial processes take advantage of different liquid-liquid dispersion system with a wide range of viscosity. Various models and theories have been established to correlate the mean and maximum droplet sizes to dimensionless parameters such as Weber number and Reynolds number. An appropriate mechanistic correlation between the size of droplets and dimensionless hydrodynamic parameters such as Weber number needs to be determined based on the droplet size relative to the Kolmogorov eddy length scale (Kolmogorov, 1949). Many authors such as Rueger and Calabrese (2013), El-Hamouz et al., (2009), and Pacek et al., (1999) obtained a correlation between the maximum stable droplet size and the Weber number in turbulent inertial regime as follows:

$$\frac{d_{max}}{D} \propto \varepsilon_T^{-0.4} \propto We^{-0.6} \tag{5.7}$$

where d_{max} is maximum stable droplet size, D is impeller diameter, ε_T is mean energy dissipation rate per unit mass, and *We* is Weber number. The Weber number in stirred tanks is defined as follows:

$$We = \frac{\rho_c N^2 D^3}{\sigma} \tag{5.8}$$

where ρ_c is the density of continuous phase, N is the impeller speed, D is the impeller diameter, and σ is the surface tension.

Figure 5.10(a) shows the correlation for maximum droplet size and Weber number in turbulent inertial regime for Conroe oil and Troika oil at 15.0% volume fraction and different impeller speeds. The theoretical maximum droplet sizes are well correlated with Eq. (5.7) with regression value over 98%. This agrees with the data reported by El-Hamouz et al. (2009) for silicon oil with addition of surfactant; however, the correlation for our results has higher exponent (-0.67) which is attributed to higher coalescence rate of droplets without using surfactant in our system. Our findings show that dispersions with higher volume fractions have higher value of exponent compared to the value of -0.6. On the other hand, Shinnar (1961) presented a correlation for turbulent viscous regime as follows:

$$\frac{d_{max}}{D} \propto (We\,Re)^{-1/3} \tag{5.9}$$

where d_{max} is the maximum droplet size in dispersion, D is impeller diameter, *We* and *Re* are the Weber number and Reynolds number, respectively. As shown in **Figure 5.10(b)**, the d_{max}

of Conroe-Brightstock and Petronius oils with 15.0% water volume fraction at different impeller speeds vary inversely with almost cube root of the $(We\ Re)$, which is in good agreement with the literature (Shinnar, 1961). Rueger and Calabrese (2013) mentioned that in dispersion when the eddy length scale is greater than the droplet size, but not by orders of magnitude, the inertial stress can be ignored. This correlation provides satisfactory results for viscous oils in turbulent viscous regime with regression value over 99%.

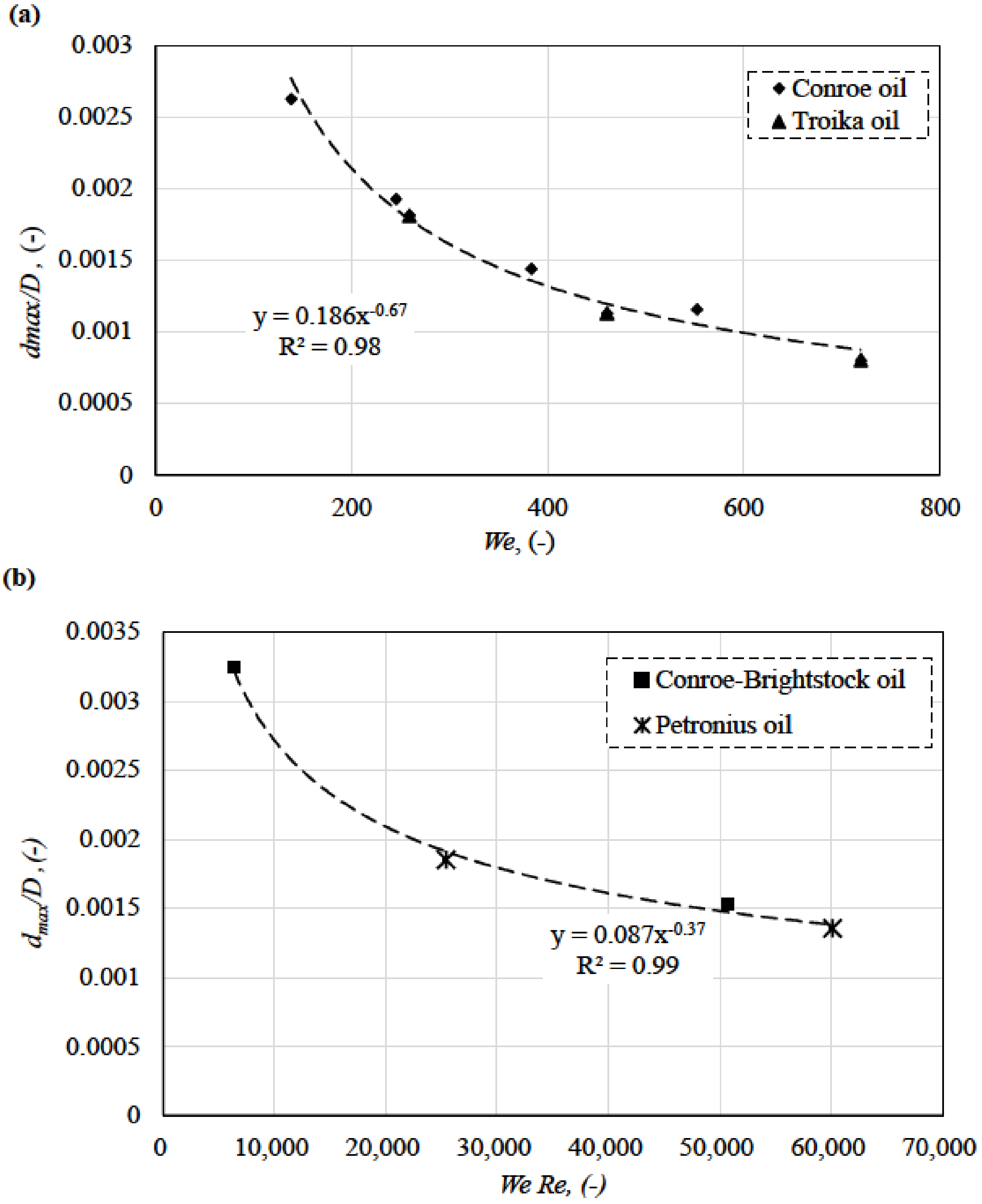

Figure 5.10. Correlation of d_{max} with: **(a)** *We* in turbulent inertial regime, and **(b)** *We.Re* in turbulent viscous regime, at different impeller speeds and 15.0% water volume fractions.

5.4 Concluding Remarks

Computational fluid dynamics (CFD) in conjunction with the population balance modeling (PBM) were employed to study water-in-crude oil dispersions in a stirred tank equipped with a Rushton turbine. The Eulerian-Eulerian multiphase approach, k-ε turbulent model, and MRF technique, were implemented in the model. The PBM provided satisfactory results with the use of Lehr's breakage model in liquid-liquid dispersion in the vessel. The effect of agitation speed, the volume fraction of dispersed phase, and the viscosity of primary phase were investigated.

- An increased turbulent energy dissipation rate, generated at higher impeller speeds, leads to droplets of smaller size and narrower size distribution. Higher impeller speed results in predominant breakage in the system and a shift in droplet size distribution (DSD) towards smaller droplets.
- The effect of volume fraction on DSD was found to be negligible while wider distributions were obtained at higher volume fractions.
- Additionally, an increase in the viscosity of the primary phase, as well as a decrease in the interfacial tension, lead to smaller droplet size and narrower droplet size distribution. The results showed that the dispersion could be performed in two different regimes, i.e. turbulent inertial and turbulent viscous regimes.

The maximum droplet diameter depends slightly on volume fraction and the viscosity of continuous phase in turbulent inertial regime. Transition from inertial to turbulent viscous regime was accomplished with an increase in continuous phase viscosity and smaller droplets were obtained in turbulent viscous regime. The theoretical droplet size was calculated by Davies expression using the values of energy dissipation rate from CFD model, and then were compared by experimental data in inertial regime. The maximum droplet size in turbulent viscous regime was successfully correlated with the product of Weber number and Reynolds number.

Experimental and Numerical Investigation on Mixing of Dilute Liquid-liquid Dispersion in a Stirred Tank

6.1 Abstract

The present study provides experimental and simulation data on hydrodynamic characteristics and chord length distribution (CLD) of dilute liquid-liquid dispersion in an un-baffled stirred tank. The electrical resistance tomography (ERT) coupled with focused beam reflectance measurement (FBRM) instrument was effectively applied for imaging liquid-liquid flow and measuring droplet size inside the tank, respectively. The effect of agitation speed, volume fraction, and viscosity of the oil-phase were investigated. A novel shape analysis in 2D and 3D was also assessed based on CLDs of dispersion. The correlations between Sauter mean diameter and hydrodynamic parameters of the system have been investigated. An Eulerian multiphase model and standard K-epsilon turbulence model incorporating with population balance discrete method were employed to simulate the flow field and droplet size distribution in a stirred tank. This chapter is organized as follows:

6.2. Introduction
6.3. Results and Discussion; and
6.4. Concluding Remarks.

6.2 Introduction

The mixing tank modeled in this study is a flat-bottom cylindrical tank with the internal diameter of 0.2 m and the liquid height in the tank is 0.2 m. A PBT impeller with a diameter of 0.1 m was attached to a central shaft with an off-bottom clearance of 0.095 m. The tank was filled with water as the primary phase and two different oils, canola oil and linseed oil, as the dispersed phase. The physical properties of the fluids are presented in **Table 3.1**. The experimental condition is tabulated in **Table 3.2**.

6.3 Results and Discussion

Figure 6.1 shows the droplet counts with time for canola oil at 10% volume fraction and impeller speed of 250 rpm. At the beginning of the agitation, the counts of droplets with chord length <10 μm increased rapidly due to the generated turbulent eddies in the continuous phase. An increase in the number of large size droplets (300-1000μm) was also observed which is related to the presence of oil stream around the impeller region at the beginning of mixing.

After a short time, large oil droplets broke up to smaller droplets in the formed eddies by viscous forces in the continuous phase which leads to a gradual increase in the count of droplets with the size of 10-300 µm. The collision between small droplets also results in decrease in the counts of small droplets (<10 µm) and increase in the counts of medium-sized droplets. After sufficient time, a balance between dynamic breakage and coalescence rate achieved and steady CLD is resulted. Heath et al. (2002) claimed that the possible reason for the difference in the count of different size ranges is because of the dependency of the chord length measurements on focal position of the FBRM pro be especially for larger droplets (300-1000 µm).

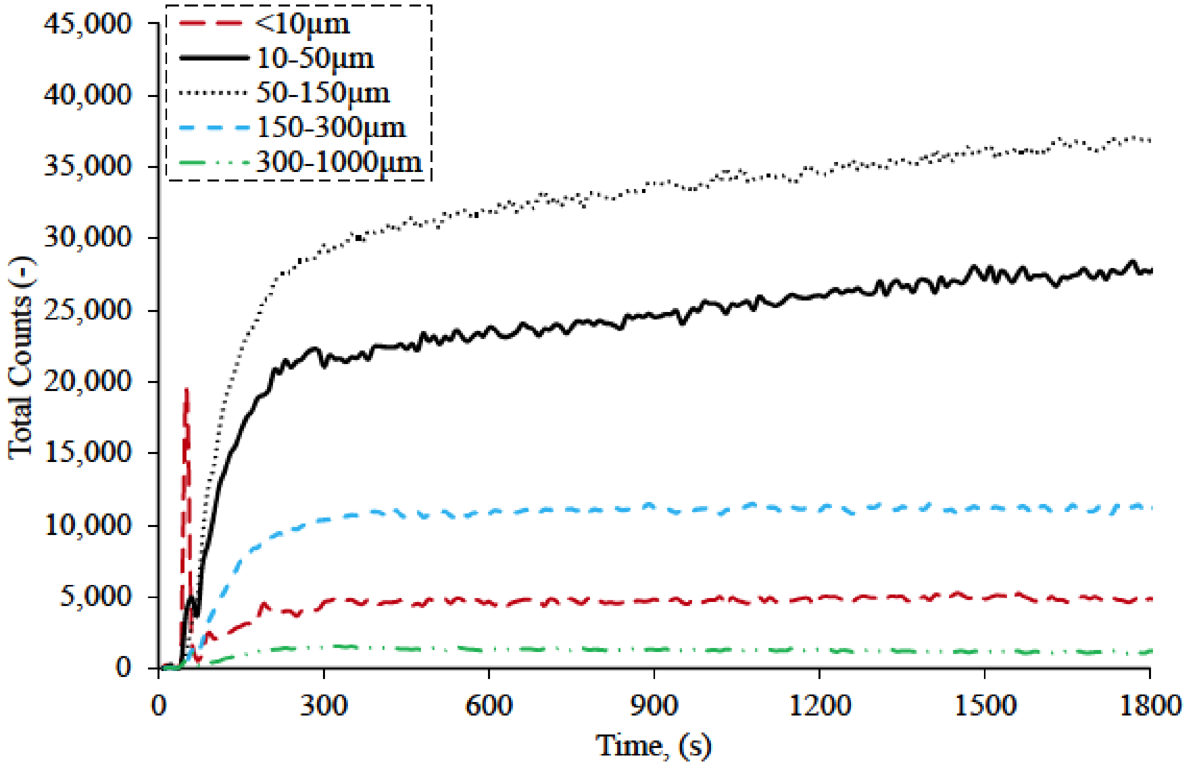

Figure 6.1. Droplet counts versus time for canola oil at 10.0% volume fraction and impeller speed of 250 rpm.

Figure 6.2 shows the flow pattern in the tank induced by impeller. The velocity vector of primary phase was colored by velocity magnitude. As can be seen in this figure, PBT impeller generates strong axial and radial flow around the impeller where droplet interactions are most likely to happen. A relatively higher velocity magnitude can be observed above the impeller in compare to the bottom of the tank. This figure also shows that the flow is being swept in a clockwise direction.

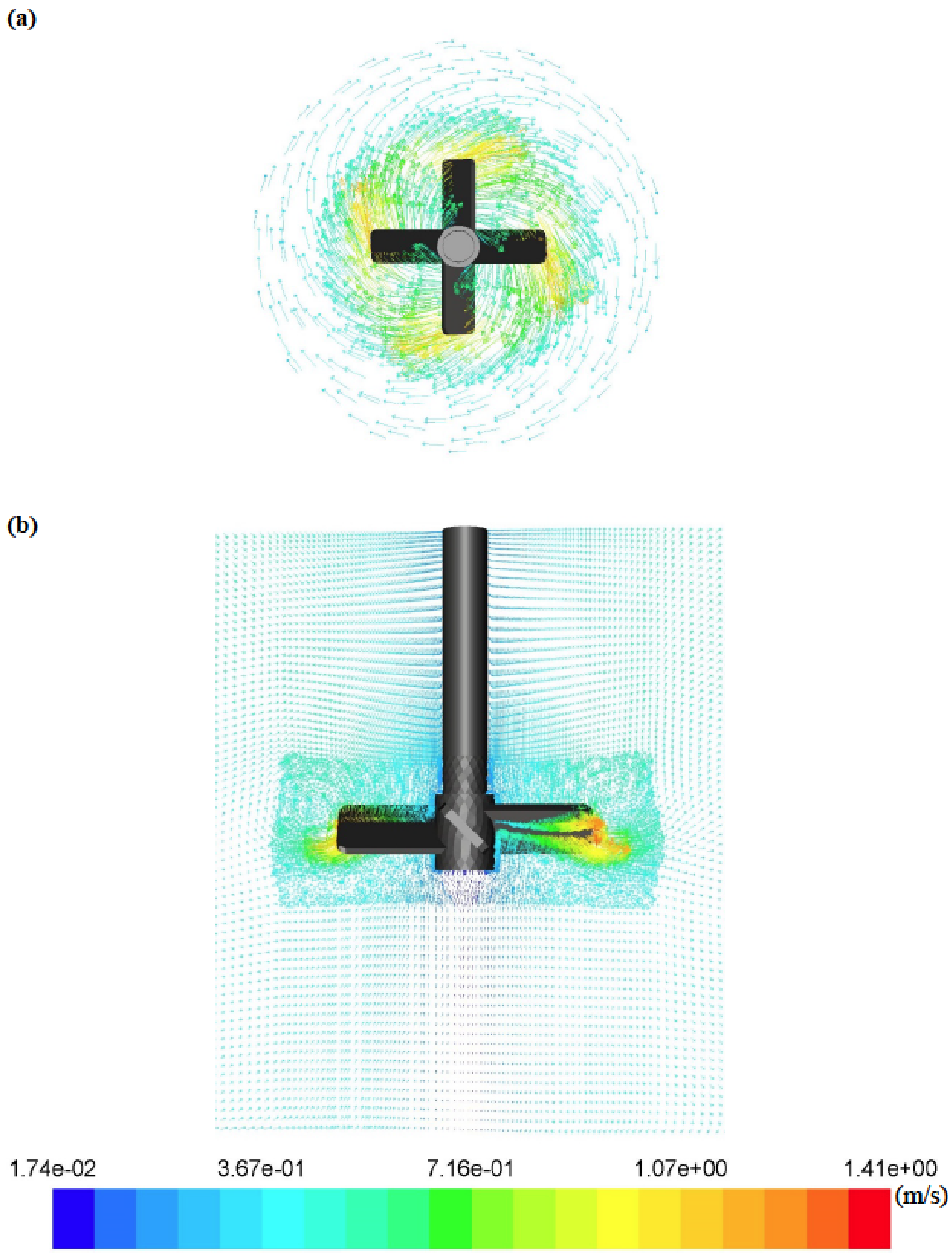

Figure 6.2. Velocity (m/s) vector of canola oil at 200rpm and 10% volume fraction on **(a)** Cross section area at h=0.095 m, **(b)** Vertical plane at x=0, -0.1<y, z<0.1 m.

The overall mixing index versus impeller speed for different volume fractions of canola oil and linseed oil is shown in **Figure 6.3**. This figure shows that mixing index decreased as the impeller speed increased regardless of oil's type and volume fraction. However, at the constant impeller speed, a better mixing performance with a lower mixing index was achieved at the lower volume fractions for both canola and linseed oils. Since the viscosities of the oils (i.e. dispersed phase) are higher than water's (i.e. continuous phase), as the oil volume fraction decreases, the mixture viscosity decreases (Nagata, 1975). A higher volume fraction of dispersed phase resulted in an increase in drag force between the phases and therefore less turbulence in the tank is achieved (Zhao et al., 2011).

The effect of volume fractions on the CLD of canola oil and linseed oil at the constant agitation speed of 200 rpm is shown in **Figure 6.4**. However, a same trend with an insignificant change in droplet size is noticed for all oil volume fractions, a slightly narrower distribution is observed at lower volume fractions. The width of the distribution (*span*) at different oil volume fractions can be defined by following equation (El-Hamouz et al., 2009):

$$span=\frac{d_{0.9}-d_{0.1}}{d_{0.5}} \tag{6.1}$$

where $d_{0.9}$ and $d_{0.1}$ are volume-averaged sizes at 90% and 10% percentile, respectively and $d_{0.5}$ is the median. The values for $d_{0.9}$, $d_{0.1}$, and $d_{0.5}$ are obtained from FBRM statistics output. **Table 6.1** shows the span of distributions at different volume fractions for impeller speed of 200 rpm.

Table 6.1. Span values at different volume fraction for canola oil and linseed oil at 200rpm.

Oil type	Volume Fraction			
	2.5%	**5.0%**	**7.5%**	**10.0%**
Canola oil	1.77	1.81	1.85	1.88
Linseed oil	1.64	1.76	1.79	1.81

It is evident that as volume fraction decreased the span was also decreased. Although Wang et al. (2013) reported narrower CLD at different oil volume fractions (10-60%) in a mixing tank, Boxall et al. (2010) and Qi et al. (2015) reported no pronounced effect of volume fraction on DSD for high concentrated emulsions.

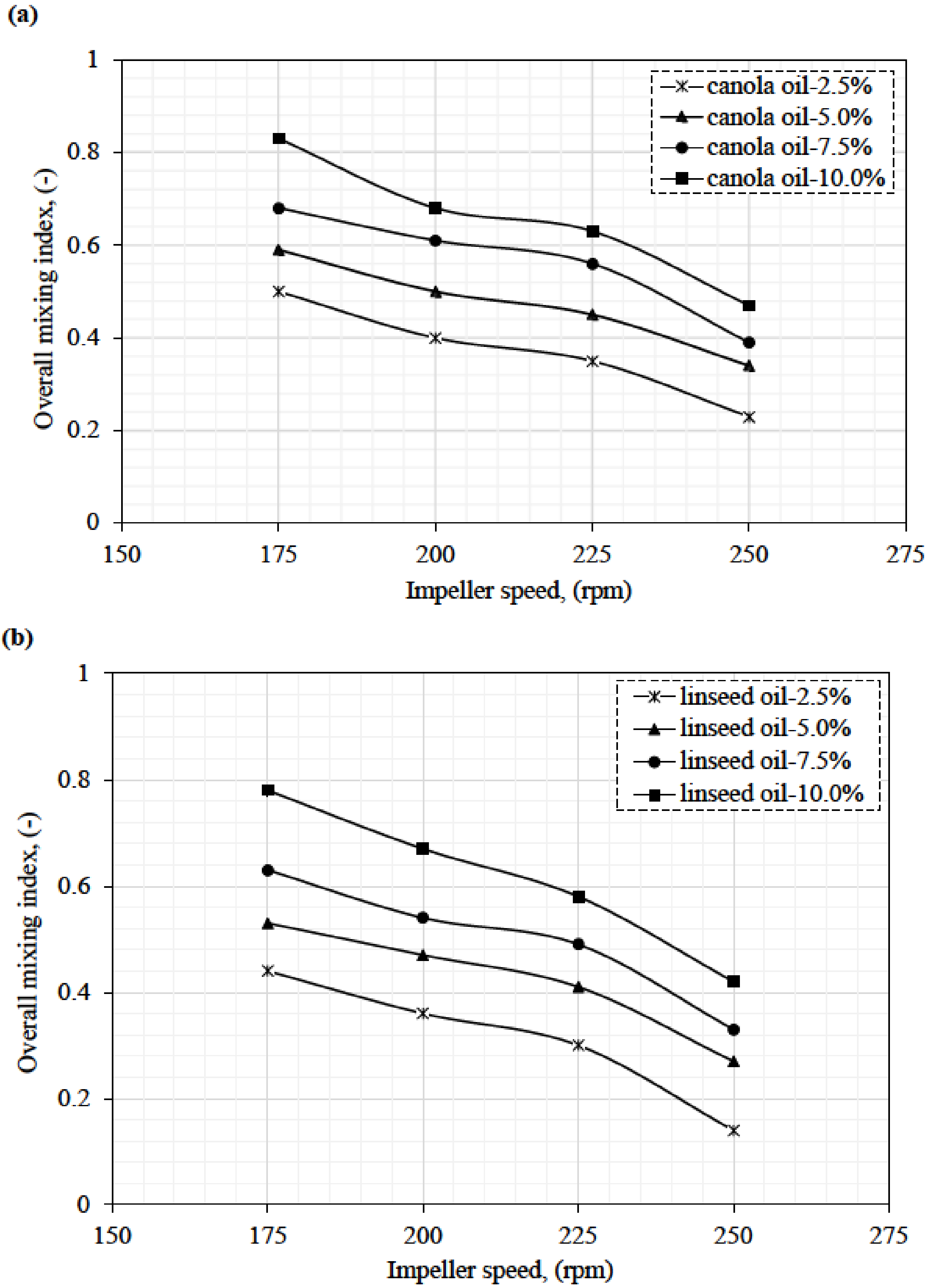

Figure 6.3. Overall mixing index (*MIo*) for: **(a)** Canola oil, and **(b)** Linseed oil at different volume fractions for different impeller speeds.

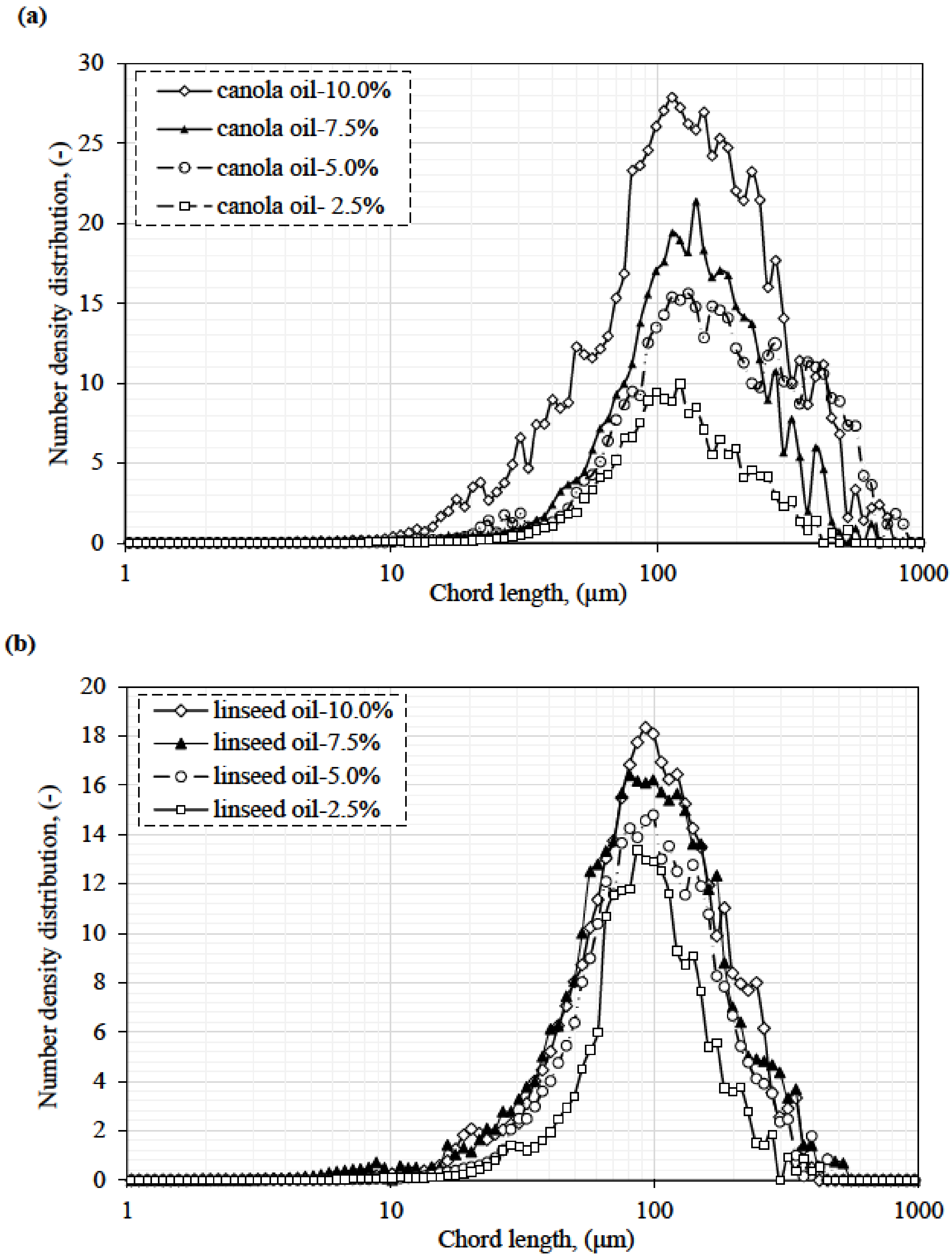

Figure 6.4. Chord length distribution (CLD) for **(a)** Canola oil, and **(b)** Linseed oil at impeller speed of 200 rpm for different volume fractions.

Figure 6.5 shows the normalized cumulative probability size distribution obtained from CFD and FBRM at different impeller speeds for canola oil and linseed oil at 10% volume fraction. The CFD results for this distribution agreed well with the experimental data with the maximum RMS error of 5.9%. The deviation of CFD results from experiments can be associated with the fact that FBRM oversize the small particles and undersize larger ones (Heath et al., 2002). As it was shown in Equation (12), the turbulent energy dissipation rate is an important factor in Lehr's breakage model. The significant variations in the turbulent properties of flow at different locations inside the tank cause a considerable variation in the local energy dissipation rate (Solsvik and Jakobsen, 2015). Therefore, the deviation of results may relate to the value of local energy dissipation rate. Another reason can be related to the assumption of having only spherical droplets in CFD simulations. It will be discussed that the shape of droplets has an effect on CLD.

As can be seen in **Figure 6.5**, an increase in impeller speed leads to an increase in the flow velocity gradient which improves the breakage probability of oil droplets. An increase in agitation speed also increases the turbulent pressure fluctuations, therefore, the generated turbulent eddies can provide enough energy for droplets to break up (Stamtoudis and Tavalarides, 2007). Consequently, the fraction of oil droplets with the small diameter is increased and the distributions are shifted to smaller sizes. The mean size of droplets changed from 75.16 μm at 175 rpm to 71.6 μm at 200 rpm, to 66.28 μm at 225 rpm, and finally to 60.84 μm at 250 rpm for canola oil. The shift in droplet size distributions due to increased agitation speed was also noticed by Alopaeus et al., (2002) and Boxall et al. (2010).

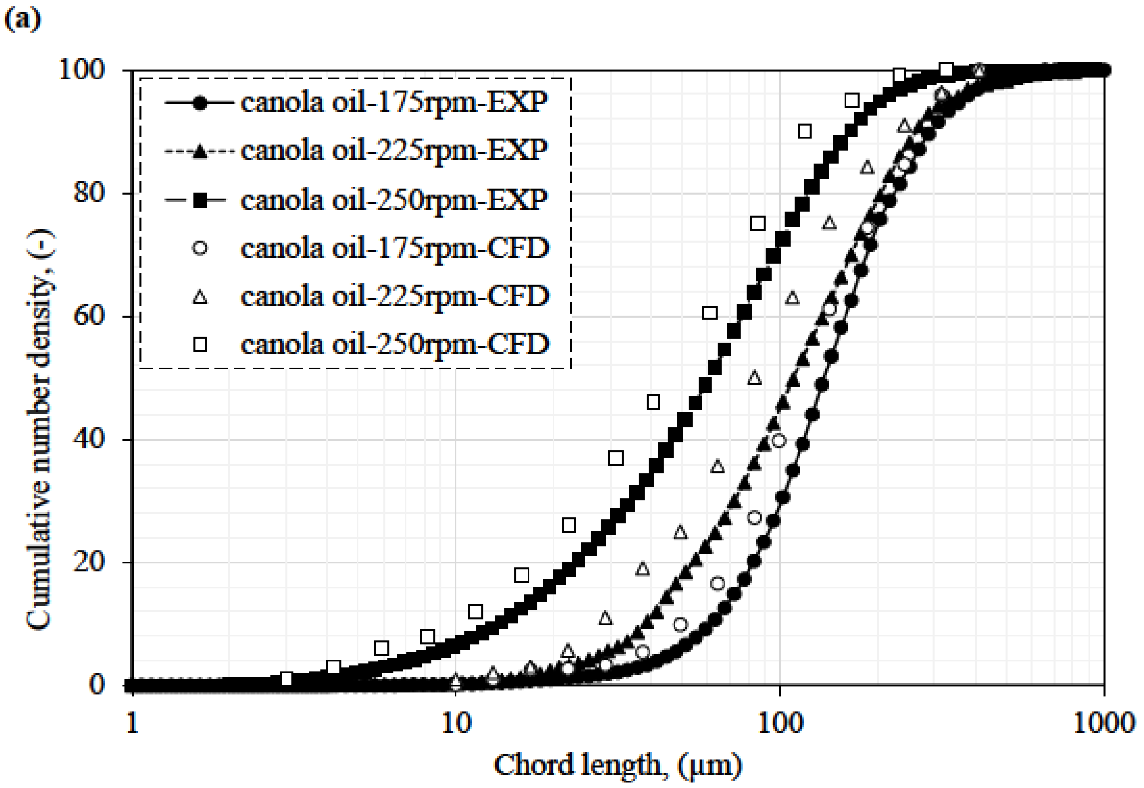

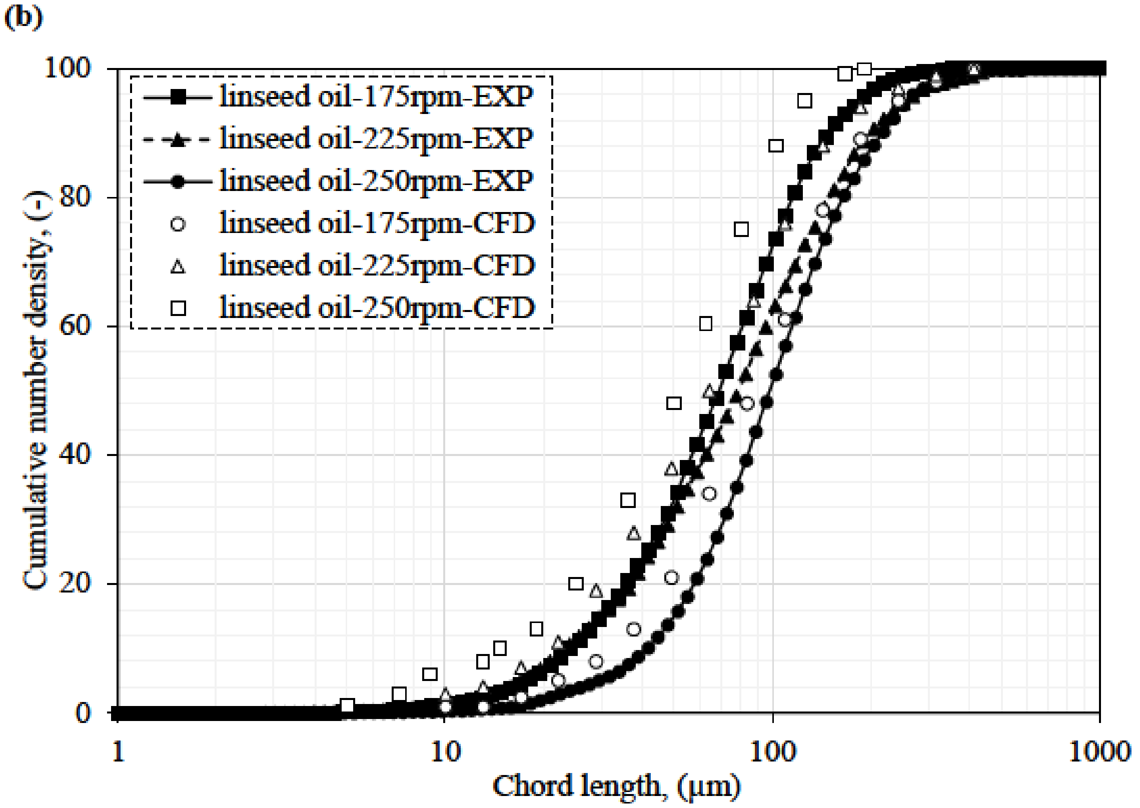

Figure 6.5. Cumulative CLD for **(a)** canola oil, and **(b)** linseed oil for 10% volume fraction at different impeller speeds.

Figure 6.6 shows ERT 2D and 3D conductivity tomograms as well as CFD vertical cross section contour plots for 10% canola oil dispersed at different impeller speeds. In this figure, the blue region in conductivity tomograms confirms higher volume fraction of dispersed phase with the lower conductivity. The conductivity tomograms show that as the impeller starts its rotation, the oil dispersed toward the bottom of the tank due to downward pumping of the impeller. Section **(a)** shows the relatively non-homogeneity, due to insufficient motion in the tank at rotational speed of 175 rpm. The blue region in plane 1 and plane 2 indicates that the motion is limited to the impeller zone, while the oil is more dispersed in plane 2 which confirms the downward pumping of the impeller. The red region in contour of volume fraction obtained by CFD also shows the inhomogeneity close to the tank surface with higher oil volume fraction. The CFD contour shows the oil dispersion in both radial and axial directions as oil was carried down to the impeller region by continuous phase. Upon increasing the impeller speed to 200 rpm (section **(b)**), the blue region at the center of plane 1 becomes smaller and thinner. CFD contour also indicates inhomogeneity at this impeller speed. Insufficient pumping power generated by impeller in the tank surface was recovered by increasing impeller speed to 225 rpm. At this impeller speed (section **(c)**), a small blue region at the center of plane 2 can be observed in the tomograms. This means that the flow is still not completely homogenous, however CFD contour indicates homogeneity in the tank. Finally, at impeller speed of 250 rpm (section **(d)**), CFD contour and conductivity tomograms show homogeneous flow

Figure 6.7 shows further analysis of mixing process for canola oil at different impeller speed with 10% volume fraction. The flow pattern was stacked by inserting 15 planes (20*17 pixels) between two adjacent key frames at X=10 and Y=10. The tomograms on X-Y planes evidently demonstrate the symmetry of oil droplet distribution within the tank. As can be seen, the dispersed phase was pumped axially at the middle of the toward the bottom of the tank which is in agreement with the flow pattern of axial impellers. This figure also shows that at impeller speed of 175rpm and 200rpm, the oil is not homogeneously distributed in the mixing vessel since the impeller speed is not adequate (**Figure 6.7(a),(b)**). As the impeller speed increased, this extent of mixing was improved.

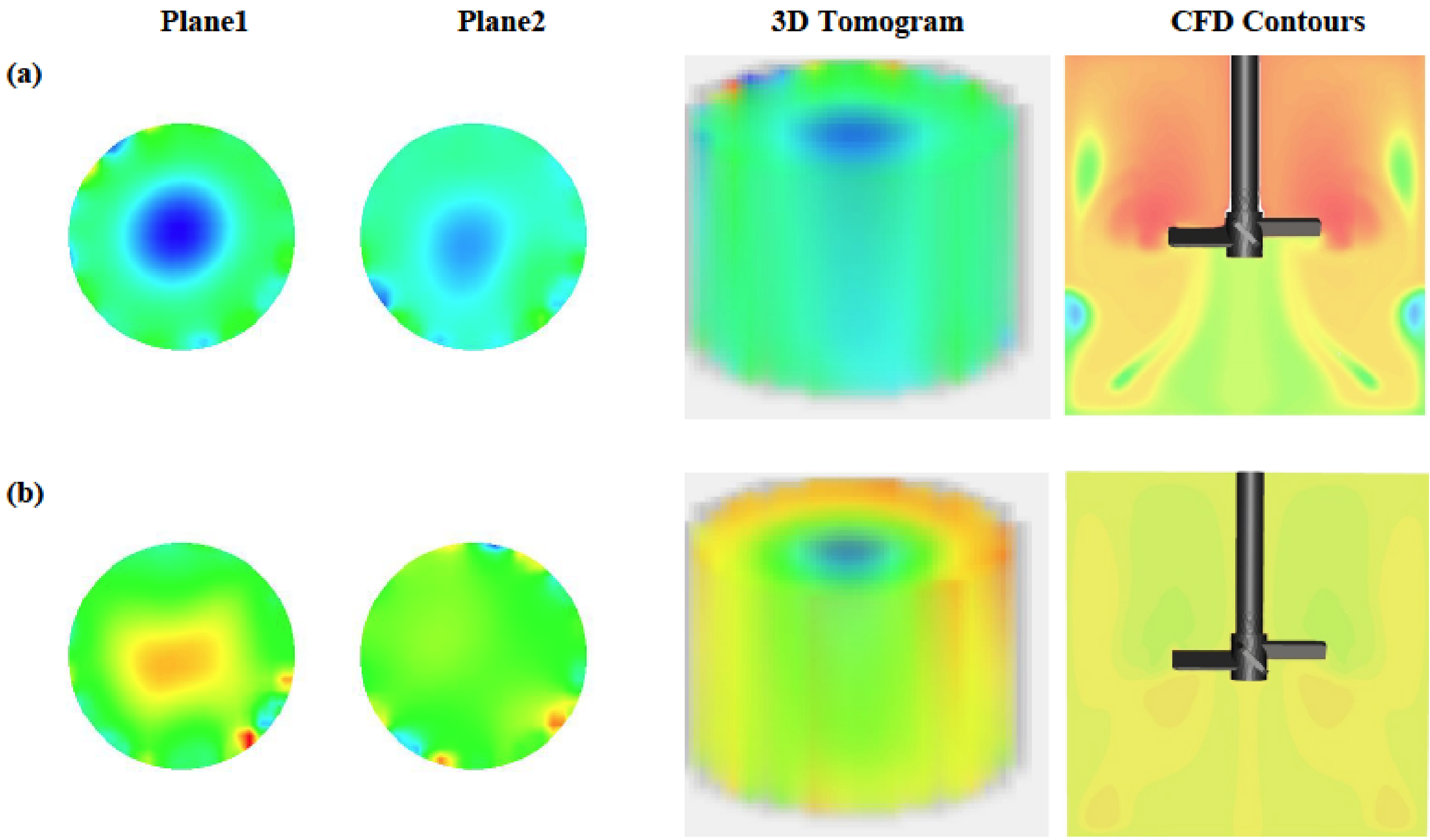
Plane1
Plane2
3D Tomogram
CFD Contours
(a)
(b)

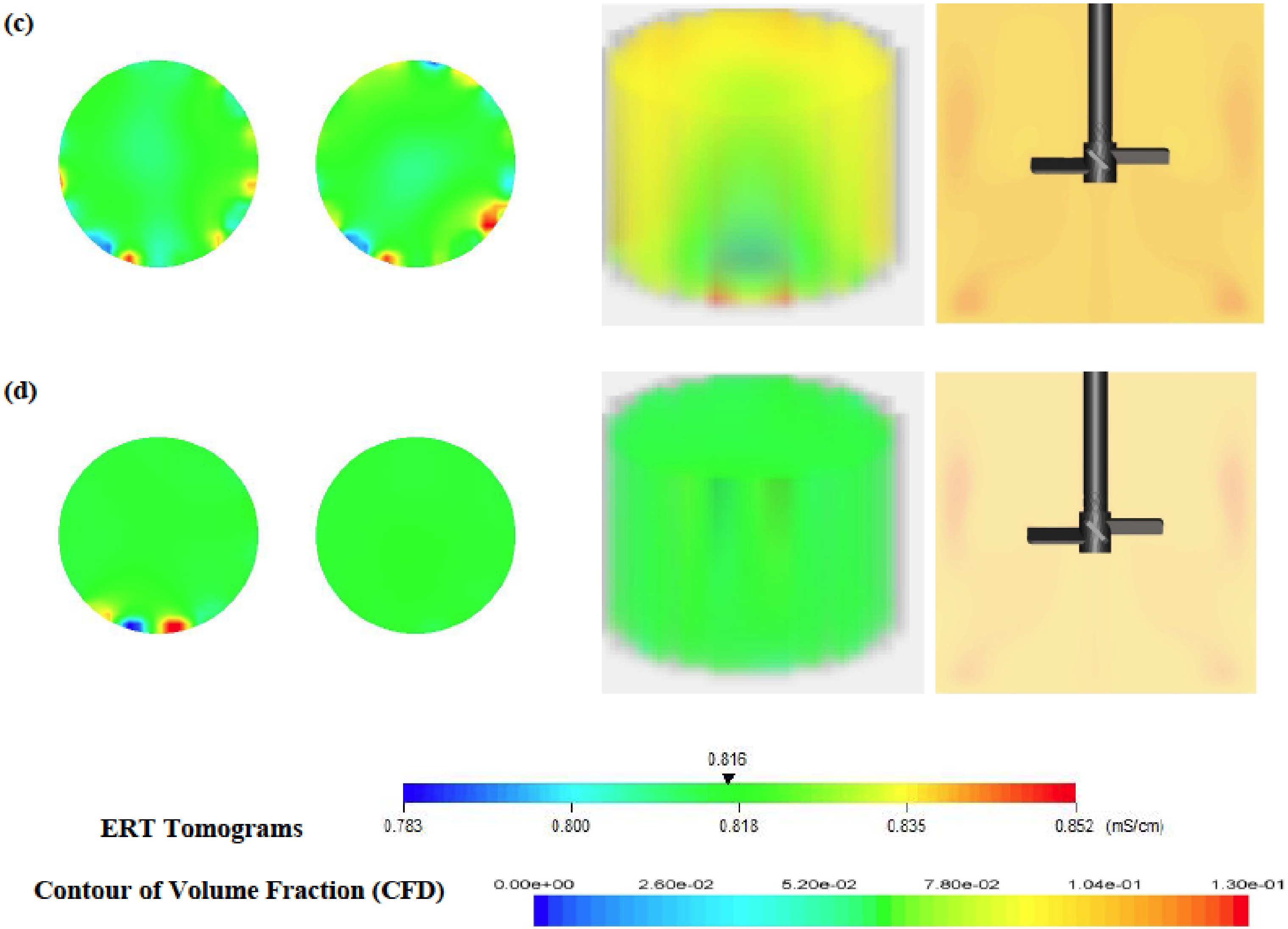

Figure 6.6. CFD contour plots of oil volume fraction and ERT conductivity tomograms for 10.0% canola oil dispersed at: **(a)** 175 rpm, **(b)** 200 rpm, **(c)** 225 rpm, and **(d)** 250 rpm.

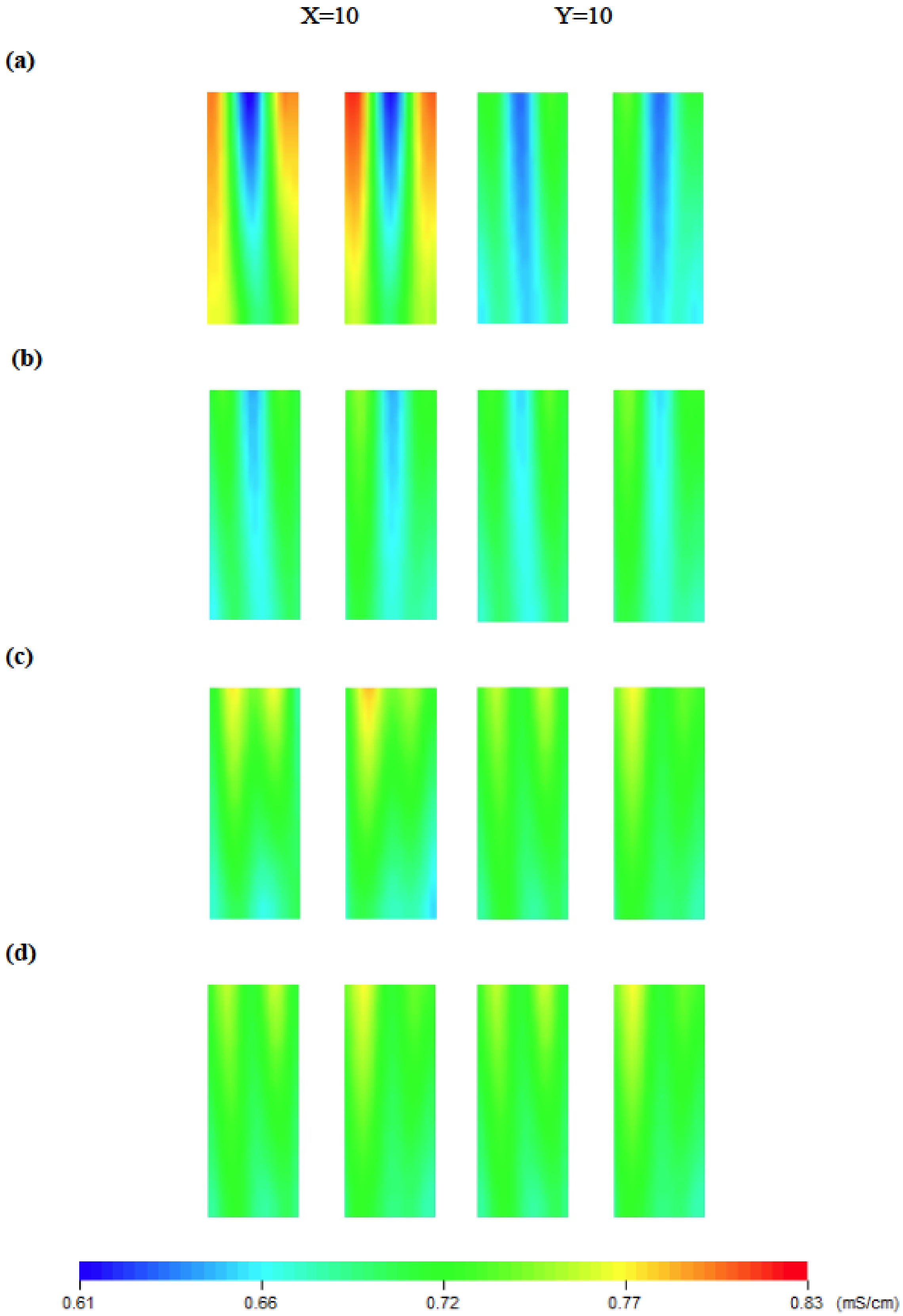

Figure 6.7. Stacked image of the mixing tank at X=10, Y=10 for canola oil at 10% volume fraction dispersed at: **(a)** 175 rpm, **(b)** 200 rpm, **(c)** 225 rpm, and **(d)** 250 rpm.

Figure 6.8 (a) compares the CLD for canola oil and linseed oil at 2.5% volume fraction and impeller speed of 250 rpm. A shift in oil-droplet size toward larger sizes and a narrower droplet size distribution were observed for canola oil. As shown in **Table 3.1,** the interfacial tension of linseed oil is higher than canola oil. Higher interfacial tension in linseed oil hinders liquid film drainage between approaching droplets by increasing the interfacial rigidity (Dowding et al., 2001). Therefore, less coalescence happens between the linseed oil-droplets. On the other hand, higher viscosity of canola oil also leads to lower breakage rate; thus, the droplet size is increased. Despite of higher viscosity of canola oil, mixing of canola oil in water resulted in larger number of formed droplets and higher number density. Generally, due to the lower energy requirements, a higher number of droplets for less viscous oil is expected.

Tcholakova et al. (2007) observed same result; larger number of droplets formed in the case of more viscous oils. They indicated that oil droplets (mother droplets) are stretched into threads prior to break-up into smaller droplets (daughter droplets), however the higher-viscosity droplets result in longer oily threads. Through a known mechanism, i.e. the capillary instability of viscous long oily threads in the turbulent flow, these oily threads break down into a number of smaller droplets. In fact, as the viscosity of dispersed oil increases, longer oily threads are generated and thus a larger number of small droplets is produced.

Liu et al. (2013) also concluded that a combination of viscous force and interfacial tension stabilizes the low-viscosity droplets, while the high-viscosity droplets are stabilized primarily by viscous forces opposing deformation and generating the oily threads. It was also presented in **Figure 6.8(b)** that, at the constant impeller speed, higher mixing index for canola oil was observed in compared to linseed oil. In fact, with an increase in viscosity, the turbulent kinetic energy induced by impeller rotation is decreased (Gréa et al., 2014). Thus; to reach a certain homogeneity in case of canola oil, more motion is required which can be achieved with an increase in the agitation speed.

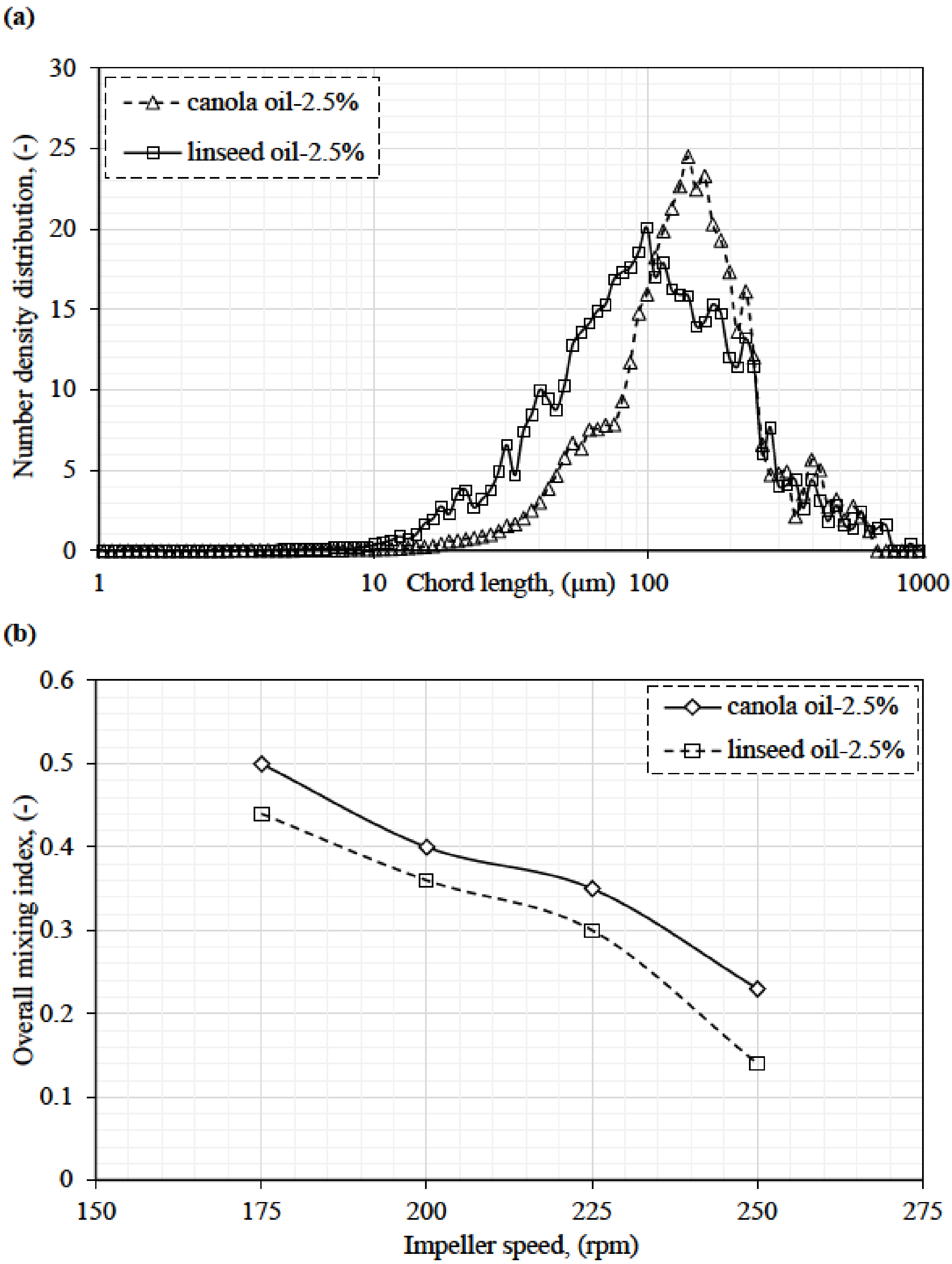

Figure 6.8. The effect of oil (with 2.5% volume fraction) type on: **(a)** CLD (at impeller speed of 250 rpm), and **(b)** Overall mixing index (*MIo*) (at different impeller speed).

The studies on the effect of particle shape on the measured particle size distribution have been limited to solid-liquid suspension (Li et al., 2005; Petrak et al., 2015; Chen et al., 2017). In liquid-liquid dispersion, droplets are generally assumed spherical in shape, however, the actual droplet's shape departs from an ideal sphere. Droplets can be deformed and elongated because of the flow shear stress (Lovick et al., 2005). Small eddies of continuous phase which not have enough energy for breakage, can only deform the droplet's shape (Paul et al., 2004). The CLD measured by FBRM is obtained from 2D projected shape of individual droplets (Li et al., 2005). Therefore, a small change in droplet's shape affects the CLD results. A projected shape of a spherical droplet is always circular, regardless of its orientation (Heath et al., 2005; Fragkopoulos et al., 2017), however the chord length measurements depend on the orientation of the non-spherical droplets.

In general, such geometries as sphere and spheroid can be observed in a liquid-liquid dispersion system (Nachtigall et al., 2016; Fragkopoulos et al., 2017). A spheroid is formed by rotating an ellipse about one of its main axes. The analysis of non-spherical particles has been limited to 2D shape analysis (Langston and Jones, 2001; Heath et al., 2005). In 2D shape analysis, a projected shape of a droplet can generally be described by an ellipse as follows:

$$(\frac{x}{a})^2 + (\frac{y}{b})^2 = 1 \tag{6.2}$$

where x and y are co-ordinates, and a and b are the semi-axis lengths with $a>b$. The droplet has spherical geometry if it has two equal semi-axis length ($a = b$). In fact, the ratio of $^a/_b$ shows how close the droplet projected shape is to a complete circular. To measure the proximity of a 2D projected shape to the outline of a circle, a circularity factor ($\psi_{p,pe}$) can be defined as (Petrak et al., 2015):

$$\psi_{p,pe} = \frac{2.\sqrt{\pi A_p}}{U_p} \leq 1 \tag{6.3}$$

where A_p and U_p are the droplet projection area and the perimeter of the droplet projected area, respectively. The circularity factor of droplet is ranging from 0 to 1. The value of 0 shows a straight line and the value of 1 shows a complete circular shape. The chord length distributions based on two particle shapes, sphere and spheroid, can be found in Petrak et al. (2015). According to their study, the correlation between the aspect ratio $\left(\frac{a}{b}\right)$ with a non-dimensional shape parameter (P), for a range of $1 \leq {}^a/_b \leq 10$ can be defined as follows:

$$\frac{a}{b} = -55.35P^5 + 431P^4 - 1313.5P^3 + 1962.3P^2 - 1433.7P + 410.34 \tag{6.4}$$

where P is defined as an area-weighted median of CLD divided by a number-weighted median of CLD. The circularity of the droplets can be then calculated for the values of $\left(\frac{a}{b}\right)$ as follows (Petrak et al., 2015):

$$\psi_{p,pe} = 1.125 - 0.119\left(\frac{a}{b}\right) + 0.0055\left(\frac{a}{b}\right)^2 \tag{6.5}$$

Figure 6.9 shows the circularity of droplet oils (i.e. canola and linseed) at 10% volume fraction and different impeller speeds. As can be seen in this figure, an increase in agitation speed resulted in a lower circularity factor confirming more deviation from a full circle. In general, droplets tend to form a spherical shape since a sphere has the minimum surface area for a given volume. In fact, a spherical shape minimizes the energy necessary to have an interface between two liquids (Fragkopoulos et al., 2017). With an increase in agitation speed, a tangential force applied to the liquid surface. Thus, the liquid surface layer moves with a certain velocity due to this external force. The velocity gradient across the flow causes liquid layers to be dragged and droplets to be deformed to an ellipse. (Fragkopoulos et al., 2017). Regardless of impeller speed, this figure also shows higher circularities for linseed oil in compared with canola oil. The origin of this behavior can be attributed to the Laplace pressure, $\Delta P = 2\sigma/r$, with ΔP as the pressure difference inside and outside of a droplet, σ as interfacial tension, and r as the radius of droplet (Fragkopoulos et al., 2017). The smaller droplet size and higher interfacial tension of linseed oil result in having larger Laplace pressure value. The higher the pressure difference, the higher the circularity of droplets. Consequently, canola oil-droplets with the larger size (refer to **Figure 6.8**) and lower interfacial tension (refer to **Table 3.1**) were deformed more by the same turbulent forces. Nachtigall et al. (2016) also reported higher deformation time, the time a spherical droplet needs to deform and finally break up, for droplets with higher viscosity than less viscous droplets.

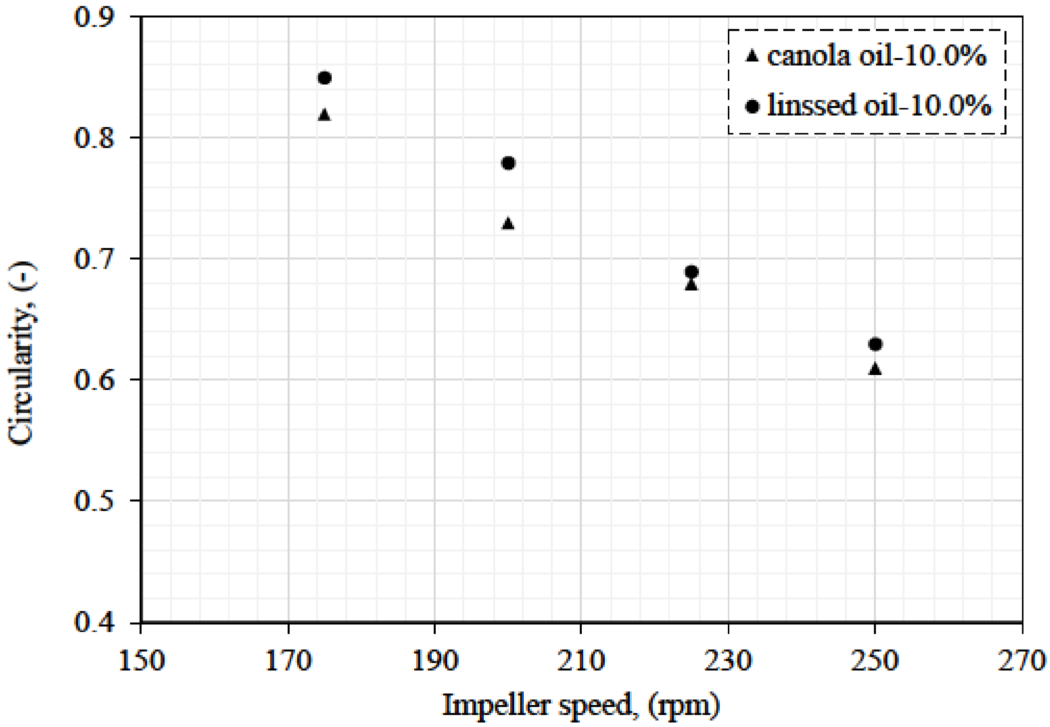

Figure 6.9. Circularity of droplets at different impeller speeds and 10.0% volume fraction.

Followed by above discussion, our analysis was limited to the two shapes that more likely are found in liquid/liquid dispersion, i.e. sphere and spheroid. The chord length distributions (CLDs) can be obtained separately for each droplet shape. **Table 6.2** shows the result of simulation in terms of droplet size (including diameter and elongation) and the probability of having each shape (sphere or spheroid) for 10% canola oil and linseed oil dispersed in water at different impeller speeds. As can be seen in this table, an increase in impeller speed leads to a decrease in the diameter and probability of sphere. The probability of oblate spheroids (spheroid with an elongation less than one) was increased at the higher impeller speeds. Lower interfacial tension of canola oil leads to larger droplet diameters and higher probability of having spheroidal droplets in the system which agrees with our previous discussion. The Sauter mean diameter, d_{32}, is an important factor in design and scale up because it is less subject to less statistical variability, it is inversely proportional to the total surface area of the dispersed phase, and it has many applications, for example, in catalysis and fuel combustion where the active surface area is of interest (Angle and Hamza, 2006).

Table 6.2. Droplet shape analysis using Python codes for both oil at 10% volume fraction.

	Canola oil	
Impeller speed	**Sphere**	**Spheroid**
175	D*= 105.38 P*=96.3%	D =69.39 E* =0.113 P =3.7%
200	D = 95.37 P =95.5%	D =53.52 E =0.072 P =4.5%
225	D = 84.41 P =95.2%	D =48.06 E =0.136 P =4.8%
250	D = 79.92 P =92.9%	D =41.23 E =0.092 P =7.1%
	Linseed oil	
175	D = 82.68 P =96.6%	D =50.85 E =0.096 P =3.4%
200	D = 82.20 P =95.7%	D =50.68 E =0.127 P =4.3%
225	D = 73.79 P =94.7%	D =42.54 E =0.011 P =5.3%
250	D = 70.53 P =93.9%	D =40.86 E =0.113 P =6.1%

*d= diameter, p= probability, e= elongation

The Sauter mean diameter, d_{32}, is an important factor in design and scale-up of stirred tanks (Angle & Hamza, 2006). **Figure 6.10** shows the Sauter mean diameter obtained at different impeller speeds for both canola and linseed oil at 10% volume fraction. As impeller speed increased, the rate of droplet breakage increased due to higher shear rate in flow and higher turbulence dissipation rate, thus an overall linear decreasing trend for d_{32} can be observed. An increase in the oil viscosity caused an increase in Sauter mean diameter. As viscous forces increase, resistance to droplet breakage increases due to an increase in cohesive forces. Hermann et al. (2011) reported that droplets with higher viscosity have less breakage rate away from impeller region where eddies have not enough turbulent energy to break the droplets; therefore, droplet breakage probability is lower at the higher dispersed phase viscosity.

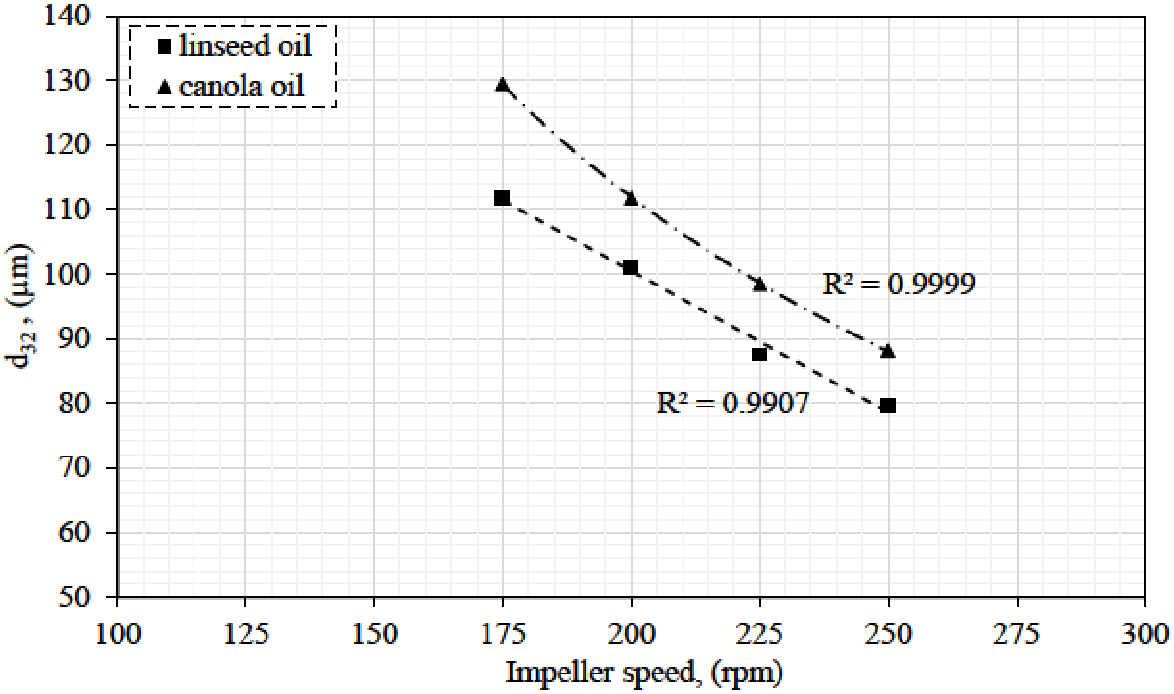

Figure 6.10. Sauter mean diameter at different impeller speed for 10.0% volume fraction.

Figure 6.11 shows the CFD contour plot of predicted d_{32} in vertical plane at impeller speed of 225 rpm and 10% volume fraction of canola oil. The contour of d_{32} shows that the size of droplets is increased at the bottom of the tank. Droplets with the equal size of Sauter mean diameter can be observed around and above the impeller. At the lower region of the mixing tank, the local energy dissipation rate is lower compared to the impeller region. As a result, the droplet breakage probability decreased. Although according to the study by Maaß et al. (2009), the large droplet is less stable, so breakage can happen with a lower energy dissipation rate far from impeller region.

Various empirical correlations found in the literature relate the mean droplet size to the different hydrodynamic parameters. Most correlations for Sauter mean diameter have been developed based on the Hinze-Kolmogorov theory of turbulent energy cascade (El-Hamouz et al., 2009; Zainal Abidin et al., 2015). According to the Kolmogorov theory (Kolmogorov, 1949), there are two mechanisms for droplet breakage, inertial subrange and viscous subrange. He introduced an eddy length scale (η) to determine the relevant mechanism of breakage as follows:

$$\eta = (\frac{\nu^3}{\varepsilon})^{1/4} \tag{6.6}$$

where ν is the kinematic viscosity and ε is the local energy dissipation rate (Wkg^{-1}). In present work, with water as a primary phase and the value of ε from CFD model equals to 0.86 m^2/s^3, η is calculated as 82 μm using Equation (6.6). In turbulent mixing with low dispersed phase viscosity and high agitation speed where droplets are larger than the eddy length scale, the inertial subrange is the prevalent regime and inertial stresses dominate over viscous stresses. Thus maximum stable droplet size is given by the balance of interfacial and inertial stresses and it is independent of continuous phase viscosity (Shinnar, 1961). Mechanistic correlations for maximum stable droplet size and Sauter mean diameter were derived in terms of dimensionless Weber number (Rueger and Calabrese, 2013). The maximum droplet size in the inertial region has a correlation with the turbulent characteristic of a system as follows:

$$\frac{d_{max}}{D} \propto \varepsilon_T^{-0.4} \propto We^{-0.6} \tag{6.7}$$

where d_{max} is maximum stable droplet size, D is impeller diameter, ε_T is mean energy dissipation rate per unit mass, and We is Weber number. The Weber number in stirred tanks is defined as:

$$We = \frac{\rho_c N^2 D^3}{\sigma} \tag{6.8}$$

where ρ_c is the density of continuous phase, N is the impeller speed, D is the impeller diameter, and σ is the surface tension.

The proportionality of maximum droplet size to Sauter mean diameter is mentioned in numerous studies which allows the above empirical correlation (refer to Eq. (6.7)) to be applied for Sauter mean diameter (El-Hamouz et al., 2009; Singh, 2009; Rueger and Calabrese, 2013; Zainal Abidin et al., 2015) as follows:

$$\frac{d_{32}}{D} \propto We^{\beta} \tag{6.9}$$

Figure 6.12 shows the contour of turbulent kinetic energy of canola oil at 10% volume fraction and 225rpm within the tank. Intense turbulent kinetic energy was observed around the impeller and upper region of the tank. High turbulent kinetic energy induced by impeller in this region can be the reason for higher droplet breakup as discussed earlier.

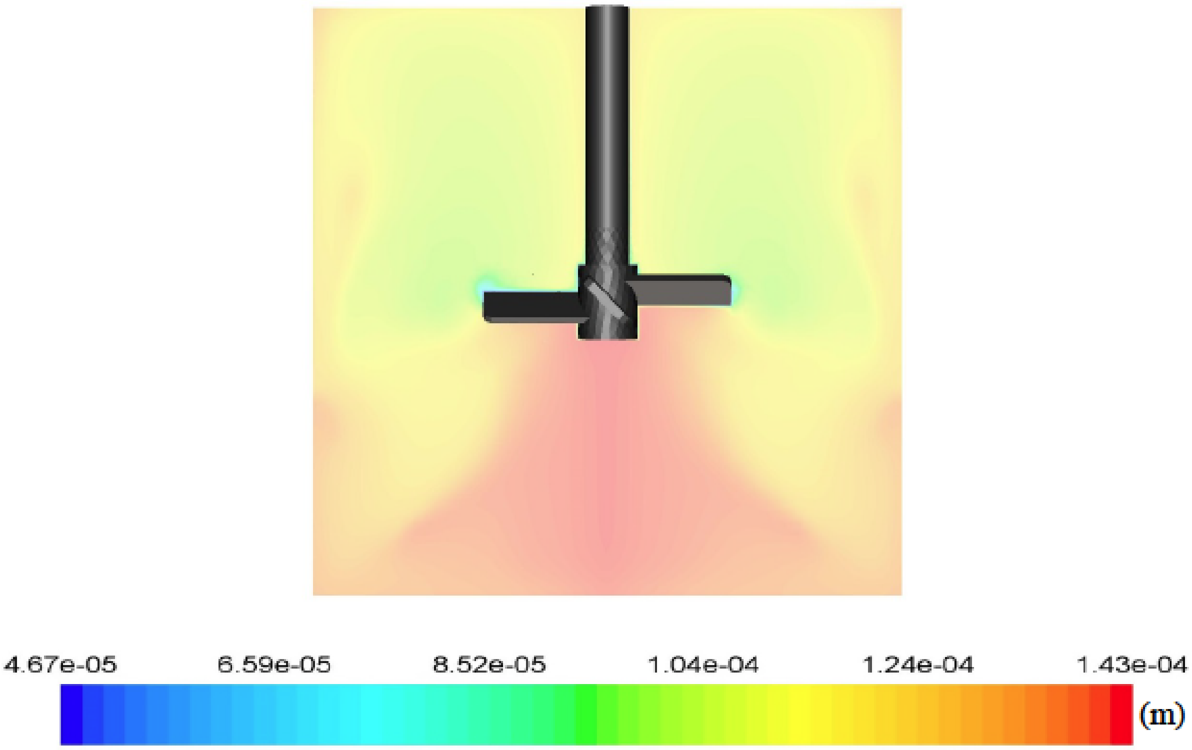

Figure 6.11. CFD Contour of Sauter mean diameter of canola oil at impeller speed of 225 rpm and10.0% volume fraction.

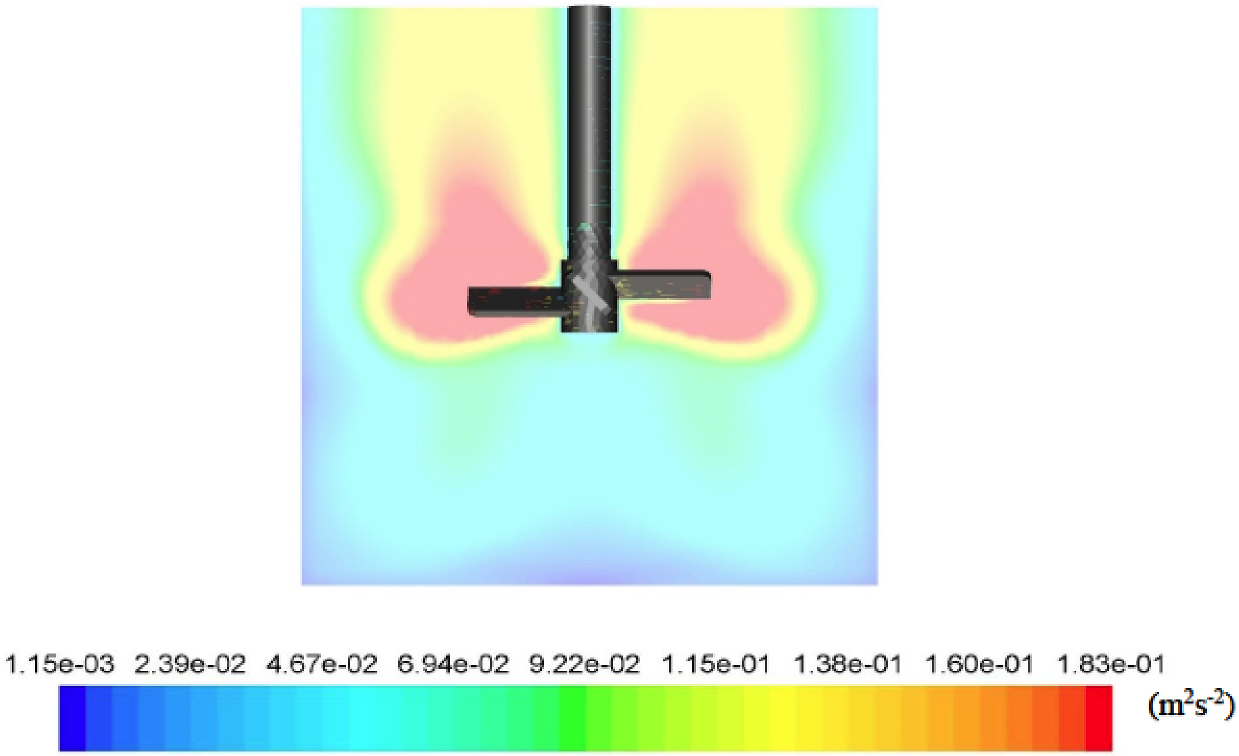

Figure 6.12. Contour of turbulent kinetic energy (m^2s^{-2}) for canola oil at impeller speed of 225 rpm and10.0% volume fraction.

Figure 6.13(a) shows Sauter mean diameter over impeller diameter as a function of Weber number for both canola and linseed oil. Our study shows the exponent of -0.48 and -0.53 which agrees with the study by Pacek et al. (1999). They reported the exponent of -0.43 for agitation of Chlorobenzene/water dispersion with Rushton impeller. El-Hamouz et al. (2009) also obtained the exponent of -0.41 for agitation of a viscous oil (242 mPas) with PBT impeller. However, from theory, the value of -0.6 was reported for the exponent in Equation (38). Some literatures mentioned experimental values in close agreement with -0.6 for dilute dispersions with a dominant droplet breakage mechanism (El-Hamouz et al., 2009; Zhou and Kresta, 1998; Zainal Abidin et al., 2015). The discrepancy between the exponent value in this study and Equation (38) is related to following reasons: (I) the value of -0.6 in Eq. (6.7) was derived for very dilute dispersions or surfactant-stabilised dispersions with the assumption of dominant breakage (Lovick et al., 2005; El-Hamouz et al., 2009; Zainal Abidin et al., 2015); however, coalescence is an important factor and cannot be ignored for volume fractions in the range of 2.5-10.0%, (II) at the beginning of agitation, as the impeller tries to bring down the oil to the impeller region, oil is drawn down in the form of long filaments. In contrast, the Buoyancy force tends to keep the large drops close to the tanks surface and large drops can remain close to the tank surface for some time which results in weaker exponent compare to Eq. (6.7) (El-Hamouz et al., 2009).

Figure 6.13(b) shows a correlation of d_{32} with impeller tip speed (ND). The correlation between Sauter mean diameter and impeller tip speed is an important scale up criteria for liquid-liquid dispersions. Both correlations in **Figure 6.13(b)** show a R^2 regression value over 99%. El-Hamouz et al. (2009) also presented a correlation between the Sauter mean diameter and (I)mean energy dissipation rate, and (II) impeller tip speed. The estimation of mean or maximum energy dissipation rate through experiments has been done in many studies such as Rueger and Calabrese (2013), and El-Hamouz et al. (2009). However, there is still a debate on how accurately one can measure the maximum energy dissipation rate. Droplet breakage predominately occurs in the impeller region where the turbulence is non-isotropic, and the turbulence depends on the impeller geometry. The rate of turbulent energy dissipation in the bulk of vessel is isotropic but insignificant compare to the impeller region. An alternative correlation criterion for Sauter mean diameter in liquid-liquid dispersion can be assessed by impeller tip speed which is independent of impeller type (El-Hamouz et al., 2009). This correlation can be used for the purpose of scale up consideration to measure the Sauter mean diameter at different impeller speeds in geometrically similar scale tanks.

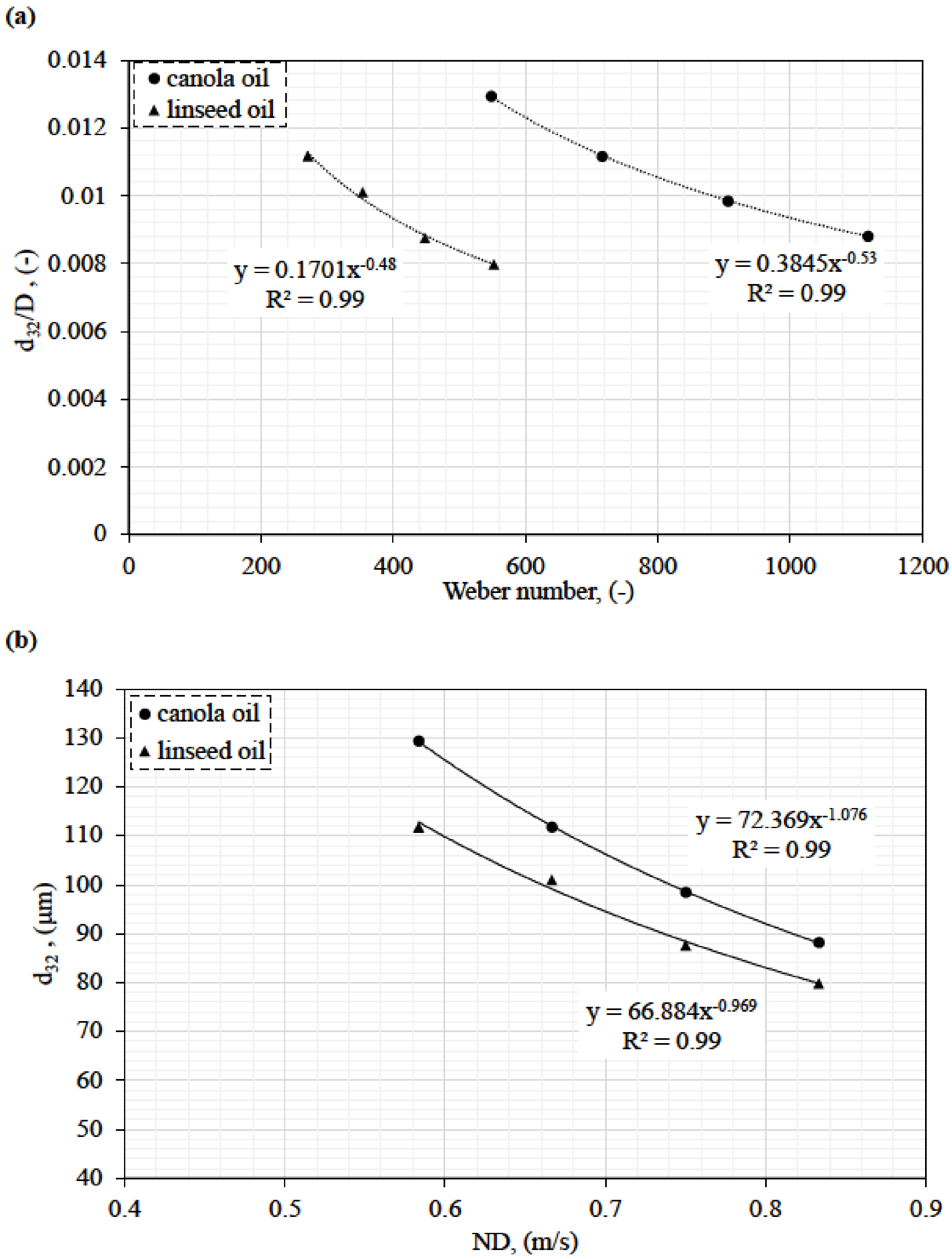

Figure 6.13. Sauter mean diameter as a function of **(a)** Weber number, and **(b)** Impeller tip speed for canola oil and linseed oil at 10.0% volume fraction.

6.4 Concluding Remarks

In this work, the effect of impeller speed, volume fraction of dispersed phase, and the viscosity of dispersed phase on hydrodynamic mixing as well as chord length distribution (CLD) of dilute oil in water dispersion were investigated by means of electrical resistance tomography (ERT) and focused beam reflectance measurement (FBRM). The experimental results were used to validate the CFD results by which a more comprehensive understanding in the mixing of liquid-liquid dispersions has been achieved.

The effect of volume fraction on droplet size was found to be negligible, however, lower volume fractions of canola oil and linseed oil showed lower mixing indices and more homogenous dispersions. With an increase in impeller speed, smaller droplets with higher fraction of in CLD were achieved. A lower mixing index was observed with an increase in impeller speed which shows an improvement in homogeneity of the dispersion. It was also found that with an increase in impeller speed, the circularity of droplets decreased, and the droplet's shape changed to oblate spheroid. The higher viscosity of canola oil also resulted in a narrower CLD and a higher mixing index compared to linseed oil regardless of impeller speed.

Results for Sauter mean diameter were correlated well with the Weber number. Our results also indicate that the existence of large oil droplets close to the surface at the beginning of mixing is a limiting factor for achieving smaller droplet size. Therefore, the correlations with *We* have weaker exponent compared to the classical relationship with an exponent of -0.6. It was also shown that the impeller tip speed is a good alternative scale up criteria for predicting droplet size due to complications in predicting accurate mean energy dissipation rate.

Overall Conclusions and Recommendation

Using a conjunction of two experimental instrument, electrical resistance tomography (ERT) and focused beam reflectance measurement (FBRM), with computational fluid dynamic (CFD) presents various important information on mixing of liquid-liquid dispersion in stirred tanks. Remarkable results are mentioned below:

An ERT system used in this study consists of 2-plane set of spherical electrodes, each containing 16 sensors. ERT was used to study the mixing performance of oil-in-water dispersion agitated by pitch-blade impeller (PBT) impeller and the following main conclusions were drawn:

- The ability of ERT system to visualize the mixing of two immiscible liquid with low volume fraction by monitoring the distribution as 2D and 3D tomograms.
- ERT can successfully show the homogenous mixing in the tank as well as providing important information in terms of mixing index and degree of homogeneity.
- Using ERT, the overall mixing indices for two different oil at four different volume fractions and four different impeller speed were calculated. A decrease in mixing indices for both oils with an increase in agitation speed, shows more homogenous flow can be obtained at higher impeller speed.
- The overall mixing index at different volume fractions of both oils, shows more homogenous flow was obtained as the volume fraction was decreased. In other words, more diluted emulsions have lower mixing index and more homogenous flow.

A FBRM laser probe (E25, Mettler-Toledo Lasentec) was used in this study to measure the chord length distribution of droplets in dispersion. Following results were obtained by FBRM:

- The effect of dispersed phase volume fraction on chord length distribution in diluted liquid-liquid dispersions was found to be negligible.
- The mean and Sauter mean diameter were found to decrease with increasing impeller speed. Also, CLDs shifted to smaller drop size.
- Viscosity and interfacial tension of dispersed phase were found to have major effect on CLDs. More viscous fluid shows smaller droplet size as well as narrower size distribution. The Effect of interfacial tension on decreasing droplet size by immobilizing the droplet surface and preventing liquid film drainage is undeniable.

- FBRM was successfully used to measure the circularity of droplets and the shape factor.

The CFD simulations were also performed and following the CFD validation by experimental data, the following main conclusions were obtained:

- The velocity vectors of impellers agreed with typical flow pattern of the Rushton and PBT impeller.
- Lehr breakage model was found to produce satisfactory results for population balance modeling.
- The result obtained for Sauter mean diameter was correlated with impeller tip speed and Weber number.

Recommendations for Future Works

- Future work can be made to investigate the effect of complex impeller type on dilute emulsions in laminar and turbulent regimes.
- Flow was modeled using discrete method in PBM, other available methods in CFD can be used to investigate the quality of obtained results.
- Using ERT for liquid-liquid mixing in stirred tanks with non-conductive continuous phase.
- Obtaining scaling laws for liquid-liquid dispersions to scale-up the multiphase processes.
- Comparing the efficiency of stirred tanks in liquid-liquid dispersions with a variety of devices such as static mixers, valve homogenizer, rotor-stator mixers.
- Investigation on droplet shape using experimental study and modeling the droplet deformation by image processing using MATLAB or other language programs.

Nomenclature

Abbreviation

FBRM	focused beam reflectance measurement
ERT	electrical resistance tomography
DSD	droplet size distribution
CLD	chord length distribution
PSD	particle size distribution
$\mathrm{MI_R}$	radial mixing index
$\mathrm{MI_z}$	axial mixing index
$\mathrm{MI_O}$	overall mixing index
CFD	computational fluid dynamic
PBT	pitch-blade impeller
DAS	data acquisition system
MRF	multiple reference frame
RMS	root-mean-square

Symbols

$C_{1\varepsilon}, C_{2\varepsilon}, C_{3\varepsilon}$	k-ε turbulent model constant, (-)
A_i	interfacial area concentration, m^2
α	phase volume fraction, (-)
a	semi-axis length, m
b	semi axis length, m
ρ	density, kgm^{-3}
$\vec{v}$	velocity vector, ms^{-1}
$\psi_{p,pe}$	droplet circularity, (-)
τ	stress tensor, Nm^{-2}
τ_i	static pressure on particle or droplet, Nm^{-2}
τ_s	particle surface stress, Nm^{-2}
τ_p	particle relaxation time in Eq. (4.5), s
g	gravitational acceleration, ms^{-2}
K	interface momentum exchange coefficient, s^{-1}
F	external force in continuity equation, N
I	unit tensor, Nm^{-2}
μ	phase viscosity in Eq. (4.3), Pa.s
μ	median of distribution in Eq. (5.1), (-)
f	drag force in Eq. (4.5), N
f	normal distribution function in Eq. (5.1), (-)
f	volume fraction in Eq. (2.1), (-)
C_D	drag coefficient, (-)
Re	Reynolds number, (-)
d	droplet diameter, m
d_{max}	maximum stable droplet size, m
e	elongation, (-)
$\acute{d}$	mother droplet diameter, m
k	turbulence kinetic energy, m^2s^{-2}
η	eddy length scale, m
ν	kinematic viscosity, m^2s^{-3}
G_k	generation rate of turbulent kinetic energy, $kgm^{-1}s^{-3}$

G_b	generation rate of turbulent kinetic energy due to buoyancy, $kgm^{-1}s^{-3}$
ε	turbulence dissipation rate, m^2s^{-3}
ε_T	mean energy dissipation rate in the tank per unit mass, m^2/s^3
$\vec{R}$	interfacial force between phases, ms^{-2}
t	time, s
M	total number of ERT measurements in a plane in Eq. (3.1), (-)
m	mass in Eq. (4.15), kg
N	impeller tip speed, rps
n	number of electrodes per plane in ERT system in Eq. (3.1), (-)
n	number density function of particles with volume V in Eq. (4.11), m^{-3}
n	number of nodes for calculation of RMS in Eq. (4.27), (-)
P	number of planes in ERT system in Eq. (2.2), (-)
P	Pressure in Eq. (4.2), Nm^{-2}
P	non-dimensional shape parameter in Eq. (2.5), (-)
P	probability of collision in Eq. (4.21), (-)
r	number of rings per plane, (-)
h	entropy of distribution, (-)
θ_{ij}	collision rate function, m^3s^{-1}
ϕ	scalar variable, (-)
λ_k	mixing weight in mixture distribution, (-)
υ	volume of a particle in Eq. (4.12), m^3
υ	Variance in Eq. (5.2), (-)
σ	surface tension in Eq. (4.26), Nm^{-1}
σ	standard deviation in Eq. (5.2), (-)
σ	conductivity in Maxwell equation in Eq. (2.1), μS/cm
σ_k	turbulent model constant in Eq. (4.9), (-)
σ_ε	turbulent model constant in Eq. (4.10), (-)
$\overline{X_{r,p}}$	average volume fraction for all rings, (-)
$X_{r,p}$	volume fraction of a ring r on plane p, (-)
B	birth rate, m^3s^{-1}
D	death rate in Eq. (4.11), m^3s^{-1}
D	impeller diameter in Eq. (5.7), m
$\Omega_B(\upsilon_i, \upsilon_k)$	breakup rate of droplet with diameter d_i into daughter droplet diameter of d_k, m^3s^{-1}
$\Omega_{ag}(\upsilon_i, \upsilon_i)$	coalescence rate of particles with volumes of v_i, and, v_j, m^3s^{-1}
β	daughter droplet size distribution, kg^{-1}
s	chord length in Eq. (2.7), m
ω	collision frequency, m^3/s
$\bar{u}$	characteristic velocity of collision, ms^{-1}
We	Weber number, (-)

Subscript

ag	aggregation
B	breakage
c	continuous phase
C	coalescence
i,j,k	local index
l	liquid
m	mixture

p	dispersed phase
pq	inter-phase
t	turbulent
t	total

References

Abramowitz, M., & Stegun, I. A. (1965). Handbook of mathematical functions: with formulas, graphs, and mathematical tables (Vol. 55). Courier Corporation.

Agahzamin, S., & Pakzad, L. (2019). A comprehensive CFD study on the effect of dense vertical internals on the hydrodynamics and population balance model in bubble columns. Chemical Engineering Science, 193, 421-435.

Agterof, W. G. M., Vaessen, G. E. J., Haagh, G. A. A. V., Klahn, J. K., & Janssen, J. J. M. (2003). Prediction of emulsion particle sizes using a computational fluid dynamics approach. Colloids and surfaces B: Bio interfaces, 31, 141-148.

Allen, T. (1990). Particle Size Measurement. 4th edition. Chapman and Hall. London.

Alopaeus, V., Koskinen, J., & Keskinen, K. I. (1999). Simulation of the population balances for liquid–liquid systems in a non-ideal stirred tank. Part 1 Description and qualitative validation of the model. Chemical Engineering Science, 54(24), 5887-5899.

Alopaeus, V., Koskinen, J., Keskinen, K. I., & Majander, J. (2002). Simulation of the population balances for liquid–liquid systems in a nonideal stirred tank. Part 2—parameter fitting and the use of the multiblock model for dense dispersions. Chemical Engineering Science, 57(10), 1815-1825.

Angle, C. W., & Hamza, H. A. (2006). Predicting the sizes of toluene-diluted heavy oil emulsions in turbulent flow Part 2: Hine–Kolmogorov based model adapted for increased oil fractions and energy dissipation in a stirred tank. Chemical engineering science, 61(22), 7325-7335.

Arellano-valle, R. B., Contreraras-reyes, J. E., & Genton, M. G. (2013). Shannon entropy and mutual information for multivariate Skew-Elliptical distributions. Scandinavian Journal of Statistics, 40(1), 42-62.

Arratia, P. E., Kukura, J., Lacombe, J., & Muzzio, F. J. (2006). Mixing of shear-thinning fluids with yield stress in stirred tanks. AIChE journal, 52(7), 2310-2322.

Azargoshasb, H., Mousavi, S. M., Jamialahmadi, O., Shojaosadati, S. A., & Mousavi, S. B. (2016). Experiments and a three-phase computational fluid dynamics (CFD) simulation coupled with population balance equations of a stirred tank bioreactor for high cell density cultivation. The Canadian Journal of Chemical Engineering, 94(1), 20-32.

Babaei, R., Bonakdarpour, B., & Ein-Mozaffari, F. (2015). The use of electrical resistance tomography for the characterization of gas holdup inside a bubble column bioreactor containing activated sludge. Chemical Engineering Journal, 268, 260-269.

Babaei, R., Bonakdarpour, B., & Ein-Mozaffari, F. (2015^{b}). Analysis of gas phase characteristics and mixing performance in an activated sludge bioreactor using electrical resistance tomography. Chemical Engineering Journal, 279, 874-884.

Bale, A. J., & Morris, A. W. (1987). In situ measurement of particle size in estuarine waters. Estuarine, Coastal and Shelf Science, 24(2), 253-263.

Becker, P. J., Puel, F., Henry, R., & Sheibat-Othman, N. (2011). Investigation of discrete population balance models and breakage kernels for dilute emulsification systems. Industrial & Engineering Chemistry Research, 50(19), 11358-11374.

Bishop, C. M. (2006). Pattern recognition and machine learning (information science and statistics), Springer-Verlag New York. Inc. Secaucus, NJ, USA.

Bolton, G. T., Hooper, C. W., Mann, R., & Stitt, E. H. (2004). Flow distribution and velocity measurement in a radial flow fixed bed reactor using electrical resistance tomography. Chemical Engineering Science, 59(10), 1989-1997.

Blazek, J. (2015). Computational fluid dynamics: principles and applications. Butterworth-Heinemann.

Boxall, J. A., Koh, C. A., Sloan, E. D., Sum, A. K., & Wu, D. T. (2009). Measurement and calibration of droplet size distributions in water-in-oil emulsions by particle video microscope and a focused beam reflectance method. Industrial & Engineering Chemistry Research, 49(3), 1412-1418.

Brown, D. E., & Pitt, K. (1972). Drop size distribution of stirred non-coalescing liquid-liquid system. Chemical Engineering Science, 27(3), 577-583.

Buffo, A., Vanni, M., & Marchisio, D. L. (2012). Multidimensional population balance model for the simulation of turbulent gas-liquid systems in stirred tank reactors. Chemical Engineering Science, 70, 31-44.

Calabrese, R. V., Chang, T. P. K., & Dang, P. T. (1986). Drop breakup in turbulent stirred-tank contactors. Part I: Effect of dispersed-phase viscosity. AIChE Journal, 32(4), 657-666.

Chen, W., Donohue, T., Katterfeld, A., & Williams, K. (2017). Comparative discrete element modelling of a vibratory sieving process with spherical and rounded polyhedron particles. Granular Matter, 19(4), 81.

Chhabra, & richardson , J. (1999). Non-Newtonian Flow in the Process Industries . butterworth heinemann

Coulaloglou, C. A., & Tavlarides, L. L. (1977). Description of interaction processes in agitated liquid-liquid dispersions. Chemical Engineering Science, 32(11), 1289-1297.

Cover, T. M., & Thomas, J. A. (2006). Elements of Information Theory Second Edition Solutions to Problems. Internet Access.

Cull, S., Lovick, J., Lye, G. J., & Angeli, P. (2002). Scale-down studies on the hydrodynamics of two-liquid phase biocatalytic reactors. Bioprocess and biosystems engineering, 25(3), 143-153.

De Hert, S. C., & Rodgers, T. L. (2017). On the effect of dispersed phase viscosity and mean residence time on the droplet size distribution for high-shear mixers. Chemical Engineering Science, 172, 423-433.

Desnoyer, C., Masbernat, O., & Gourdon, C. (2003). Experimental study of drop size distributions at high phase ratio in liquid–liquid dispersions. Chemical Engineering Science, 58(7), 1353-1363.

Dowding, P. J., Goodwin, J. W., & Vincent, B. (2001). Factors governing emulsion droplet and solid particle size measurements performed using the focused beam reflectance technique. Colloids and Surfaces A: Physicochemical and Engineering Aspects, 192, 5-13.

Drew, D., & Lahey, R. (1993). In particulate two-phase flow. Oxford: Butterworth-Heinemann.

Ebrahimi, N., Soofi, E. S., & Soyer, R. (2010). Information measures in perspective. International Statistical Review, 78(3), 383-412.

El-Hamouz, A., Cooke, M., Kowalski, A., and Sharratt, P. (2009). Dispersion of silicone oil in water surfactant solution: Effect of impeller speed, oil viscosity and addition point on drop size distribution. Chemical Engineering and Processing. Process Intensification, 48(2), 633–642.

Endoh, S., Kuga, Y., Ohya, H., Ikeda, C., & Iwata, H. (1998). Shape estimation of anisometric particles using size measurement techniques. Particle & Particle Systems Characterization: Measurement and Description of Particle Properties and Behavior in Powders and Other Disperse Systems, 15(3), 145-149.

Fan, L., Xu, N., Wang, Z., & Shi, H. (2010). PDA experiments and CFD simulation of a lab-scale oxidation ditch with surface aerators. Chemical Engineering Research and Design, 88(1), 23-33.

Fluent, I. N. C. (2006). FLUENT 6.3 user's guide. Fluent documentation.

Fragkopoulos, A. A., Pairam, E., Berger, E., Segre, P. N., & Fernández-Nieves, A. (2017). Shrinking instability of toroidal droplets. Proceedings of the National Academy of Sciences, 114(11), 2871-2875.

Frank, T., Zwart, P. J., Shi, J., Krepper, E., Lucas, D., & Rohde, U. (2005). Inhomogeneous MUSIG model-a population balance approach for poly dispersed bubbly flows.

Gelves, R., Dietrich, A., & Takors, R. (2014). Modeling of gas-liquid mass transfer in a stirred tank bioreactor agitated by a Rushton turbine or a new pitched blade impeller. Bioprocess and biosystems engineering, 37(3), 365-375.

Gerstlauer, A. (1999). Herleitung und reduktion populations dynamischer modelle am beispiel der flüssig-flüssig-extraktion. Fortschritt berichte-vdi reihe 3 verfahrenstechnik.

Ghadiri, M., & Zhang, Z. (2002). Impact attrition of particulate solids. Part 1: A theoretical model of chipping. Chemical Engineering Science, 57(17), 3659-3669.

Godfrey, J. C., & Grilc, V. (1977). Drop size and drop size distribution for liquid–liquid dispersions in agitated tanks of square cross section. In Proc 2nd European Conference on Mixing (p. C1).

Gray, R. M. (2011). Entropy and information theory. Springer Science & Business Media.

Gréa, B. J., Griffond, J., & Burlot, A. (2014). The effects of variable viscosity on the decay of homogeneous isotropic turbulence. Physics of Fluids, 26(3), 035104.

Greaves, D., Boxall, J., Mulligan, J., Montesi, A., Creek, J., Sloan, E. D., & Koh, C. A. (2008). Measuring the particle size of a known distribution using the focused beam reflectance measurement technique. Chemical Engineering Science, 63(22), 5410-5419.

Gumery, F., Ein-Mozaffari, F., & Dahman, Y. (2011). Macromixing hydrodynamic study in draft-tube airlift reactors using electrical resistance tomography. Bioprocess and biosystems engineering, 34(2), 135-144.

Hagesaether, L., Jakobsen, H. A., & Svendsen, H. F. (2002). A model for turbulent binary breakup of dispersed fluid particles. Chemical Engineering Science, 57(16), 3251-3267.

Håkansson, A., Trägårdh, C., & Bergenståhl, B. (2009). Dynamic simulation of emulsion formation in a high-pressure homogenizer. Chemical Engineering Science, 64(12), 2915-2925.

Hamood-ur-Rehman, M., Dahman, Y., & Ein-Mozaffari, F. (2012). Investigation of mixing characteristics in a packed-bed external loop airlift bioreactor using tomography images. Chemical engineering journal, 213, 50-61.

Hamood-ur-Rehman, M., Ein-Mozaffari, F., & Dahman, Y. (2013). Dynamic and local gas holdup studies in external loop recirculating airlift reactor with two rolls of fiberglass packing using electrical resistance tomography. Journal of Chemical Technology & Biotechnology, 88(5), 887-896

Harrison, S. T., Stevenson, R., & Cilliers, J. J. (2012). Assessing solids concentration homogeneity in Rushton-agitated slurry reactors using electrical resistance tomography (ERT). Chemical engineering science, 71, 392-399.

Hashemi, N., Ein-Mozaffari, F., Upreti, S. R., & Hwang, D. K. (2016). Analysis of mixing in an aerated reactor equipped with the coaxial mixer through electrical resistance tomography and response surface method. Chemical Engineering Research and Design, 109, 734-752.

Heath, A. R., Fawell, P. D., Bahri, P. A., & Swift, J. D. (2002). Estimating average particle size by focused beam reflectance measurement (FBRM). Particle & Particle Systems Characterization, 19(2), 84-95.

Heath, A. R., & Koh, P. T. (2003, December). Combined population balance and CFD modelling of particle aggregation by polymeric flocculant. In Proceedings of the 3rd International Conference on CFD in the Minerals and Process Industries (p. 10-12). CSIRO Melbourne, Australia.

Hermann, S., Maaß, S., Zedel, D., Walle, A., Schäfer, M., & Kraume, M. (2011, October). Experimental and numerical investigations of drop breakage mechanism. In Proceedings 1st International Symposium on Multiscale Multiphase Process Engineering, Kanazawa, Japan.

Hill, P. J., & Ng, K. M. (1995). New discretization procedure for the breakage equation. AIChE Journal, 41(5), 1204-1216.

Hinze, J. O. (1955). Fundamentals of the hydrodynamic mechanism of splitting in dispersion processes. AIChE Journal, 1(3), 289-295.

Hobbel, E. F., Davies, R., Rennie, F. W., Allen, T., Butler, L. E., Waters, E. R., & Sylvester, R. W. (1991). Modern methods of online size analysis for particulate process streams. Particle & Particle Systems Characterization, 8, 29-34.

Holden, P. J., Wang, M., Mann, R., Dickin, F. J., & Edwards, R. B. (1998). Imaging stirred-vessel macromixing using electrical resistance tomography. AIChE Journal, 44(4), 780-790.

Hosseini, S., Patel, D., Ein-Mozaffari, F., & Mehrvar, M. (2010). Study of solid–liquid mixing in agitated tanks through electrical resistance tomography. Chemical Engineering Science, 65(4), 1374-1384.

Hounslow, M. J., Ryall, R. L., & Marshall, V. R. (1988). A discretized population balance for nucleation, growth, and aggregation. AIChE Journal, 34(11), 1821-1832.

Hu, B., Angeli, P., Matar, O. K., Lawrence, C. J., & Hewitt, G. F. (2006). Evaluation of drop size distribution from chord length measurements. AIChE journal, 52(3), 931-939.

Jarvis, P., Jefferson, B., & Parsons, S. A. (2005). Measuring floc structural characteristics. Reviews in Environmental Science and Bio/Technology, 4(1-2), 1-18.

Kaminoyama, M., Taguchi, S., Misumi, R., & Nishi, K. (2005). Monitoring stability of reaction and dispersion states in a suspension polymerization reactor using electrical resistance tomography measurements. Chemical engineering science, 60(20), 5513-5518.

Kazemzadeh, A., Ein-Mozaffari, F., Lohi, A., & Pakzad, L. (2016). Investigation of hydrodynamic performances of coaxial mixers in agitation of yield-pseudoplastic fluids: single and double central impellers in combination with the anchor. Chemical Engineering Journal, 294, 417-430.

Kellerer, A. M. (1971). Considerations on the random traversal of convex bodies and solutions for general cylinders. Radiation Research, 47(2), 359-376.

Kendall, M. G., & Moran, P. A. P. (1963). Geometrical probability [by] MG Kendall and PAP Moran (No. 10). C. Griffin.

Kerdouss, F., Bannari, A., & Proulx, P. (2006). CFD modeling of gas dispersion and bubble size in a double turbine stirred tank. Chemical Engineering Science, 61(10), 3313-3322.

Kingman, J. F. C. (1965). Mean free paths in a convex reflecting region. Journal of Applied Probability, 2(1), 162-168.

Khakpay, A., & Abolghasemi, H. (2010). The effects of impeller speed and holdup on mean drop size in a mixer settler with spiral-type impeller. The Canadian Journal of Chemical Engineering, 88(3), 329-334.

Khalil, A., Puel, F., Chevalier, Y., Galvan, J. M., Rivoire, A., & Klein, J. P. (2010). Study of droplet size distribution during an emulsification process using in situ video probe coupled with an automatic image analysis. Chemical Engineering Journal, 165(3), 946-957.

Kim, S., Nkaya, A. N., & Dyakowski, T. (2006). Measurement of mixing of two miscible liquids in a stirred vessel with electrical resistance tomography. International communications in heat and mass transfer, 33(9), 1088-1095.

Kolmogorov, A. N. (1949). O droblenii kapel v turbulentnom potoke. Doklady Akademii Nauk Sssr, 66(5), 825-828.

Kostoglou, M., Dovas, S., & Karabelas, A. J. (1997). On the steady-state size distribution of dispersions in breakage processes. Chemical Engineering Science, 52(8), 1285-1299.

Kumar, S., Kumar, R., & Gandhi, K. S. (1991). Alternative mechanisms of drop breakage in stirred vessels. Chemical engineering science, 46(10), 2483-2489.

Laakkonen, M., Alopaeus, V., & Aittamaa, J. (2006). Validation of bubble breakage, coalescence and mass transfer models for gas–liquid dispersion in agitated vessel. Chemical engineering science, 61(1), 218-228.

Langston, P. A., & Jones, T. F. (2001). Non-spherical 2-dimensional particle size analysis from chord measurements using Bayes' theorem. Particle & Particle Systems Characterization: Measurement and Description of Particle Properties and Behavior in Powders and Other Disperse Systems, 18(1), 12-21.

Langston, P. A. (2002). Comparison of least-squares method and Bayes' theorem for deconvolution of mixture composition. Chemical engineering science, 57(13), 2371-2379.

Launder, B. E., & Spalding, D. B. (1983). The numerical computation of turbulent flows. In Numerical Prediction of Flow, Heat Transfer, Turbulence and Combustion (pp. 96-116).

Laakkonen, M., Alopaeus, V., & Aittamaa, J. (2006). Validation of bubble breakage, coalescence and mass transfer models for gas-liquid dispersion in agitated vessel. Chemical engineering science, 61(1), 218-228.

Lehr, F. (2001). Berechnen von Blasengrobenverteiungen und Stromungsfeldern in Blasensaulen. University of Hannover, Germany.

Lehr, F., Millies, M., & Mewes, D. (2002). Bubble-size distributions and flow fields in bubble columns. AIChE Journal, 48(11), 2426-2443.

Lemenand, T., Della Valle, D., Zellouf, Y., & Peerhossaini, H. (2003). Droplets formation in turbulent mixing of two immiscible fluids in a new type of static mixer. International Journal of Multiphase Flow, 29(5), 813-840.

Li, M., Wilkinson, D., & Patchigolla, K. (2005). Comparison of particle size distributions measured using different techniques. Particulate Science and Technology, 23(3), 265-284.

Liao, Y., & Lucas, D. (2009). A literature review of theoretical models for drop and bubble breakup in turbulent dispersions. Chemical Engineering Science, 64(15), 3389-3406.

Liao, Y., & Lucas, D. (2010). A literature review on mechanisms and models for the coalescence process of fluid particles. Chemical Engineering Science, 65(10), 2851-2864.

Liu, S., & Li, D. (1999). Drop coalescence in turbulent dispersions. Chemical Engineering Science, 54(23), 5667-5675.

Liu, C., Li, M., Liang, C., & Wang, W. (2013). Measurement and analysis of bimodal drop size distribution in a rotor–stator homogenizer. Chemical Engineering Science, 102, 622-631.

Liu, N., Wang, W., Tian, Y., Wu, C., & Gong, J. (2017). Experimental and numerical study for drop size distribution in oil-water dispersions with non-ionic surfactant Tween 80. Experimental Thermal and Fluid Science, 89, 153-165.

Lovick, J., Mouza, A. A., Paras, S. V., Lye, G. J., & Angeli, P. (2005). Drop size distribution in highly concentrated liquid–liquid dispersions using a light back scattering method. Journal of Chemical Technology & Biotechnology: International Research in Process, Environmental & Clean Technology, 80(5), 545-552.

Luo, H. (1993). Coalescence, breakup and liquid circulation in bubble column reactors. Dr. Ing (Doctoral dissertation, Thesis, Department of Chemical Engineering, The Norwegian Institute of Technology, Trondheim, Norway).

Luo, J. Y., & Gosman, A. D. (1994, January). Prediction of impeller-induced flow in mixing vessels using multiple frames of reference. Institute of chemical engineering symposium series.

Luo, H., & Svendsen, H. F. (1996). Theoretical model for drop and bubble breakup in turbulent dispersions. AIChE Journal, 42(5), 1225-1233.

Maaß, S., Wollny, S., Sperling, R., & Kraume, M. (2009). Numerical and experimental analysis of particle strain and breakage in turbulent dispersions. Chemical Engineering Research and Design, 87(4), 565-572.

Madupu, A., Mazumdar, A., Zhang, J., Roelant, D., & Srivastava, R. (2005). Electrical resistance tomography for real-time mapping of the solid-liquid interface in tanks containing optically opaque fluids. International Society for Optics and Photonics, 5674, 36-47.

Malik, D., & Pakzad, L. (2018). Experimental investigation on an aerated mixing vessel through electrical resistance tomography (ERT) and response surface methodology (RSM). Chemical Engineering Research and Design, 129, 327-343.

Mann, R., Williams, R. A., Dyakowski, T., Dickin, F. J., & Edwards, R. B. (1997). Development of mixing models using electrical resistance tomography. Chemical Engineering Science, 52(13), 2073-2085.

Maggioris, D., Goulas, A., Alexopoulos, A. H., Chatzi, E. G., & Kiparissides, C. (2000). Prediction of particle size distribution in suspension polymerization reactors: effect of turbulence nonhomogeneity. Chemical Engineering Science, 55(20), 4611-4627.

Marchisio, D. L., Pikturna, J. T., Fox, R. O., Vigil, R. D., & Barresi, A. A. (2003). Quadrature method of moments for population-balance equations. AIChE Journal, 49(5), 1266-1276.

Mavros, P. (2001). Flow visualization in stirred vessels: A review of experimental techniques. Chemical Engineering Research and Design, 79(2), 113-127.

Maxwell, I. C., & Electricity, A.T.O. (1873). Magnetism. Jeans, Electricity and Magnetism, 327.

Mewes, D., & Wiemann, D. (2003). Two-phase flow with mass transfer in bubble columns. Chemical Engineering & Technology: Industrial Chemistry-Plant Equipment-Process Engineering-Biotechnology, 26(8), 862-868.

Moilanen, P., Laakkonen, M., Visuri, O., Alopaeus, V., & Aittamaa, J. (2008). Modelling mass transfer in an aerated 0.2 m3 vessel agitated by Rushton, Phasejet and Combijet impellers. Chemical Engineering Journal, 142(1), 95-108.

Murthy, J. Y. (1993). A moving-deforming-mesh technique for simulation of flow in mixing tanks. In AIChE Symposium Series (pp. 37-37). American Institute of Chemical Engineers.

Myers, K. J. (1994). Simulation and experimental verification of liquid-solid agitation performance.

Nachtigall, S., Zedel, D., & Kraume, M. (2016). Analysis of drop deformation dynamics in turbulent flow. Chinese Journal of Chemical Engineering, 24(2), 264-277.

Nagata, S. (1975). Mixing: principles and applications. Halsted Press.

Nambiar, D. K. R., Kumar, R., Das, T. R., & Gandhi, K. S. (1992). A new model for the breakage frequency of drops in turbulent stirred dispersions. Chemical Engineering Science, 47(12), 2989-3002.

Narayanan, K. R., & Srinivasa, A. R. (2012). Shannon-entropy-based nonequilibrium “entropic” temperature of a general distribution. Physical Review E, 85(3), 031151.

Narsimhan, G., Nejfelt, G., & Ramkrishna, D. (1984). Breakage functions for droplets in agitated liquid-liquid dispersions. AIChE Journal, 30(3), 457-467.

Nastac, L., Zhang, L., Thomas, B.G., Sabau, A., El-Kaddah, N., Powel, A.C., & Combeau, H. (2012). CFD Modeling and Simulation in Material Processing. Wiley. Florida.

Ohtake T., Hano T., Takagi K., & Nakashio, F. (1987). Effects of viscosity on drop diameter of w/o emulsion dispersed in a stirred tank. Journal of chemical engineering of Japan, 20(5), 443-447.

Ohtake, T., Hano, T., Takagi, K., & Nakashio, F. (1988). Analysis of water entrapment into dispersed w/o emulsion drops. Journal of chemical engineering of Japan, 21(3), 272-276.

Ok, T., Ookawara, S., Yoshikawa, S., & Ogawa, K. (2003). Drop size distribution in liquid-liquid mixing. Journal of chemical engineering of Japan, 36(8), 940-945.

Pacek, A. W., Man, C. C., & Nienow, A. W. (1998). On the Sauter mean diameter and size distributions in turbulent liquid/liquid dispersions in a stirred vessel. Chemical Engineering Science, 53(11), 2005-2011.

Pakzad, L. (2007). Using Electrical Resistance Tomography (ERT) and Computational Fluid Dynamics (CFD) to Study the Mixing of Pseudoplastic Fluids with a Scaba 6SRGT Impeller. MA Sc (Doctoral dissertation, Thesis, Ryerson University, Toronto).

Pakzad, L., Ein-Mozaffari, F., & Chan, P. (2008). Measuring Mixing Time in the Agitation of Non-Newtonian Fluids through Electrical Resistance Tomography. Chemical Engineering & Technology: Industrial Chemistry-Plant Equipment-Process Engineering Biotechnology, 31(12), 1838-1845.

Pakzad, L., Ein-Mozaffari, F., & Chan, P. (2008). Using electrical resistance tomography and computational fluid dynamics modeling to study the formation of cavern in the mixing of pseudoplastic fluids possessing yield stress. Chemical Engineering Science, 63(9), 2508-2522.

Patankar, S. (1980). Numerical heat transfer and fluid flow. CRC press.

Patel, H., Ein-Mozaffari, F., & Dhib, R. (2010). CFD analysis of mixing in thermal polymerization of styrene. Computers & chemical engineering, 34(4), 421-429.

Patel, D., Ein-Mozaffari, F., & Mehrvar, M. (2014). Tomography images to analyze the deformation of the cavern in the continuous-flow mixing of non-Newtonian fluids. AIChE Journal, 60(1), 315-331.

Patel, D., Ein-Mozaffari, F., & Mehrvar, M. (2014^{b}). Using tomography to visualize the continuous-flow mixing of biopolymer solutions inside a stirred tank reactor. Chemical Engineering Journal, 239, 257-273.

Patel, D., Ein-Mozaffari, F., & Mehrvar, M. (2015). Effect of rheological parameters on non-ideal flows in the continuous-flow mixing of biopolymer solutions. Chemical Engineering Research and Design, 100, 126-134.

Paul, E. L., Atiemo-Obeng, V. A., & Kresta, S. M. (Eds.). (2004). Handbook of industrial mixing: science and practice. John Wiley & Sons.

Petrak. D, Dietrich. S, Eckardt. G, Köhler. M. (2011). In-line particle sizing for real-time process control by fibre-optical spatial filtering technique (SFT). Advanced Powder Technology. 22, 203–208.

Poilov, V. Z., Kosvintsev, O. K., Gramlich, K., Kodura, J., & Karvot, R. (1997). Formation of magnesium chloride particles in bulk polythermal crystallization. Russian journal of applied chemistry, 70(7), 1036-1040.

Politis, D. N. (1994). Maximum entropy modelling of mixture distributions. Kybernetes, 23(1), 49-54.

Qi, L., Meng, X., Zhang, R., Liu, H., Xu, C., Liu, Z., & Klusener, P. A. (2015). Droplet size distribution and droplet size correlation of chloroaluminate ionic liquid–heptane dispersion in a stirred vessel. Chemical Engineering Journal, 268, 116-124.

Raikar, N. B., Bhatia, S. R., Malone, M. F., & Henson, M. A. (2009). Experimental studies and population balance equation models for breakage prediction of emulsion drop size distributions. Chemical Engineering Science, 64(10), 2433-2447.

Ramkrishna, D. (2000). Population balances: Theory and applications to particulate systems in engineering. Elsevier.

Ranade, V. V., & Dommeti, S. M. (1996). Computational snapshot of flow generated by axial impeller in baffled stirred vessels. Chemical engineering research & design, 74(4), 476-484.

Ranade, V. V. (2001). Computational flow modeling for chemical reactor engineering (Vol. 5). Elsevier.

Randolph, A. D., & Larson, M. A. (1988). Theory of particulate process: analysis and techniques of continuous crystallization. Academic Press.

Rathore, A. S., Sharma, C., & Persad, A. A. (2012). Use of computational fluid dynamics as a tool for establishing process design space for mixing in a bioreactor. Biotechnology progress, 28(2), 382-391.

Revankar, S. T. (2001). Coalescence and breakup of fluid particles in multi-phase flow. In 4th International Conference on Multiphase Flow, New Orleans, USA (p. 352).

Ribeiro, M. M. M., Guimaraes, M. M. L., Madureira, C. M. N., & Pinto, J. C. (2004). Non-invasive system and procedures for the characterization of liquid–liquid dispersions. Chemical Engineering Journal, 97(2-3), 173-182.

Roudsari, S. F., Turcotte, G., Dhib, R., & Ein-Mozaffari, F. (2012). CFD modeling of the mixing of water in oil emulsions. Computers & Chemical Engineering, 45, 124-136.

Rueger, P. E., & Calabrese, R. V. (2013). Dispersion of water into oil in a rotor–stator mixer. Part 2: Effect of phase fraction. Chemical Engineering Research and Design, 91(11), 2134-2141.

Ruiz, M. C., Lermanda, P., & Padilla, R. (2002). Drop size distribution in a batch mixer under breakage conditions. Hydrometallurgy, 63(1), 65-74.

Russ, J. C. (2016). The image processing handbook. CRC press.

Schiller, L. (1933). Über die grundlegenden Berechnungen bei der Schwerkraftaufbereitung. Z. Vereines Deutscher Inge., 77, 318-321.

Schütz, S., Gorbach, G., & Piesche, M. (2009). Modeling fluid behavior and droplet interactions during liquid–liquid separation in hydrocyclones. Chemical Engineering Science, 64(18), 3935-3952.

Shannon, Claude E., Warren Weaver, and Arthur W. Burks. "The mathematical theory of communication." (1951).

Sharma, S. K., Stanley, D. A., & Harris, J. (1994). Determining the effect of physico-chemical parameters on floc size using a population balance model. Minerals and Metallurgical Processing, 11(3), 168-173.

Sharifi, M., & Young, B. (2013). Electrical resistance tomography (ERT) applications to chemical engineering. Chemical Engineering Research and Design, 91(9), 1625-1645.

Siddiqui, H. (1993). Mixing technology for buoyant solids in a nonstandard vessel. AIChE journal, 39(3), 505-509.

Sidiropoulos, P. (2014). N-sphere chord length distribution. arXiv preprint arXiv:1411.5639.

Simon, M., Schmidt, S. A., & Bart, H. J. (2003). The droplet population balance model–estimation of breakage and coalescence. Chemical Engineering & Technology: Industrial Chemistry-Plant Equipment-Process Engineering-Biotechnology, 26(7), 745-750.

Singh, K. K., Mahajani, S. M., Shenoy, K. T., & Ghosh, S. K. (2008). Representative drop sizes and drop size distributions in A/O dispersions in continuous flow stirred tank. Hydrometallurgy, 90(2-4), 121-136.

Singh, V. P. (2013). Entropy theory and its application in environmental and water engineering. John Wiley & Sons.

Sjoblom, J. (Ed.). (2001). Encyclopedic handbook of emulsion technology. CRC Press.

Skelland, A. H. P. (1967). Non-Newtonian flow and heat transfer. Wiley.

Solsvik, J., & Jakobsen, H. A. (2015). Single drop breakup experiments in stirred liquid–liquid tank. Chemical Engineering Science, 131, 219-234.

Sprow, F. B. (1967). Distribution of drop sizes produced in turbulent liquid—liquid dispersion. Chemical Engineering Science, 22(3), 435-442.

Srilatha, C., Morab, V. V., Mundada, T. P., & Patwardhan, A. W. (2010). Relation between hydrodynamics and drop size distributions in pump–mix mixer. Chemical Engineering Science, 65(11), 3409-3426.

Stamatoudis, M., & Tavlarides, L. L. (1987). The effect of continuous-phase viscosity on the unsteady state behavior of liquid-liquid agitated dispersions. The Chemical Engineering Journal, 35(2), 137-143.

Stanley, S. J. (2006). Tomographic imaging during reactive precipitation in a stirred vessel: Mixing with chemical reaction. Chemical Engineering Science, 61(24), 7850-7863.

Tadayyon, A., & Rohani, S. (1998). Determination of particle size distribution by Par-Tec® 100: modeling and experimental results. Particle & Particle Systems Characterization: Measurement and Description of Particle Properties and Behavior in Powders and Other Disperse Systems, 15(3), 127-135.

Tahvildarian, P., Ng, H., D'Amato, M., Drappel, S., Ein-Mozaffari, F., & Upreti, S. R. (2011). Using electrical resistance tomography images to characterize the mixing of micron-sized polymeric particles in a slurry reactor. Chemical engineering journal, 172(1), 517-525.

Tatterson, G. B. (1991). Fluid mixing and gas dispersion in agitated tanks. McGraw-Hill Companies.

Tcholakova, S., Vankova, N., Denkov, N. D., & Danner, T. (2007). Emulsification in turbulent flow: 3. Daughter drop-size distribution. Journal of Colloid and Interface Science, 310(2), 570-589.

Tsouris, C., & Tavlarides, L. L. (1994). Breakage and coalescence models for drops in turbulent dispersions. AIChE Journal, 40(3), 395-406.

Valentas, K. J., & Amundson, N. R. (1966). Breakage and coalescence in dispersed phase systems. Industrial & Engineering Chemistry Fundamentals, 5(4), 533-542.

Vankova, N., Tcholakova, S., Denkov, N. D., Ivanov, I. B., Vulchev, V. D., & Danner, T. (2007). Emulsification in turbulent flow: 1. Mean and maximum drop diameters in inertial and viscous regimes. Journal of Colloid and Interface Science, 312(2), 363-380.

Verhoff, F. H., Ross, S. L., & Curl, R. L. (1977). Breakage and coalescence processes in an agitated dispersion. Experimental system and data reduction. Industrial & Engineering Chemistry Fundamentals, 16(3), 371-377.

Versteeg, H. K., & Malalasekera, W. (2007). An introduction to computational fluid dynamics: the finite volume method. Pearson Education.

Vladisavljević, G. T., Kobayashi, I., & Nakajima, M. (2011). Effect of dispersed phase viscosity on maximum droplet generation frequency in microchannel emulsification using asymmetric straight-through channels. Microfluidics and Nanofluidics, 10(6), 1199-1209.

Vlaev, D., Wang, M., Dyakowski, T., Mann, R., & Grieve, B. D. (2000). Detecting filter-cake pathologies in solid–liquid filtration: semi-tech scale demonstrations using electrical resistance tomography (ERT). Chemical Engineering Journal, 77(1-2), 87-91.

Vonka, M., & Soos, M. (2015). Characterization of liquid-liquid dispersions with variable viscosity by coupled computational fluid dynamics and population balances. AIChE Journal, 61(8), 2403-2414.

Wang, M., Dorward, A., Vlaev, D., & Mann, R. (2000). Measurements of gas-liquid mixing in a stirred vessel using electrical resistance tomography (ERT). Chemical Engineering Journal, 77(1-2), 93-98.

Wang, W., Liu, J., Wang, P., Duan, J., & Gong, J. (2013). Evolution of dispersed drops during the mixing of mineral oil and water phases in a stirred tank. Chemical Engineering Science, 91, 173-179.

Williams, R. A, & Beck, M. S. (1996). Process tomography: a European innovation and its applications. Measurement Science and Technology, 7(3), 215.

White, R., & Doblin, C. (2003, December). An investigation of sparged mixing tanks using electrical impedance tomography and computational fluid dynamics. In Third International Conference on CFD in the Mineral and Process Industries, Melbourne, Australia.

Wu, Q., Kim, S., Ishii, M., & Beus, S. G. (1998). One-group interfacial area transport in vertical bubbly flow. International Journal of Heat and Mass Transfer, 41(8-9), 1103-1112.

Wutz, J., Lapin, A., Siebler, F., Schäfer, J. E., Wucherpfennig, T., Berger, M., & Takors, R. (2016). Predictability of kLa in stirred tank reactors under multiple operating conditions using an Euler–Lagrange approach. Engineering in Life Sciences, 16(7), 633-642.

Xu, R., & Di Guida, O. A. (2003). Comparison of sizing small particles using different technologies. Powder Technology, 132(2-3), 145-153.

Zainal Abidin, M. I. I., Abdul Raman, A. A., & Mohamad Nor, M. I. (2015). Mean drop size correlations and population balance models for liquid-liquid dispersion. AIChE Journal, 61(4), 1129-1145.

Zhang, L., & Chen, B. (2012). Applications of Shannon's entropy theory to naphtha pyrolysis simulation. Chemical Engineering & Technology, 35(2), 281-286.

Zhao, Z. F., Mehrvar, M., & Ein-Mozaffari, F. (2008). Mixing time in an agitated multi-lamp cylindrical photoreactor using electrical resistance tomography. Journal of Chemical Technology & Biotechnology: International Research in Process, Environmental & Clean Technology, 83(12), 1676-1688.

Zhao, Y., Li, X., Cheng, J., Yang, C., & Mao, Z. S. (2011). Experimental study on liquid–liquid macromixing in a stirred tank. Industrial & Engineering Chemistry Research, 50(10), 5952-5958.

Zhou, G., & Kresta, S. M. (1998). Correlation of mean drop size and minimum drop size with the turbulence energy dissipation and the flow in an agitated tank. Chemical Engineering Science, 53(11), 2063-2079.

Appendix A

Python Codes for Simulation of Droplet Shape using Mixture Distribution and Information Theory

```
#!/usr/bin/env python 2.7
import numpy as np
import pandas as pd
import numexpr as ne
from scipy import optimize
from scipy.special import beta
from scipy.special import gamma
from scipy.special import polygamma
import matplotlib.pyplot as plt
plt.close("all")
from pyomo.environ import *
from math import pi
**********************************************************************************
#instance = './file location/file name.txt'
#df = pd.read_csv(instance, sep='\t')
##df['Mean, No Wt (Macro)'].plot()
#first_sample = **(time sample)
#last_sample = **(time sample)
**********************************************************************************
df = df.iloc[first_sample:last_sample,:]
X_mean = df['Mean, No Wt (Macro)'].values
*********************************************************************************
M = ConcreteModel()
# Sphere
M.d1 = Var(bounds=(1, None), domain=NonNegativeReals, initialize=np.mean(X_mean))
M.p1 = Var(bounds= (0,1), domain=NonNegativeReals, initialize=0.5)
# Spheroid
M.d2 = Var(bounds=(1, None), domain=NonNegativeReals, initialize=np.mean(X_mean))
```

```
M.e = Var(bounds= (0,1), domain=NonNegativeReals, initialize=0.5)
M.p2 = Var(bounds= (0,1), domain=NonNegativeReals, initialize=0.5)
S = np.linspace(1,np.max(X_mean)*5,1000)
def ci(x):
    if value(x) > 1:
        return acosh(x)
    else:
        return acos(x)
def H(x):
    return np.heaviside(value(x),1)
def f1(M,s):
    f = (2/(M.d1**2))*s
    return f
def f2(M,s):
    c1 = (1/2) + (M.e**2)*(1/2)*(1/sqrt(1-M.e**2))*ci(1/M.e)
    c2 = (1/4)*(1/M.e**2) + (3/4)*c1
    f = (2/c1)*(s/(M.d2**2)) * ( c2 + sqrt(1-M.e**2)*(1/4)*(1/(M.e**(-2) - 1)) *\
            (sqrt(abs(M.d2**2 / s**2 - 1)) * (M.d2**3 / s**3 + (3/2)*(M.d2 / s) +
(3/2)*ci(M.d2/s) ) ) )
    return f
def fmix(M,s):
    f = (M.p1)*f1(M,s) + (M.p2)*f2(M,s)
    return f
M.o = Objective(expr= -sum( fmix(M,s)*log(fmix(M,s)) for s in S), sense = maximize)

M.c1 = Constraint (expr= M.p1 + M.p2 == 1)

M.c2 = Constraint (expr= (M.p1)*(2/3)*M.d1 +\
                (M.p2)*8*(M.d2)*(M.e)*sqrt(1-M.e**2) *\
                (1/(   6*sqrt(1-M.e**2)+3*(M.e**2)*log((1+sqrt(1-M.e**2))/(1-sqrt(1-M.e**2)))
))  <= np.max(X_mean))
```

```
 M.c3 = Constraint (expr= (M.p1)*(2/3)*M.d1 +\
                (M.p2)*8*(M.d2)*(M.e)*sqrt(1-M.e**2) *\
                (1/(6*sqrt(1-M.e**2)+3*(M.e**2)*log((1+sqrt(1-M.e**2))/(1-sqrt(1-M.e**2))) ))
>= np.min(X_mean)
 solver = SolverFactory('ipopt')
 solver.solve(M)

 S = S[np.where((S<=np.mean(X_mean)))]
 pdf = np.zeros(np.size(S))
 for i in np.arange(np.size(S)):
    pdf[i] = value(fmix(M, S[i]))

 normFactor = np.sum(pdf)
 pdf = pdf / normFactor

 xStar = np.argmin(pdf)


 ******************************************************************************

 plt.plot(S[0:xStar+1],pdf[0:xStar+1], linewidth=1.5, linestyle="-.", c="red", label='spheroid
regime')
 plt.plot(S[xStar:],pdf[xStar:], linewidth=1.5, linestyle="-", c="black", label='sphere regime')
 plt.title(instance)
 plt.xlabel('s (micron)')
 plt.xticks(np.arange(0,S[-1] , step=5))
 plt.legend(loc=1, bbox_transform=plt.gcf().transFigure)
 plt.plot()

 print ('------------------------')
 print('Sphere')
 print ('d = ' + str(value(M.d1)))
 print ('prob = ' + str(value(M.p1)))
```

```
print ('---------------------------')
print('Sphereoid')
print ('d = ' + str(value(M.d2)))
print ('e = ' + str(value(M.e)))
print ('prob = ' + str(value(M.p2)))
```